Theoretical and Experimental Investigation of Multiple Quantum Wells for Photovoltaic Applications

A THESIS

Submitted in partial fulfillment of the
requirements for the award of the degree
of
DOCTOR OF PHILOSOPHY

by

GAURAV SIDDHARTH

DEPARTMENT OF ELECTRICAL ENGINEERING
INDIAN INSTITUTE OF TECHNOLOGY INDORE

MAY 2021

INDIAN INSTITUTE OF TECHNOLOGY INDORE

CANDIDATE'S DECLARATION

I hereby certify that the work which is being presented in the thesis entitled **"Theoretical and experimental investigation of multiple quantum wells for photovoltaic applications"** in the partial fulfilment of the requirements for the award of the degree of **Doctor of Philosophy** and submitted in the **Department of Electrical Engineering, Indian Institute of Technology Indore**, is an authentic record of my own work carried out during the time period from **July, 2016** to **May, 2021** under the supervision of **Dr. Shaibal Mukherjee**, Associate Professor, Electrical Engineering, IIT Indore.

The matter presented in this thesis has not been submitted by me for the award of any other degree of this or any other institute.

Gaurav 04/05/2021

Signature of the student with date

GAURAV SIDDHARTH

This is to certify that the above statement made by the candidate is correct to the best of my knowledge.

S. Mukherjee
4 May 2021

Signature of Thesis Supervisor with date

Dr. SHAIBAL MUKHERJEE

GAURAV SIDDHARTH has successfully given his Ph.D. Oral Examination held on **03 September 2021**

S. Mukherjee
3 September 2021

Signature of Thesis Supervisor with date

Dr. SHAIBAL MUKHERJEE

ACKNOWLEDGEMENTS

First of all, I would like to express my sincere appreciation to my thesis supervisor **Dr. Shaibal Mukherjee**, Associate Professor, Department of Electrical Engineering IIT Indore, for his generous guidance, support, monitoring, constant encouragement, timely suggestions and the detailed discussion without which this work would not have been possible. He consistently allowed this thesis to be my own work, but he steered me in the right direction whenever he thought I needed it.

I am extremely grateful to my doctoral committee members **Dr. Mukesh Kumar** and **Dr. Swadesh Kumar Sahoo** for their encouragement, valuable advice, questions, insightful comments and co-operation throughout the work.

My sincere thanks go to **Prof. Neelesh Kumar Jain**, Director, IIT Indore for providing the essential experimental facilities. I want to acknowledge the support provided by sophisticated instrumentation center (SIC) at IIT Indore, for performing XRD, SEM, and EDX measurements.

My sincere appreciation to **Dr. Myo Than Htay**, and **Dr. Mukul Gupta** for their valuable experimental support in the HRTEM, and SIMS. This thesis would not have been possible without your helpful support and guidance.

I would also like to express my gratitude to **Md. Bilal Siddiqui**, Physics teacher, for his excellent guidance throughout my life. Thank you for encouraging me with your kind words and for your kind help.

I would like to express my whole-hearted thanks to **Ruchi Singh** (Sister) for her trustworthy help, company, discussions and debates, assistance during fabrication and characterization processes, and most importantly her presence during my challenging times. Thanks to **Dr. Brajendra Singh Sengar and Dr. Vivek Garg** for their help in understanding the basics of the solar cell, its fabrication and characterization. My thanks also go to other lab members and colleagues **Dr. Amitesh Kumar, Dr. Rohit Singh, Dr. Aaryashree, Dr. Md Arif Khan, Dr. Ritesh Bhardwaj, Dr. Mangal Das, Dr. Biswajit Mandal, and future doctors Pawan Kumar, Sanjay Kumar, Jyoti Tiwari, Mayank**

Dubey, Chandrabhan Patel, and Sumit Chaudhary, who in one way or the other provided me assistance and motivation whenever required. I would also like to express my gratitude to my best friends **Sandeep Kumar (Bhai)** and **Ruchi Tomar** for continually inspiring me at various times.

I am deeply grateful to my family members: my parents, brother **Vivek Kumar**, sisters **Himani Pal and Ruchi Singh**, and sister in law **Megha Pal** for providing me unfailing support and continuous encouragement throughout my years of study and through the process of research and writing this thesis. Finally, I am honored to have attended the Inner Engineering program (Yogic Practice) offered by Isha Foundation under the guidance of **Sadhguru Jaggi Vasudev** for inner wellbeing.

GAURAV SIDDHARTH

Dedicated

To my parents, Bimla Devi and Rakesh Kumar

LIST OF PUBLICATIONS

List of Publications

A: Publications from PhD thesis work

A1. Peer-reviewed Journals

1. **Gaurav Siddharth**, Ruchi Singh, Vivek Garg, Brajendra S. Sengar, Mangal Das, Biswajit Mandal, Myo Than Htay, Mukul Gupta, and Shaibal Mukherjee, "Investigation of DIBS-deposited CdZnO/ZnO-based multiple quantum well for large-area photovoltaic application," **IEEE Transactions on Electron Devices**, vol. 67, no. 12, pp. 5587-5592, November 2020. **(Impact Factor: 2.913)**
2. **Gaurav Siddharth**, Brajendra S. Sengar, Vivek Garg, Md Arif Khan, Ruchi Singh, and Shaibal Mukherjee, "Analytical performance analysis of CdZnO/ZnO-based multiple quantum well solar cell," **IEEE Transactions on Electron Devices**, vol. 67, no. 3, pp. 1047-1051, March 2020. **(Impact Factor: 2.913)**
3. **Gaurav Siddharth**, Vivek Garg, Brajendra S. Sengar, Ritesh Bhardwaj, Pawan Kumar and Shaibal Mukherjee, "Analytical study of performance parameters of InGaN/GaN multiple quantum well solar cell," **IEEE Transactions on Electron Devices**, vol. 66, no. 8, pp. 3399-3404, June 2019. **(Impact Factor: 2.704)**

A2. Proceedings of International Conferences

1. **Gaurav Siddharth**, Ruchi Singh, Mayank Dubey, Myo Than Htay, and Shaibal Mukherjee, "Optimization of dual ion beam sputtered MQWs for solar cell," **48th IEEE Photovoltaic Specialist Conference (IEEE PVSC)**, Virtual Meeting, June 20- 25, 2021.

2. **Gaurav Siddharth**, Ruchi Singh, and Shaibal Mukherjee, "Modeling and Simulation of CdZnO/ZnO heterostructure based Multiple Quantum Wells for Photovoltaics," **37th European Photovoltaic Solar Energy Conference and Exhibition (EU PVSEC)**, Virtual meeting, September 7-11, 2020.

3. **Gaurav Siddharth**, Ruchi Singh, and Shaibal Mukherjee, "Modelling and Performance analysis of InGaN/GaN based Multiple Quantum Well solar cells," **47th IEEE Photovoltaic Specialist Conference (IEEE PVSC)**, Virtual Meeting, June 15-August 21, 2020.

4. **Gaurav Siddharth**, Ruchi Singh, and Shaibal Mukherjee, "Analytical Study of InGaN/GaN-Based Double Heterojunction *p-i-n* Solar Cell," **20th International Workshop on Physics of Semiconductor Device (IWPSD)**, December 17-20, 2019, IIT Kharagpur, India.

5. **Gaurav Siddharth**, Brajendra S. Sengar, Vivek Garg, Amitesh Kumar, Md. Arif Khan, and Shaibal Mukherjee, "Temperature dependent performance analysis of InGaN based *p-i-n* solar cell," **30th Annual General Meeting of MRSI and First Indian Materials Conclave**, IISc Banglore, India, February 12-15, 2019.

A3. Book Chapter

1. **Gaurav Siddharth**, Vivek Garg, Brajendra S. Sengar, and Shaibal Mukherjee, "Progress in Thin Film Solar Cell and Advanced Technologies for Performance Improvement," **Reference Module in Materials Science and Materials Engineering**, Elsevier, January, 2021.

B: Other publications during PhD

B1. Peer-reviewed Journals

1. Vivek Garg, Brajendra S. Sengar, **Gaurav Siddharth**, Shailendra Kumar, Victor V. Atuchin, and Shaibal Mukherjee, "Insights into the sputter-instigated valence plasmon oscillations in CIGSe thin films," **Surfaces and Interfaces**, vol. 25, p. 101146, August 2021. **(Impact Factor: 3.724)**
2. Brajendra S. Sengar, Vivek Garg, **Gaurav Siddharth**, Amitesh Kumar, Sushil Kumar Pandey, Mayank Dubey, Victor V. Atuchin, Shailendra Kumar, and Shaibal Mukherjee, "Improving the $Cu_2ZnSn(S,Se)_4$-based photovoltaic conversion efficiency by back contact modification," **IEEE Transactions on Electron Devices**, vol. 68, no. 6, pp. 2748-2752, June 2021. **(Impact Factor: 2.917)**
3. Ruchi Singh, Ritesh Bhardwaj, **Gaurav Siddharth**, Pawan Kumar and Shaibal Mukherjee, "Analytical study of sputter-grown ZnO-based *p-i-n*

homojunction UV photodetector," **IEEE Sensors Journal**, vol. 21, no. 6, pp. 7515-7521, January 2021. **(Impact Factor: 3.073)**

4. Pawan Kumar, Md Arif Khan, **Gaurav Siddharth**, Sanjay Kumar, Ruchi Singh, and Shaibal Mukherjee, "Electron scattering analysis in 2DEG in sputtering-grown MgZnO/ZnO heterostructure," **Journal of Physics D: Applied Physics**, vol. 53, no. 12, p. 125108, January 2020. **(Impact Factor: 2.890)**
5. Md Arif Khan, Pawan Kumar, **Gaurav Siddharth**, Mangal Das, and Shaibal Mukherjee, "Analysis of drain current in polycrystalline MgZnO/ZnO and MgZnO/CdZnO HFET," **IEEE Transactions on Electron Devices**, vol. 66, no. 12, pp. 5097-5102, December 2019. **(Impact Factor: 2.704)**
6. Vivek Garg, Brajendra S. Sengar, Amitesh Kumar, **Gaurav Siddharth**, Shailendra Kumar, and Shaibal Mukherjee, "Investigation of valence plasmon excitations in GMZO thin film and their suitability for plasmon-enhanced buffer-less solar cells," **Solar Energy**, vol. 178, pp. 114-124, January 2019. **(Impact Factor: 4.608)**
7. Biswajit Mandal, Sayan Maiti, Aaryashree, **Gaurav Siddharth**, Mangal Das, Ajay Agarwal, Apurba K. Das, and Shaibal Mukherjee, "Organo-di-benzoic-acidified ZnO nanohybrids for highly selective detection of CO at low temperature," **Journal of Physical Chemistry C**, vol. 124, pp. 7307-7316, March 2020. **(Impact Factor: 4.189)**
8. Mangal Das, Amitesh Kumar, Sanjay Kumar, Biswajit Mandal, **Gaurav Siddharth**, Pawan Kumar, Myo Than Htay, and Shaibal Mukherjee, "Impact of interfacial SiO_2 on dual ion beam sputtered Y_2O_3-based memristive system," **IEEE Transactions on Nanotechnology**, vol. 19, no. 153134, pp. 332-337, May 2020. **(Impact Factor: 2.196)**

B2. Proceedings of International Conferences

1. Ruchi Singh, **Gaurav Siddharth**, Ritesh Bharadwaj, and Shaibal Mukherjee, "Structural and Optical Study of Sputtered Grown Sb Doped ZnO Thin Film," **21st IEEE International Conference on Nanotechnology (IEEE NANO)**, Virtual Meeting, July 28-30, 2021.

2. Ruchi Singh, **Gaurav Siddharth**, Ritesh Bhardwaj, and Shaibal Mukherjee, "Structural Study of Sb doped ZnO Thin Film for Optical Applications," **5th International Conference on Emerging Electronics**, IIT Delhi, India, November 26-28, 2020.

3. Mayank Dubey, **Gaurav Siddharth**, Chandrabhan Patel, and Shaibal Mukherjee, "Effect of Sputtering Parameters on Molybdenum Back Contact for Chalcogenide Based Solar Cell Application," **5th International Conference on Emerging Electronics**, IIT Delhi, India, November 26-28, 2020.

4. Brajendra S. Sengar, Vivek Garg, **Gaurav Siddharth**, Nisheka Anadkat, Shailendra Kumar, and Shaibal Mukherjee, "Compositional Influence in the Photovoltaic Properties of Dual Ion Beam Sputtered $Cu_2ZnSn(S,Se)_4$ Thin Films," **20th International Conference on Renewable and Sustainable Energy (ICRSE)**, San Francisco, USA, June 6-7, 2018.

5. Vivek Garg, Brajendra S. Sengar, **Gaurav Siddharth**, Nisheka Anadkat, Shailendra Kumar, and Shaibal Mukherjee, "An Investigation on the Suitability of Dual Ion Beam Sputtered GMZO Thin Films: For All Sputtered Buffer-Less Solar Cells," **20th International Conference on Renewable and Sustainable Energy (ICRSE)**, San Francisco, USA, June 6-7, 2018.

6. Brajendra S. Sengar, Vivek Garg, **Gaurav Siddharth**, Md. Arif Khan, and Shaibal Mukherjee, "Band alignment study of Mg-doped ZnO/ CZTSSe heterojunction for Photovoltaic applications," **30th Annual General Meeting of MRSI and First Indian Materials Conclave**, IISc Banglore, India, February 12-15, 2019.

7. Vivek Garg, Brajendra S. Sengar, **Gaurav Siddharth**, Amitesh Kumar, Shailendra Kumar, and Shaibal Mukherjee, "Sputter-stimulated plasmonic excitations in GMZO thin films: For ultrathin photovoltaic applications," **30th Annual General Meeting of MRSI and First Indian Materials Conclave**, IISc Banglore, India, February 12-15, 2019.

8. Biswajit Mandal, Daya Shankar Sharma, **Gaurav Siddharth**, Ritesh Bhardwaj, Mangal Das, and Shaibal Mukherjee, "Surface Defective MoO_3

Nanofibers Towards Highly Sensitive Ethanol Detection," **30^{th} Annual General Meeting of MRSI and First Indian Materials Conclave**, IISc Banglore, India, February 12-15, 2019.

9. Vivek Garg, Brajendra S. Sengar, Nisheka Anadkat, **Gaurav Siddharth**, Shailendra Kumar, and Shaibal Mukherjee, "Evaluation of Ga:MgZnO/CIGSe heterojunction for realization of all sputtered buffer-less solar cell," **19^{th} International Workshop on The Physics of Semiconductor Devices (IWPSD)**, IIT Delhi, India, December 11-15, 2017.

10. Md Arif Khan, Pawan Kumar, Mangal Das, **Gaurav Siddharth**, and Shaibal Mukherjee, "Analytical model for DC characterizations of ZnO based HFET utilizing interface states density modulation," **10^{th} International Conference on Materials for Advanced Technologies (ICMAT)**, Singapore, June 23-28, 2019.

TABLE OF CONTENTS

LIST OF FIGURES

LIST OF TABLES

ACRONYMS

PV	*Photovoltaic*
AM	*Air Mass*
FF	*Fill Factor*
I-V	*Current-Voltage*
J-V	*Current density-Voltage*
P-V	*Power density-Voltage*
SC	*Solar Cell*
MQWSC	*Multiple quantum well solar cell*
MJSC	*Multiple junction solar cell*
ASTM	*American Society for Testing and Materials*
DIBS	*Dual Ion Beam Sputtering Deposition*
DPC	*Deposition Chamber*
LLC	*Load Lock Chamber*
MOCVD	*Metal organic chemical vapour deposition*
MOVPE	*Metal organic vapour phase epitaxy*
RTCVD	*Rapid thermal chemical vapour deposition*
PVD	*Physical Vapor Deposition*
AZO	*Al-doped ZnO*
ZnO	*Zinc Oxide*
ZnInON	*Zinc Indium Oxide Nitride*
CdZnO	*Cadimum Zinc Oxide*
MgZnO	*Magnesium Zinc Oxide*
GZO	*Ga-doped Zinc Oxide*
SZO	*Sb-doped Zinc Oxide*
GaN	*Gallium Nitride*
InGaN	*Indium Gallium Nitride*
GaAs	*Gallium Arsenide*
RF	*Radio Frequency*
OPTR	*Optical recombination and generation*
HFET	*Heterostructure field effect transistor*

LED	*Light emitting diode*
STC	*Standard Test Condition*
SE	*Spectroscopic Ellipsometry*
SIMS	*Secondary Ion Mass Spectroscopy*
HRTEM	*High-Resolution Transmission Electron Microscopy*
EDX	*Energy Dispersive X-ray*
FESEM	*Field emission scanning electron microscope*
XRD	*X-Ray diffraction*
HF	*Hydrofluoric*
DI	*Deionized Water*
TCE	*Trichloroethene*
DC	*Direct Current*

NOMENCLATURE

h	*Plank's Constant*
c	*Speed of light*
λ	*Wavelength*
V_{oc}	*Open Circuite Voltage*
J_{sc}	*Short Circuit Current Density*
P_m	*Maximum power density*
P_{in}	*Incident power*
η	*Conversion Efficiency*
J_s	*Reverse saturation current density*
V_t	*Thermal Voltage*
L_n and L_p	*Diffusion length of electrons and holes*
D_n and D_p	*Diffusion constants for electrons and holes*
W	*Depletion region width*
E_g	*Energy bandgap*
E_{g0}	*Energy bandgap at 0 K*
b	*Bowing parameter*
α	*Absorption Coefficient*
ψ	*Wave function*
k	*Wave vector*
E_n	*Quanized energy*
m^*	*Effective mass*
ρ	*Density of states*
a	*Lattice parameter*
$N_{ph}(\lambda)$	*Spectral photon flux*
$P(\lambda)$	*Spectral power density*
I	*Irradiance*
k_B	*Boltzman constant*
R_s and R_e	*Radii of the Sun and Earth*

ABSTRACT

Theoretical and Experimental Investigation of Multiple Quantum Wells for Photovoltaic Applications

by

Gaurav Siddharth

Hybrid Nanodevice Research Group, Department of Electrical Engineering

Indian Institute of Technology Indore

Supervisor: Dr. Shaibal Mukherjee

There are certain losses associated with the single junction solar cell such as, thermalization loss, transmission loss, recombination loss and blackbody radiation loss, most of which can be minimized by using multiple energy bands technologies, i.e. multiple quantum well solar cell (MQWSC). Alternatively, this MQWSC technology can be integrated with the multiple junction solar cell (MJSC) to absorb the different part of the solar spectrum more efficiently. As, in MJSC minimum of the current from all the sub-cells will be delivered. Therefore, by inserting multiple quantum well in the sub-cells which is generating low current, this issue in MJSCs can be resolved up to some extent. In MQWSC, transport mechanism of charge carrier is mainly thermally activated, thus these are estimated to show a better conversion efficiency at high temperature than the conventional cells and therefore, makes them more feasible for concentrated solar cell applications.

Before the actual experimental fabrication of the MQWSC, it is vital to accomplish theoritcal study of the performance parameters of the MQWSC under different conditions. Therefore, an analytical and simulation study has to be commenced to evaluate the performance parameters that will be expected from MQWSC under various conditions. First, analytical model is developed for the *p-i-n* structure, as MQWSC is just the extension of *p-i-n* structure in which MQWs are inserted in the intrinsic region. Then, an

analytical model is developed for the MQWSC. In the developed models, significantly the spectral irradiance available from American Society for Testing and Materials (ASTM) standards data sheets is used for realising photon flux density instead of commonly used Planck's blackbody radiation law. Further, the photon flux density is utilized to evaluate the performance parameters of MQWSC and bulk p-i-n solar cell.

The developed model of MQWSC is further compared with the published experimental data obtained by other reasearchers on the same technology. In comparision, the material and structural properties of the published experimental researches are utilized to obtain the results from analytical model. The close aggrement of the analytically obtained results with that of the published experimental results by other researches validate the analytical model.

Next, based on the developed models, the analysis has been performed for different composition of indium in $In_xGa_{1-x}N$ well layers on performance parameters of InGaN/GaN-based MQWSC since InGaN is a well-established material for the high bandgap device technology. As the temperature of operation also has a substantial influence on solar cell performance, an extensive discussion on the temperature dependence of the performance parameters of the *p-i-n* and MQW solar cell is performed. The analysis has also been performed to study the impact of number of quantum well variation on device performance parameters. Results suggest that by incorporating quantum wells in the intrinsic region (x = 0.1 in $In_xGa_{1-x}N$), ~27 % increment in the conversion efficiency can be achieved as compared to that from the bulk solar cell. Moreover, the rise in temperature leads to the increase in short circuit current density; however, open circuit voltage and conversion efficiency decreases. A decrement of ~9.7 % in the conversion efficiency of MQWSC is observed with the rise in temperature from 200 to 400 K as compared to ~11.6 % decline in *p-i-n* solar cell.

Additionally, the CdZnO/ZnO-based MQWSC has been proposed and its performance is studied under various conditions such as cadmium composition variation and operation temperature variation. The results show that, for the proposed CdZnO/ZnO-based MQWSC, the open-circuit voltage (V_{oc}) has a negative temperature coefficient (-2.63 mV/˚C), and short-circuit current density (J_{sc}) and conversion efficiency (η) have positive temperature coefficients of 2.43×10^{-3} mA/cm^2.˚C and 2.91×10^{-3} %/˚C, respectively.

Furthermore, the influence of solar irradiance on the performance parameters and *J-V* characteristics of MQWSC is examined by modifying the developed model i.e. by including the effect of solar irradiance in the previously developed model. For CdZnO/ZnO-based MQWSC, the short-circuit current density increases from 0.12 to 57.98 mA/cm^2, open circuit voltage rises from 2.60 to 2.77 V and photon conversion efficiency from 2.85 to 3.04 %, as solar irradiance increases from 0.1 to 50 suns.

Next, optimization of CdZnO/ZnO-based Multiple quantum wells (MQWs) realized for the first time by dual ion beam sputtering (DIBS) at different deposition conditions in terms of ion beam power, substrate temperature, and time cessation between deposition of successive layers is performed. The effects of DIBS deposition conditions are analyzed by spectroscopy ellipsometry (SE), secondary ion mass spectroscopy (SIMS) and high-resolution transmission electron microscopy (HRTEM) and discussed systematically. The SIMS and HRTEM analysis have been used for depth profiling at high resolution of CdZnO/ZnO-based MQWs structure. The deposition of CdZnO/ZnO-based MQW structure performed at 100 °C, with time cessation of 30 min between successive layer growth and ion beam power of 14 W has displayed the best results in terms of distinct well and barrier layers formation.

Chapter 1

Introduction and Fundamental Concepts

1.1. Energy

On earth there are two major types of energy: renewable and non-renewable. The utilization of the non-renewable energy resources such as coal, petroleum, diesel etc. leads to their depletion and also these energy sources contributes to pollution (greenhouse gases and other by-products) of the environment. The higher growth rate of the population, urbanization and industrialization have resulted in the increase in demand of energy supply. Therefore, there is a drastic increase in the consumption of the non-renewable energy resources, resulting in there depletion on earth at a much faster rate. Therefore, innovative approach to utilize renewable energy resources such as solar energy, hydropower energy, wind energy etc. to their fullest must be explored to meet the demand supply of energy, as they are environment friendly non-polluting unlimited source of energy [1].

Solar energy is certainly the most prominent renewable energy, owing to its versatility, inexhaustible and environmental friendly features and it has potential to complete world’s energy demand supply chain. 1 hour of solar energy is sufficient to complete human annual energy requirement and also it is the energy source for almost all the processes happening on the surface of our planet. Solar energy technologies such as photovoltaic (PV) deals with, or is a section of research focusing on the direct conversion of solar energy into electrical energy [2].

The major challenges in the path of solar cell becoming a primary source of energy are its high costs and low conversion efficiency. In the last decade or so, major research is done with the motive of improving the conversion efficiency of solar cells by investigating new technologies such as multi-junction solar cells and multiple quantum well solar cell to utilize full solar spectrum more efficiently, and also by using new materials for manufacturing solar cells [3].

1.2. Fundamentals of Solar Cell

1.2.1 Solar Spectrum:

Sun emits electromagnetic radiation particular in ultraviolet, visible and infrared region. The sunlight is composed of energetic particles called photons. Every photon has its own energy that depends on the wavelength of the incoming light and is expressed by the Planck-Einstein relation [3]:

$$E = hc/\lambda \tag{1.1}$$

where h - Planck constant, c - speed of light, and λ - light wavelength. Figure 1.1 shows the solar spectral irradiance in terms of the wavelength of photons for terrestrial and space application. The dashed lines indicated the boundaries of the ultraviolet, visible and infrared part of the spectrum. The ultraviolet region covers only 5 % of the spectrum, while visible and infrared region covers 46 %and 49 % of the spectrum respectively [4].

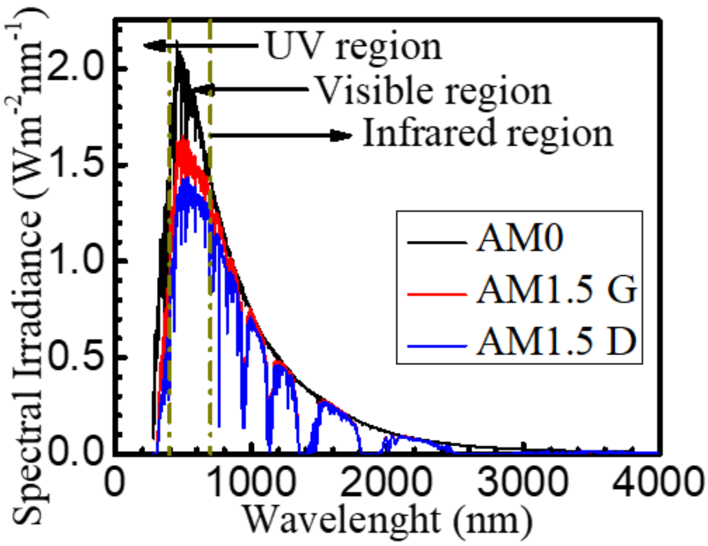

Figure 1.1 *Solar Spectrum for terrestrial (AM1.5) and space application (AM0).*

A large fraction of the solar spectrum is absorbed by the specific molecules in earth's atmosphere such as water, carbon dioxide, oxygen and ozone [3]. Therefore, there is difference in the solar spectrum available outside of Earth's atmosphere and at the sea level of Earth.

1.2.2 Air Mass (AM):

The important parameter that governs the change of the solar spectral irradiance (spectral power density) with the distance it covers through the atmosphere is air mass. The distance covered by the spectral irradiance is shortest only when the sun is directly overhead i.e. at the zenith position.

The ratio of an actual path length (l) travel by the solar spectral irradiance through the atmosphere to the shortest distance (l_0) is known as the optical air mass or commonly air mass. The air mass corresponding to the sun having an angle theta (θ) with the zenith is given by [5, 6]

$$AM = 1/\cos\theta = l/l_0 \quad (1.2)$$

The figure 1.2 shows the sun at its zenith position. As it illuminates earth, light travels through the four main layers of earth's atmosphere. Excluding the exosphere, these layers are the troposphere, stratosphere, mesosphere and thermosphere.

With the sun at its zenith position the air mass becomes unity, and the corresponding spectrum is represented by AM1. AM0 represents the solar spectral irradiance available outside the Earth's atmosphere and is utilized for space application having the integrated power of 1361 W/m^2. For the evaluation of solar cells performance fabricated all over the world, the AM1.5 is preferred as a standard for terrestrial application that corresponds to an angle of 48.2° between the sun actual position and zenith position. Moreover, if the sun is at 60° to zenith position, the spectrum received is AM2 [3].

The solar spectral irradiance that reaches the Earth can be considered in two modules: direct (the spectral irradiance that reaches directly to the Earth) and diffuse (the spectral irradiance that is scattered by Earth's atmosphere). There is a distinct representation of these spectrums: AM1.5G signifying a global radiation (consider all the components of sunlight) and AM1.5D (consider only direct radiation). Generally, AM1.5G is used as a standard spectrum having solar irradiance of 1000 W/m^2 [3].

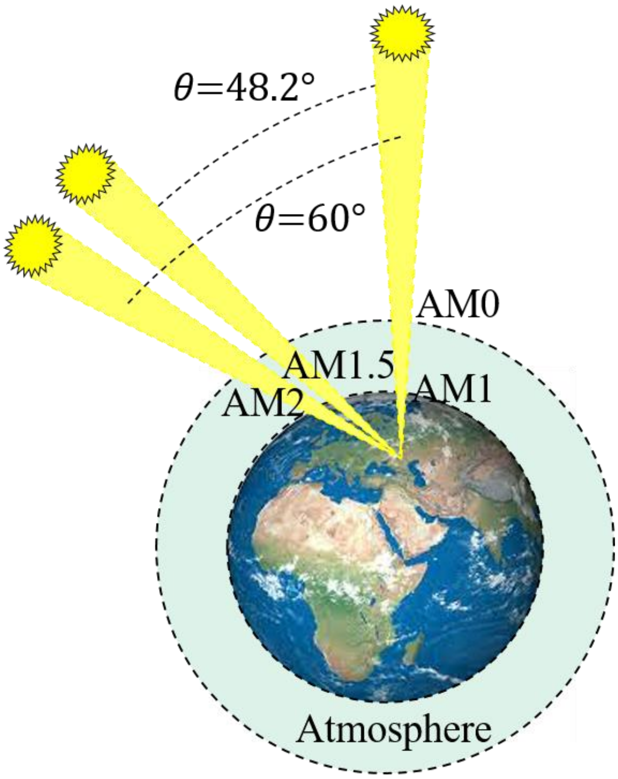

Figure 1.2 *Air Mass at various sun position with respect to its zenith position.*

1.2.3 Working Principle:

The working of solar cell is based on the photovoltaic effect i.e. by directly converting sunlight into electricity. The solar energy conversion flow is basically consists of three process [3] as depicted in Figure 1.3:

Figure 1.3 *Process flow of solar energy conversion.*

1.2.3.1 Generation of Charge Carrier: The first process is the generation of charge carriers by the absorption of photons in the materials that form the *p-n* junction. The photons having energy greater than or equal to the energy bandgap of the material, leads to the generation of charge carriers, on the other hand, lesser energy photons passes through the material without being absorbed and will not contribute to the charge carrier generation. As a result of this carrier generation process, electron hole pair is generated. In this generated pair, electron moves to the higher energy state (conduction band) leaving behind the hole in the lower energy state (valence band) shown in Figure 1.4 (a).

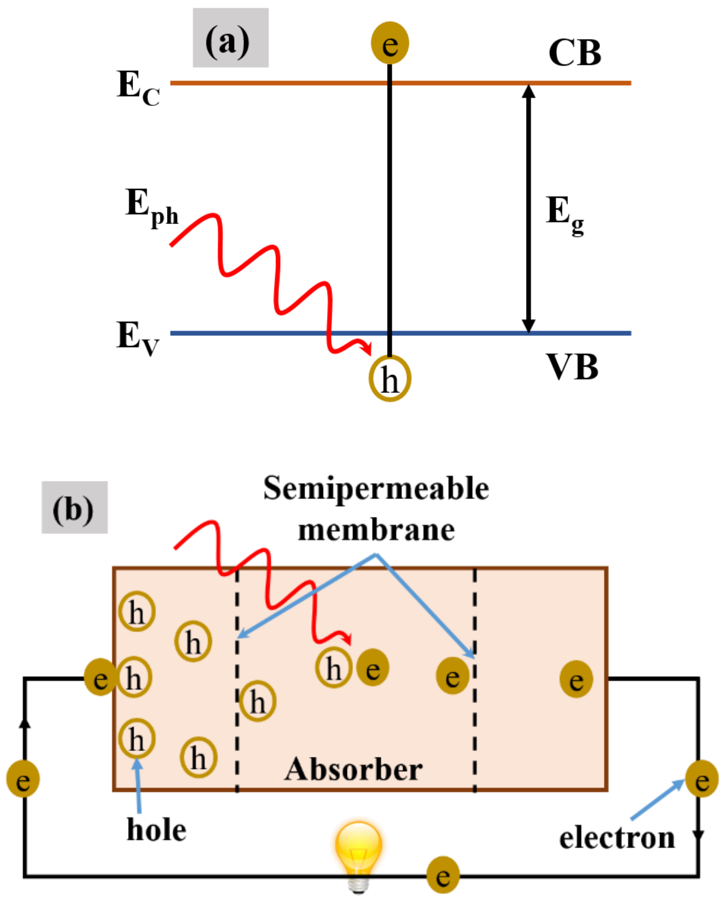

Figure 1.4 *(a) Energy band diagram showing generation of charge carrier by the absorption of photons (b) Simple solar cell model showing separation of charge carrier via semipermeable membrane and followed by collection of charge carrier and then flow of electron through external circuit.*

1.2.3.2 Separation of Charge Carrier: After carrier lifetime, recombination of charge carrier may occur, therefore the generated charge carrier must be separated before the recombination to generate electricity. In order to separate them, the semipermeable membranes must be present on the both side of the absorber layer, so that electron can flow through one and hole through the other as is shown in the

Figure 1.4 (b). These membranes are basically formed by the *p*- and *n*-type materials.

1.2.3.3 Collection of Charge Carrier: In the final process, the separated charge carriers are collected at the contacts, so that electrons can flow through the external circuit to generate electricity and after passing through the circuit, they recombine with the holes at the other contact as is shown in the Figure 1.4 (b).

1.2.4 Performance Parameters:

The solar cell device functions in the fourth quadrant, indicating negative current density but positive voltage, therefore producing the negative power i.e. the device produces power by utilizing the incident solar irradiance on the device. The illuminated current density of the *p*-*n* junction solar cell under the applied voltage is given by

$$J = J_s \left[exp\left(\frac{V}{V_t}\right) - 1 \right] + J_{sc} \tag{1.3}$$

where V_t is thermal voltage, J_s is reverse saturation current density and V is terminal or bias voltage.

The performance parameters of solar cell that are used to characterize it are short circuit current density (J_{sc}), open circuit voltage (V_{oc}), fill factor (FF) and maximum peak power density (P_m). These parameters are obtained from the illuminated current density vs voltage (*J*-*V*) curve as shown in Figure 1.5.

1.2.4.1 Short Circuit Current Density, J_{sc}: The current per unit area that flows through the external circuit because of the generated electron-hole pairs due to incident photons, when the device is short-circuited is called short-circuit current density. J_{sc} is directly proportional to the incident photon flux density. This is the maximum current density delivered by the solar cell. Under uniform generation rate (G), the short circuit density of the *p*-*n* junction solar cell is given by

$$J_{sc} = qG(L_n + L_p + W) \tag{1.4}$$

where Lp and Ln are the minority-carriers diffusion length of holes and electrons, respectively, and W is depletion region width. The above mentioned equation suggests that the charge carriers generated in the depletion region of the *p-n* junction and also in the areas extended till minority-carrier diffusion length from the edges of depletion region in both *p* and *n* semiconductor can contribute to the short circuit current density.

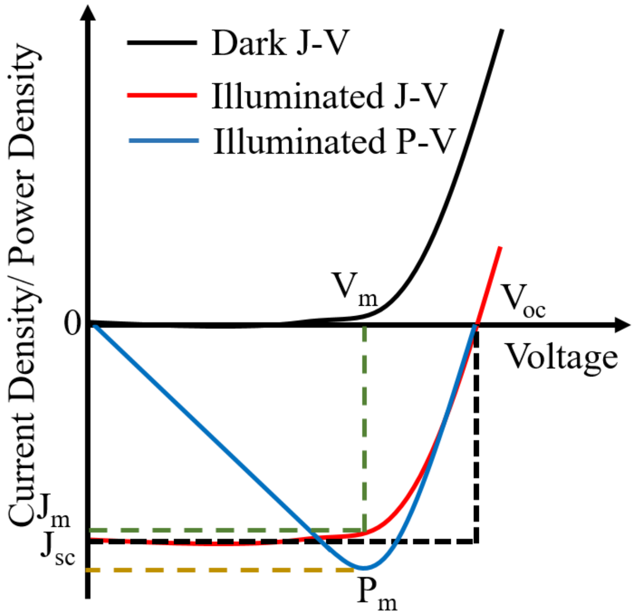

Figure 1.5 *J-V and P-V characteristics of the p-n junction solar cell in the dark and under illumination.*

1.2.4.2 Open Circuit Voltage, V_{oc}: The voltage developed at the terminals of the solar cell when they are open and the net flow of current through the external circuit is zero is called Open circuit voltage. This is the maximum voltage that can be produced by a solar cell and it corresponds to the forward bias voltage, at which short circuit current density is compensated by dark current density. V_{oc} is calculated using the following equation:

$$V_{oc} = V_t ln\left(\frac{J_s - J_{sc}}{J_s}\right) \tag{1.5}$$

1.2.4.3 Maximum power density, P_m: This is the maximum power density that can be generated by the solar cell and is marked as P_m on the *P-V* curve in figure 5. The current density and voltage corresponding to the maximum power density defines the maximum power point. This voltage and current density should be the operating point for the solar cell to deliver maximum power.

1.2.4.4 Fill Factor, *FF*: It is the ratio of maximum power density produced by the solar cell to the product of J_{sc} and V_{oc}.

$$FF = \frac{P_m}{V_{oc}J_{sc}} \tag{1.6}$$

1.2.4.5 Conversion efficiency, *η*: It is the ratio of maximum power density generated to the incident power density of the solar spectrum.

$$\eta = \frac{P_m}{P_{in}} \tag{1.7}$$

1.2.5 Conversion Efficiency Limit:

The maximum theoretically achievable conversion efficiency limit from single *p*-*n* junction solar cell was calculated by Shockley and Queisser and is found to be 33.7% for bandgap of 1.34 eV [7]. But the mass production of silicon with indirect bandgap of 1.1 eV limits the theoretically conversion efficiency to 29.43% under 1 sun AM1.5G illumination [8]. The major losses that are considered in the Shockley and Queisser limit are thermalization loss of photons above the energy bandgap of the semiconductor and non-absorbed photon loss below energy bandgap of the semiconductor. The calculations are performed using the detailed balance principle by considering several assumptions:

- ❖ Single semiconductor material and one *p*-*n* junction per solar cell
- ❖ Single photon creates single electron-hole pair
- ❖ All photons with the energy more than the energy bandgap of the used semiconducting material, are absorbed and while, the energy of the photon left after the e-h pair generation process is converted to heat
- ❖ A non-concentration sunlight source is considered
- ❖ Only radiative recombination of the charge carriers inside the *p*-*n* junction is assumed

The detailed Shockley and Queisser limit for AM0, AM1.5 and blackbody spectrum at 6000K are shown in Figure 1.6.

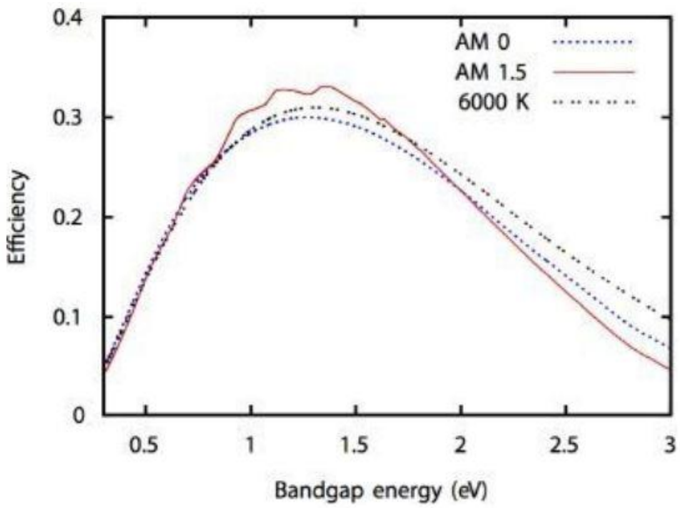

Figure 1.6 *The Shockley-Queisser efficiency limit for the blackbody spectrum at 6,000 K, and the AM0 and AM1.5 solar spectra [3].*

1.2.6 Generations of Solar Cell:

Solar cells are broadly classified into three generations based on the technology and material. The research is being carried out in all the three generations to further improve the conversion efficiencies of the solar cell of respective generations.

1.2.6.1 First generation solar cell: This generation includes the single junction solar cell made from amorphous, mono- and poly-crystalline silicon used as semiconducting material. As the silicon has low absorption coefficient and indirect energy bandgap, relatively thick absorber layer (> 100 μm) is required, which leads to the increased cost and non-flexible devices. Although it covers large part of the solar spectrum, the part of high energy photons of the spectrum is wasted as heat. High quality, large area and single *p-n* junction devices are the key features of the first generation solar cells.

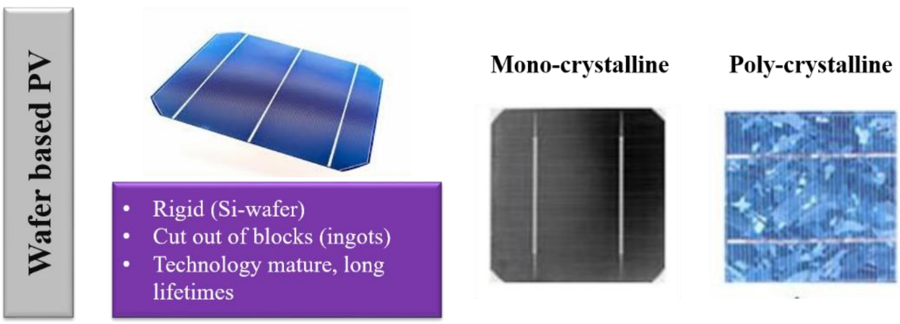

Figure 1.7 *First generation solar cell.*

1.2.6.2 Second generation solar cell: The first generation solar cells have a foremost issues of production costs which is most important attention in development of second generation thin-film solar cell technology. The material costs can be reduced by introducing absorber layer of thickness less than 5 μm and eradicating the silicon wafer in the thin-film technology. Reduction in the absorber layer thickness is possible by utilizing the direct energy bandgap and high absorption coefficient semiconducting materials. Another main focus of thin film technology is to bridge the gap of energy conversion efficiency with the first generation solar cells. The commonly used materials in the thin film technology are cadmium telluride, amorphous silicon, and copper indium gallium selenide. Although, these technologies comprises very low percentage of commercial production. But, the future of thin-film technology appears to be encouraging with the development of new materials over the coming decades.

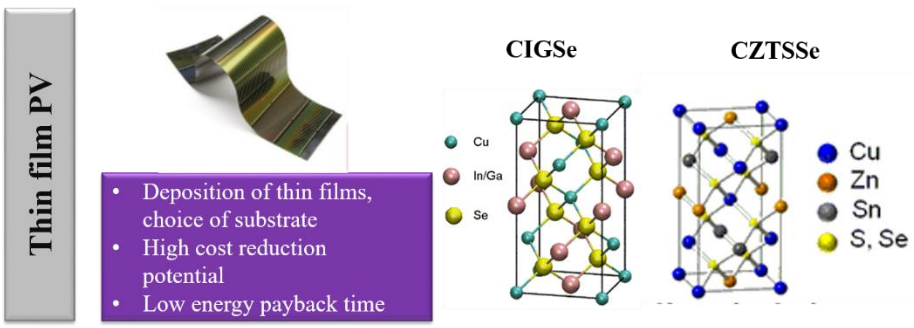

Figure 1.8 *Second generation solar cell.*

1.2.6.3 Third generation solar cell: This generation refers to the novel technologies, aiming to overcome Shockley and Queisser limit. The third generation solar cells concepts includes intermediate band solar cell, quantum well solar cell, tandem/multi junction solar cell, hot-carrier cells, spectral up and down conversion technologies, concentrator photovoltaic and solar thermal technologies like thermo-photonics. Many researchers are focussing in the development of efficient solar cells combining the second and third generation technologies of solar cell and a very advance breakthrough is expected in the near future.

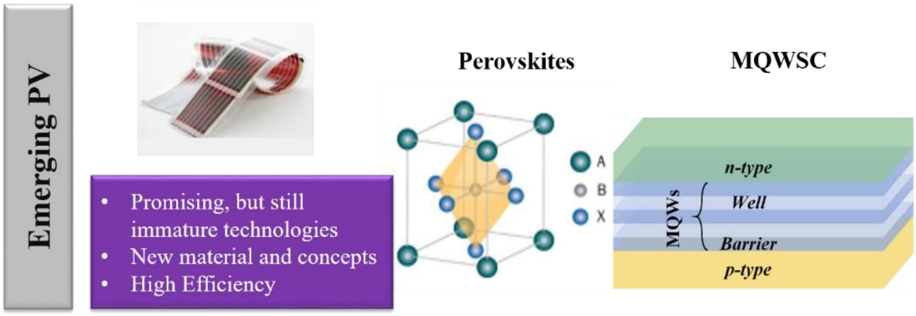

Figure 1.9 *Third generation solar cell.*

1.3. Motivation

There are certain losses associated with the single junction solar cell, most of which can be overcome or minimized by using multiple energy bands technologies, i.e. multiple quantum well solar cell (MQWSC) which is studied extensively in the past few decades [9-18]. These losses are described with the help of energy band diagram shown in Figure 1.10 and are explained as follows:

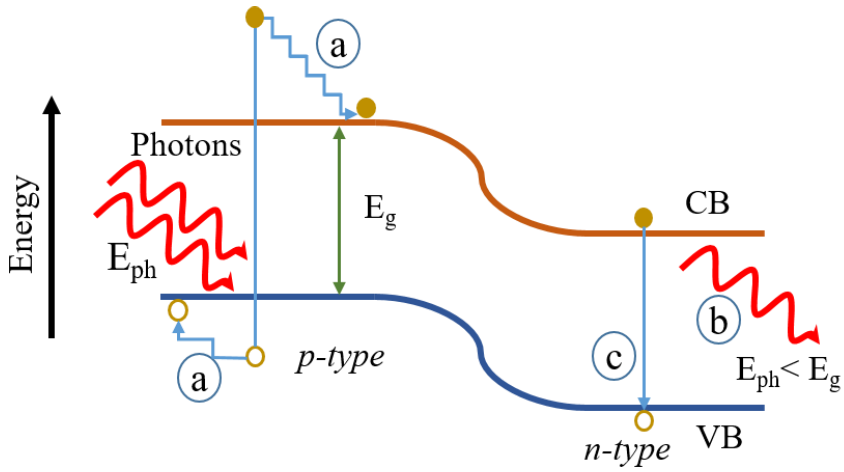

Figure 1.10 *Losses associated single p-n junction solar cell depicted with the help of energy band diagram.*

❖ Thermalization loss: In this case the energy of incident photon is larger than the bandgap of the material, so the extra energy apart from the energy bandgap of the absorber material is lost in terms of heat, shown in Figure 1.10 by process (a).

❖ Transmission loss: Certain photons have their energy less than the energy bandgap of the absorber material, such photons are incapable of providing any power in the generation process and they simply pass through the absorber material without getting absorbed, shown in Figure 1.10 by process (b).

❖ Recombination loss: In this case electron hole pair are generated but before being collected for the generation of electricity they get recombine providing zero contribution in conversion efficiency, shown in Figure 1.10 by process (c).

❖ Blackbody radiation loss: This loss occurs in every material object if the temperature of operation is above 0 K.

The efficiency of any single-junction solar cell is inherently limited by these losses. If these fundamental losses could be overcome, the PV technology could be developed to achieve higher conversion efficiency exceeding the Shockley-Queisser limit [3, 19].

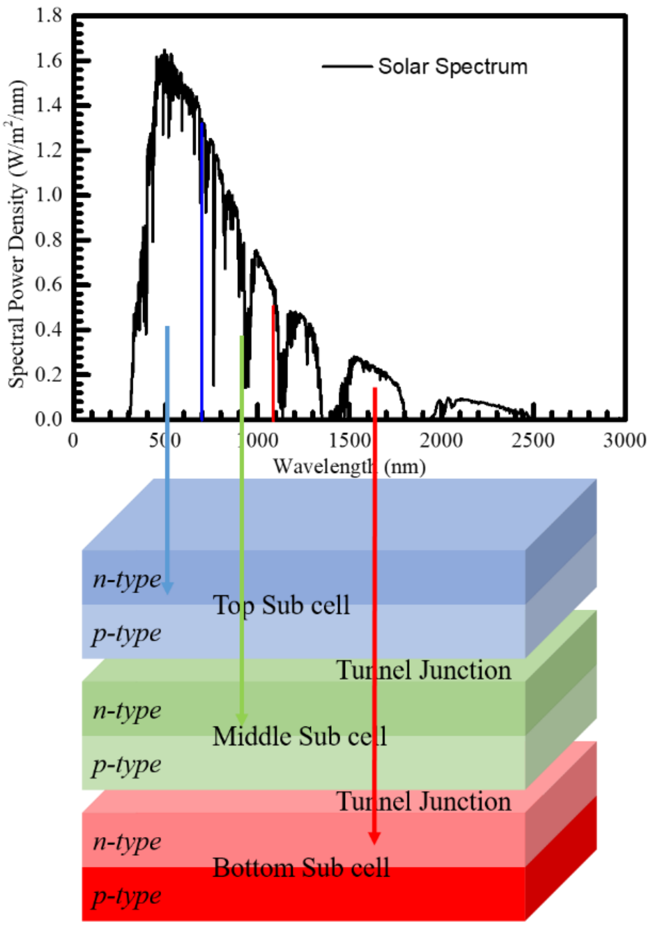

Figure 1.11 *Different region of the solar spectrum is absorbed in different sub cells of the MJSC.*

Alternatively, this multiple quantum well solar cell technology can be integrated with the multi junction solar cell, so that the whole solar spectrum can be utilized efficiently [20-23]. The top cell in the multiple junction solar cell (MJSC) structure absorbs lower wavelength photons corresponding to the high energy bandgap of the material and allow the higher wavelength photons to pass through it. The higher wavelength photons are absorbed in the middle or bottom cells depending on the energy bandgap values of the corresponding material. The bottom cell has the lowest energy bandgap, therefore absorb long wavelength photons, which are transmitted from the above sub cells. This whole process is explained with the help of Figure 1.11, in which different region of the solar spectrum is absorbed by 3 junction solar cell.

In MJSC, different part of the spectrum is absorbed by the different sub-cells, but as the spectrum is not constant throughout the wavelength range so the different amount of current is produced by the different sub-cell. However, to have maximum benefits the current must be the approximately same in all the sub-cells of MJSCs, otherwise minimum of the current from all the sub-cells will be delivered. And this issue in MJSCs can be resolved up to some extent by inserting multiple quantum well in the sub-cells which is generating low current [20, 21].

In conventional or bulk solar cells and also if the solar cells are used under concentrated sunlight, the prime concern is the performance degradation with the increase in device temperature. Since in MQWSC, transport mechanism of charge carrier from quantum wells is mainly thermally activated, thus MQWSC are estimated to show a better performance at high temperature than the conventional solar cells. This advantage of better performance at high temperature, makes them more feasible for concentrated solar cell applications [24, 25].

These are reason, behind the rigorous research on MQWSC both theoretically and experimentally in the past few decade [9-14].

1.4. Problem Formulation and Execution Plan

The objective of this work is to analyse the multiple quantum well for photovoltaic application both theoretically and experimentally. Before the actual experimental fabrication of the MQWSC, it is vital to accomplish an analytical and simulation study of the performance parameters of the MQWSC under different conditions. Therefore, an analytical and simulation study has to be commenced to evaluate the performance parameters that will be expected from MQWSC under various conditions. As, fabrication of MQW involves multiple layers deposition of few nanometres thickness, therefore its optimization is crucial and is performed by varying various deposition parameters. The execution plan of the work are as follows:

1) Before, developing analytical model for MQWSC, analytical model is developed for the *p*-*i*-*n* structure, as MQW are just inserted in the intrinsic region of the *p*-*i*-*n* structure.

2) Then, an analytical model is developed for the MQWSC. In the developed models, the spectral irradiance available from American Society for Testing and Materials (ASTM) standards data sheets is used for realising photon flux density instead of commonly used Planck's blackbody radiation law. This obtained photon flux density is further used for evaluating the performance parameters of the solar cell.

3) Based on the developed models, the analysis has been performed for different composition of indium in $In_xGa_{1-x}N$ well layers on performance parameters of InGaN/GaN-based MQWSC since InGaN is a well-established material for the high bandgap device technology. After this, analysis is also performed for the proposed CdZnO/ZnO-based MQWSC by varying cadmium composition in CdZnO.

4) As the temperature of operation has a substantial influence on solar cell performance, an extensive discussion on the temperature

dependence of the performance parameters of the *p-i-n* and MQW solar cell is performed.

5) The analysis has also been performed to study the impact of number of quantum well variation on device performance parameters.
6) Furthermore, the influence of solar irradiance on the performance parameters and J-V characteristics of MQWSC is examined by modifying the developed model i.e. by including the effect of solar irradiance in the previously developed model.
7) Optimization of CdZnO/ZnO-based MQWs deposited for the first time by dual ion beam sputtering (DIBS) at different deposition conditions such as substrate temperature, ion beam power and cessation time is performed.
8) Analysis of the deposited MQWs is performed using Spectroscopy Ellipsometry, Secondary Ion Mass Spectroscopy and High Resolution Transmission Electron Microscopy.

1.5. Thesis Organization

The research in this thesis describe the analytical modelling, silvaco atlas simulation, fabrication and measurement of MQWs for photovoltaic application to enhance solar cell performance. Based on this, the thesis is organised as follows:

Chapter 1 presents the introduction of solar cell and the associated performance parameters with it. And also discuss the motivation behind the analysis of MQWSC.

Chapter 2 discuss the physics of the quantum well, recent development in MQWSC and state of the art research in thic field.

Chapter 3 demonstrates the analytical model developed to investigate the performance of InGaN/GaN-based *p-i-n* solar cell. As the indium composition in the InGaN intrinsic material changes the energy bandgap therefore its study is performed. Additionally, the effect of operation temperature has been analysed on the performance parameters of the solar cell.

Chapter 4 describes the analytical model developed for the MQWSC. Thereafter, the analysis has been performed to examine the performance of InGaN/GaN-based MQWSC. An extensive discussion of the different composition of InGaN materials in the well layers, operation temperature and number of quantum wells on the performance parameters of MQWSC has been performed. Moreover, the influence of solar irradiance on the performance parameters and J-V characteristics of MQWSC is explored by modifying the developed model corresponding to solar irradiance. Additionally, the CdZnO/ZnO-based MQWSC has been proposed and its performance is studied under various conditions.

Chapter 5 illustrates the deposition and several characterization techniques employed for CdZnO/ZnO-based MQWs. The thin films are deposited by DIBS system, and characterizations are performed by Secondary Ion Mass Spectroscopy, High Resolution Transmission Electron Microscopy and Spectroscopic Ellipsometry (SE).

Chapter 6 focuses on the optimization of substrate temperatures, ion beam power and cessation time for the deposition of CdZnO/ZnO-based MQWs for photovoltaics application.

Chapter 7 illustrates the summary of the research work from the thesis and proposes the scope for future works for the continuation of the research on this topic.

1.6. References

[1] M. A. Green, “Commercial progress and challenges for photovoltaics,” Nature Energy, vol. 1, no. 1, p. 15015, 2016.

[2] G. W. Crabtree and N. S. Lewis, "Basic research needs for solar energy utilization," 2005.

[3] A. H. Smets, K. Jager, O. Isabella, R. A. Swaaij, and M. Zeman, “Solar energy: The physics and engineering of photovoltaic conversion, technologies and systems,” Cambridge: Cambridge University Press, 2015.

[4] “Solar Cell Basics” [Online] http://solarcellcentral.com/index.html.

[5] M. A. Green, “Solar cells: Operating principles, technology, and system applications,” Englewood Cliffs, NJ, Prentice-Hall, Incorporation, p. 80, 1982.

[6] Würfel, Peter, and Uli Würfel, “Physics of solar cells: from basic principles to advanced concepts,” John Wiley & Sons, 2016.

[7] W. Shockley and H. J. Queisser, “Detailed Balance Limit of Efficiency of p-n Junction Solar Cells,” Journal of Applied Physics, vol. 32, no. 3, pp. 510-519, 1961.

[8] A. Richter, M. Hermle, and S. W. Glunz, "Reassessment of the limiting efficiency for crystalline silicon solar cells," IEEE Journal of Photovoltaics, vol. 3, no. 4, pp. 1184-1191, 2013.

[9] K. W. J. Barnham, and G. Duggan, “A new approach to high-efficiency multi-band-gap solar cells,” Journal of Applied Physics, vol. 67, no. 7, pp.3490-3493, 1990.

[10] S. M. Ramey, and R. Khoie, “Modeling of multiple-quantum-well solar cells including capture, escape, and recombination of photoexcited carriers in quantum wells,” IEEE Transactions on Electron Devices, vol. 50, no. 5, pp.1179-1188, 2003.

[11] N. G. Anderson, “Ideal theory of quantum well solar cells,” Journal of Applied Physics, vol. 78, no. 3, pp.1850-1861, 1995.

[12] E. Aperathitis, A. C. Varonides, C. G. Scott, D. Sand, V. Foukaraki, M. Androulidaki, Z. Hatzopoulos, and P. Panayotatos, “Temperature dependence of photocurrent components on enhanced performance GaAs/AlGaAs multiple quantum well solar cells,” Solar Energy Materials and Solar Cells, vol. 70, no. 1, pp.49-69, 2001.

[13] R. Dahal, J. Li, K. Aryal, J. Y. Lin, and H. X. Jiang, “InGaN/GaN multiple quantum well concentrator solar cells,” Applied Physics Letters, vol. 97, no. 7, p.073115, 2010.

[14] B.W. Liou, “Temperature of InxGa1− xN/GaN solar cells with a multiple-quantum-well structure on SiCN/Si (111) substrates,” Solar Energy Materials and Solar Cells, vol. 114, pp.141-146, 2013.

[15] B. Behaghel, R. Tamaki, N. Vandamme, K. Watanabe, C. Dupuis, N. Bardou, H. Sodabanlu, A. Cattoni, Y. Okada, M. Sugiyama, and S. Collin, "Absorption enhancement through Fabry-Pérot resonant modes in a 430 nm thick InGaAs/GaAsP multiple quantum wells solar cell," Applied Physics Letters, vol. 106, no. 8, p.081107, 2015.

[16] Y. Wen, Y. Wang, K. Watanabe, M. Sugiyama, and Y. Nakano, "Enhanced carrier escape in MSQW solar cell and its impact on photovoltaics performance," IEEE Journal of Photovoltaics, vol. 2, no. 2, pp.221-226, 2012.

[17] K. Matsushima, R. Shimizu, T. Ide, D. Yamashita, H. Seo, K. Koga, M. Shiratani, and N. Itagaki, "Fabrication of ZnInON/ZnO multi-quantum well solar cells," Thin Solid Films, vol. 587, pp.106-111, 2015.

[18] G. Siddharth, R. Singh, V. Garg, B. S. Sengar, M. Das, B. Mandal, M. T. Htay, M. Gupta, and S. Mukherjee, "Investigation of DIBS-Deposited CdZnO/ZnO-Based Multiple Quantum Well for Large-Area Photovoltaic Application," IEEE Transactions on Electron Devices, vol. 67, no. 12, pp.5587-5592, 2020.

[19] D. J. Friedman, "Progress and challenges for next-generation high-efficiency multijunction solar cells," Current Opinion in Solid State and Materials Science, vol. 14, no. 6, pp.131-138, 2010.

[20] N. G. Young, E. E. Perl, R. M. Farrell, M. Iza, S. Keller, J. E. Bowers, S. Nakamura, S. P. DenBaars, and J. S. Speck, "High-performance broadband optical coatings on InGaN/GaN solar cells for multijunction device integration," Applied Physics Letters, vol. 104, no. 16, p.163902, 2014.

[21] N. J. Ekins-Daukes, J. M. Barnes, K. W. J. Barnham, J. P. Connolly, M. Mazzer, J. C. Clark, R. Grey, G. Hill, M. A. Pate, and J. S. Roberts, "Strained and strain-balanced quantum well devices for high-efficiency tandem solar cells," Solar Energy Materials and Solar Cells, vol. 68, no. 1, pp.71-87, 2001.

[22] B. Kim, K. Toprasertpong, A. Paszuk, O. Supplie, Y. Nakano, T. Hannappel, and M. Sugiyama, "GaAsP/Si tandem solar cells: Realistic prediction of efficiency gain by applying strain-balanced multiple quantum wells," Solar Energy Materials and Solar Cells, vol. 180 pp. 303-310, 2018.

[23] G. K. Bradshaw, J. P. Samberg, C. Z. Carlin, P. C. Colter, K. M. Edmondson, W. Hong, C. Fetzer, N. Karam, and S. M. Bedair, "GaInP/GaAs tandem solar cells with InGaAs/GaAsP multiple quantum wells," IEEE Journal of Photovoltaics, vol. 4, no. 2, pp.614-619, 2014.

[24] K. Y. Lai, G. J. Lin, C. Y. Chen, Y. L. Lai, and J. H. He, "Origin of hot carriers in InGaN-based quantum-well solar cells," IEEE Electron Device Letters, vol. 32, no. 2, pp.179-181, 2010.

[25] W. Yanwachirakul, H. Fujii, K. Toprasertpong, K. Watanabe, M. Sugiyama, and Y. Nakano, "Effect of Barrier Thickness on Carrier Transport Inside Multiple Quantum Well Solar Cells Under High-Concentration Illumination," IEEE Journal of Photovoltaics, vol. 5, no. 3, pp.846-853, 2015.

Chapter 2

Fundamentals of multiple quantum well solar cell

2.1. Introduction

The multiple quantum well solar cells (MQWSC) are first proposed by Barnham and Duggan in 1990 [1] involving multiple energy bandgap semiconductors and a rigorous research has been performed in this efficiency enhancement technique in the past decade. The MQWSC is just the extension of *p*-*i*-*n* structure, where quantum wells are incorporated in the intrinsic region of the solar cell, to enhance conversion efficiency of the solar cell [1]. The principle of MQWSC is reasonably analogous to that of the tandem cell i.e. comprising several energy bandgaps semiconductors to absorb different part of the spectrum efficiently. However, instead of using two or more *p*-*n* junctions prepared from different energy bandgap semiconductors, the MQWSC consists of ultra-thin layers of different energy bandgap semiconductors involving single *p*-*n* junction.

For *p*-*i*-*n* solar cells, it is reasonably challenging to achieve thick intrinsic layers, because the thicker layer leads to an increase in recombination of charge carrier before being collected at the electrodes. In MQWSC, a well material with small energy bandgap leads to current increment compared to the conventional solar cell as additional charge-carriers are generated due to increased absorption of the solar spectrum. This results, in an increase in J_{sc}. However, V_{oc} remains relatively unaffected as it is controlled largely by high energy bandgap of the barrier material. Thus, this leads to an overall increase in the conversion efficiency of the solar cell. MQWSCs also find applications in the MJSCs for the effective current matching of all the sub cells, i.e. top, middle and bottom cells [2].

In concentrators and conventional solar cells, the prime concern is the performance degradation with the increase in device temperature. Since in MQWSC, transport mechanism of charge carrier from quantum wells is mainly thermally activated, thus these are estimated to show a better conversion efficiency at high temperature than the conventional cells and therefore, this makes them more feasible for concentrated solar cell applications [3, 4].

However, the thickness of the quantum well layer has to be optimized in MQWSC for better performance. The thinner quantum wells permit additional wells to be inserted for a fixed total thickness of the intrinsic material, thus an increase in the number of quantum wells offers additional material for the low-energy photon to get absorbed. But, this also increases the interfaces for recombination of charge-carriers in MQWSCs. While, the wider quantum wells have less probability for the charge-carriers to be able to escape, therefore, increases the possibility of recombination in the quantum well itself [5].

The conventional bulk cells have maximized conversion efficiency of 27.5% obtained at a single optimum energy bandgap of intrinsic material, $E_{Bu} = 1.4\ eV$, whereas the optimum conversion efficiency of MQWSC is 30.2% obtained at the quantum well layer energy bandgap of $E_W = 1.33\ eV$ [6].

2.2. Physics of QWs

Quantum wells have different electronic structure as compared to other heterostructure of semiconductors, because of the confinement of charge carriers in one dimension of thin semiconductor layers. This distinctive electronic structure affects the physical processes of incident photon absorption, charge carrier transport and their relaxation, which plays important part in photovoltaic energy conversion process [7]. The typical quantum well structure with its corresponding energy band diagram is shown in Figure 2.1.

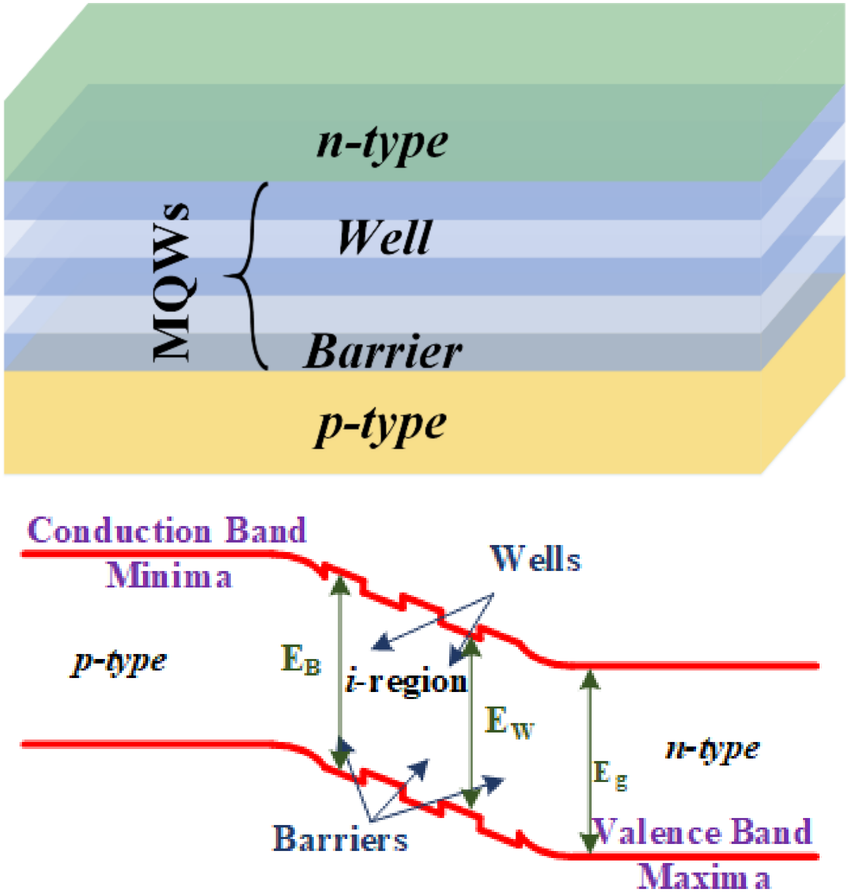

Figure 2.1 *MQWSC schematic with its corresponding energy band diagram [8].*

A QW is developed when narrow energy bandgap semiconductor layer i.e. well layer of a few nanometres thick is sandwiched between two wide energy bandgap semiconductor layers i.e. barrier layers. If minima of conduction band is lower and maxima of valence band is higher with respect to energy in the well layer than in the barrier layer, then both the charge carriers i.e. electrons and holes are in the well layer. The structure involving similar type of QWs is shown in Figure 2.1 and this type of QW is known as a Type I QW. If only one of the charge carrier type is confined in the well layer, then it is known as Type II QW [7].

De Broglie have proposed that electron and other particles of the matter can have wave like properties. The energy and momentum of the particle would be associated to the frequencies and wave vectors of these "matter waves" by the de Broglie relations [9]:

$$E = \hbar\omega \tag{2.1}$$

$$p = \hbar k \tag{2.2}$$

where $\hbar = h/2\pi$ is Planck's constant.

The time-independent Schrödinger equation describes the wave function ψ of electrons as [9, 10]:

$$-\frac{\hbar^2}{2m^*}\nabla^2\psi = E\psi \tag{2.3}$$

The wavefunction for QW can be attained by solving the generalized one dimensional Schrödinger equation for each band with the one-dimensional potential *V(z)* and position-dependent effective mass m^*(z) [7, 11].

$$-\frac{\hbar^2}{2}\frac{\partial}{\partial z}\left[\frac{1}{m^*(z)}\frac{\partial\psi(z)}{\partial z}\right] + V(z)\psi(z) = E\psi(z) \tag{2.4}$$

The QW forms a quasi-two-dimensional system. As the potential energy of the well layer is lower compared to that of barrier layer, it leads to a confinement in the electron wave function, which can be obtained by solving the equation (2.4). Confinement of charge carriers i.e. electrons and holes in the deposition/growth (say, z) direction (thickness of the layer) leads to the quantization of z component of their kinetic energy and momentum. The quantized energy (E_n) of the nth level corresponding to the z component of the wave vector (k_n) is given by [7]

$$E_n = \frac{\hbar^2 k_n^2}{2m^*} \tag{2.5}$$

The first three quantized energy states in the conduction band structure are shown in Figure 2.2. The charge carriers are confined to a set of sub-bands of minimum energy V_n, but they are free to move in the (xy) plane of the well layer. Therefore, the total energy of a charge carrier in the nth sub-band within (xy) plane movement is equal to [7]

$$E(k) = E_n + \frac{\hbar^2 k_{xy}^2}{2m_{xy}^*} \tag{2.6}$$

where k is the total wave vector, k_{xy} is the component in the xy plane (such that $k^2 = k_n{}^2 + k_{xy}{}^2$), and $m_{xy}*$ is the effective mass of the carrier in this plane.

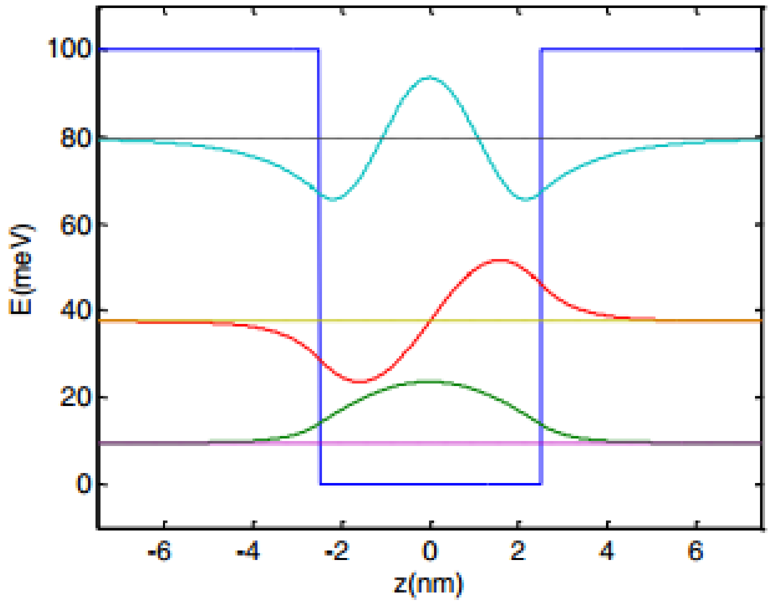

Figure 2.2 *Conduction band structure of a 5 nm thick QW with a barrier height of 100 meV showing first three quantized energy states [12].*

In quantum well systems, there are only two degrees of freedom, as there is one-dimensional confinement and thus it leads to an energy-independent density of states (number of electron states per energy per unit area per quantum well layer) for each confined subband [13].

$$\rho^{2D}(E) = \frac{1}{2\pi}\frac{2m^*}{\hbar^2}E^0 \tag{2.7}$$

The advantage of using such a confined system is that we can modify the optical characteristics of the material, such as the optical absorption edge.

2.3. Development in MQWSC

The rigorous study both via theoretical and experimental approaches has been performed worldwide in the MQWSC. Theoretically, numerous models have been developed to analyze the performance of MQWSC [5, 6, 14]. Ramey and Khoie [5] have studied MQWSC by developing a model involving the escape, capture and recombination of the photoexcited charge carriers in quantum wells, and arrives at the conclusion that incorporating MQWs in the intrinsic region of *p-i-n* structure solar cell leads to an improvement in the conversion efficiency. Aperathitis *et al.* [14] have examined the performance of AlGaAs/GaAs-based MQWSC by studying the effect of tunneling current on the generated photocurrent at various temperatures. Anderson [6] has proposed an ideal model to study MQWSC, based on the effect of charge carrier generation and recombination in the QWs.

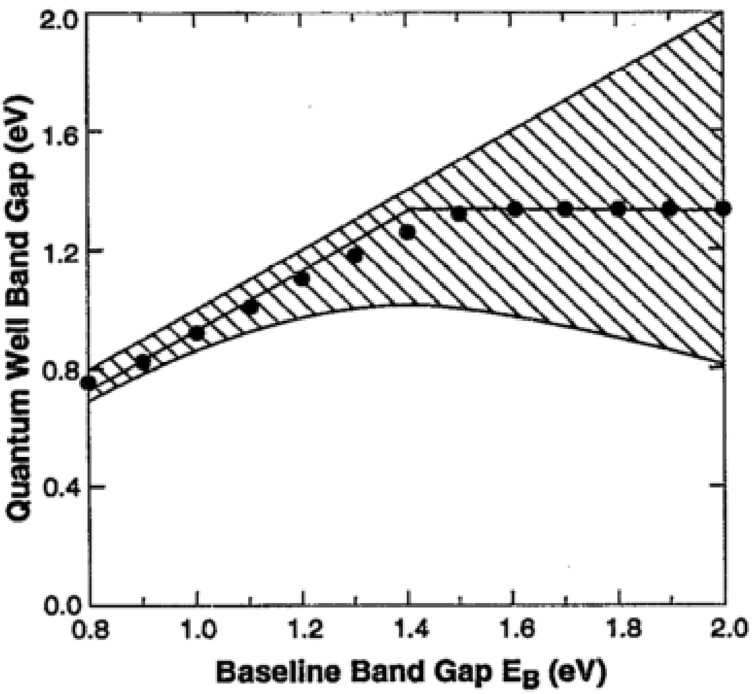

Figure 2.3 *Possible combination of quantum well bandgap (E_W) and barrier bandgap (E_B) [6].*

The energy bandgap (E_W) of quantum well layer has to be selected corresponding to a particular barrier layer energy bandgap (E_B), so that enhancements in the conversion efficiency can be possible and the same mechanism is shown in Figure 2.3 for the selection of quantum well materials as per the barrier material or vice-versa. However, the optimum values for the selection of the same are denoted by the solid circular points. The upper bound of the shaded region is governed by the line $E_W = E_B$, at which quantum well disappears, while the lower bound is defined at which quantum well recombination reduces efficiency enhancements. Note that for smaller E_B, the optimum value of E_W

increases with the increase in E_B, but for larger E_B, E_W saturates and takes on an optimum value 1.33 eV [6].

The number of QWs that can be inserted in MQWSC is basically limited by lattice mismatch between well and barrier layers. Therefore, strain balance approach is used for enhancing the conversion efficiency, for example, if well produces compressive strain, then barrier with tensile strain is used to balance the strain, thus overcoming the lattice mismatch limitation and shown in Figure 2.4 [15].

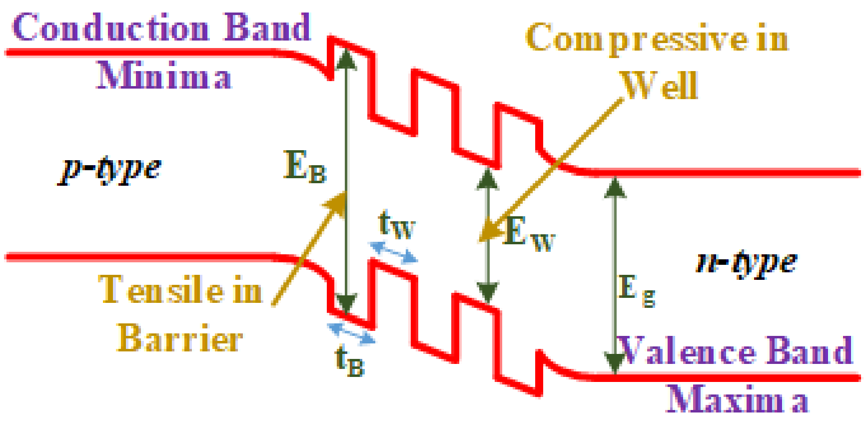

Figure 2.4 *Energy band diagram of strain balanced MQWSC.*

The basic dimensions relation to ensure the average lattice parameter (a) across the intrinsic region is define as follows [16]:

$$a = \frac{t_B a_B + t_W a_W}{t_B + t_W} \tag{2.8}$$

where t_B and t_W are the thickness of barrier and well region, and a_B and a_W are the lattice parameter of barrier and well region, respectively.

2.4. State of the art research

There are several experimental studies to investigate the qualitative performance of MQWSC. Various deposition techniques are employed by the research community working in this technology. Mostly, the research in this field is on GaN and GaAs based materials, as their energy bandgap can be changed by alloying them with indium, phosphorous and aluminium, so that most of the solar spectrum can be covered more efficiently. Table 2.1 shows some of the research done in this field by using different materials and deposition techniques.

Table 2.1: *Experimental study of MQWSC having different QW pair and deposition techniques*

MQWs	QW pair	Deposition technique	V_{oc} (V)	J_{sc} (mA/cm^2)	FF (%)	PCE (%) [Ref]
12	$In_{.35}Ga_{.65}N$ (3 nm)/GaN (16 nm)	MOCVD	1.8	2.56	64	3.03 [17]
14	$In_{.21}Ga_{.79}N$ (3 nm)/$Al_{.14}Ga_{.86}N$ (4 nm)	MOVPE	2.1	0.84	66	1.16 [18]
7	$In_{.15}Ga_{.85}N$ (3 nm)/GaN (8 nm)	MOCVD	2.2	1.25	80	2.3 [19]
20	$In_{.19}Ga_{.81}N$ (2.3 nm)/GaN (12.7 nm)	Rapid Thermal Chemical Vapour Deposition (RTCVD)	2.92	2.72	74.8	5.95 [20]
20	$In_{.19}Ga_{.81}N$ (3 nm)/GaN (13 nm)	RTCVD	2.94	2.71	75	5.99 [21]
30	$In_{.2}Ga_{.8}N$ (3 nm)/GaN (4 nm)	MOCVD	2.26	2.97	67.9	3.33 [2]
10	$In_{.18}Ga_{.82}As$ (8.5 nm)/$GaAs_{.78}P_{.22}$ (12.5 nm)	MOVPE	0.87	16.2	74	10.5 [22]

20	$In_{.16}Ga_{.84}As$ (7.6 nm)/ $GaAs_{.79}P_{.21}$ (11.6 nm)	MOVPE	0.88	22.25	80	14.2 [23]

Till date, there are only two experimental reports on the fabrication of ZnO-based MQWs for solar cell by sputtering process.

The MQWSC structure fabricated by Matsushima *et al.* [24] is composed of *n*-type Al:ZnO (AZO), 7 pairs of ZnInON (6 nm) / ZnO (15 nm) MQWs, and *p*-type GaN or Si substrate. The deposition of ZnInON well, ZnO barrier and *n*-type AZO layers is performed by RF magnetron sputtering in Ar-O_2-N_2, Ar-O_2 and pure Ar ambient, respectively. The V_{oc} and J_{sc} parameters of MQWSC realized on *p*-Si substrate are 0.23 V and 7.1×10^{-4} A/cm^2, respectively, and the parameters on *p*-GaN substrate are 0.16 V and 1.9×10^{-6} A/cm^2, respectively. Comparatively, small total thickness of MQWs and the wide bandgap of the well layers accounts for the low current density in both cases. Comparatively, high current density in case of Si owes to its smaller bandgap of 1.2 eV as compared to that of GaN (3.4 eV) at room temperature. However, low V_{oc} on *p*-GaN may be due to the large number of dislocations (10^9 cm^{-2}), leading to an increase in carrier recombination.

Our group have investigated the DIBS deposited CdZnO/ZnO-based MQW for solar cell application and is part of this thesis and discussed in details in the later chapters [25].

2.5. Conclusion

In this chapter, it is seen that, MQWSC is just the extension of the *p-i-n* solar cell structure. The basic principle behind the QW as described by Schrodinger equations are discussed briefly and it is analysed that confinement of the charge carrier occurs in one dimension of thin semiconductor layers. This feature affects the absorption of incident photons and charge carrier transport mechanism in the thin semiconductor layers. The confinement of the charge carrier in one dimension leads to the quantization of the kinetic energy in the same dimension. As the number of QWs that can be inserted in MQWSC is basically limited by lattice mismatch between well and barrier layers, therefore, strain balance approach used for enhancing the conversion efficiency is discussed.

Further, the research and development in the field of MQWSC using different material system both theoretically and experimentally are discussed. The analytical model developed for the *p-i-n* structure is discussed in the next chapter followed by the analytical model development for MQWSC discussed in the later chapter.

2.6. References

[1] K.W.J. Barnham, and G. Duggan, "A new approach to high-efficiency multi-band-gap solar cells," Journal of Applied Physics, vol. 67, no. 7, pp.3490-3493, 1990.

[2] N. G. Young, E. E. Perl, R. M. Farrell, M. Iza, S. Keller, J. E. Bowers, S. Nakamura, S. P. DenBaars, and J. S. Speck, "High-performance broadband optical coatings on InGaN/GaN solar cells for multijunction device integration," Applied Physics Letters, vol. 104, no. 16, p.163902, 2014.

[3] K. Y. Lai, G. J. Lin, C. Y. Chen, Y. L. Lai, and J. H. He, "Origin of hot carriers in InGaN-based quantum-well solar cells," IEEE Electron Device Letters, vol. 32, no. 2, pp.179-181, 2010.

[4] W. Yanwachirakul, H. Fujii, K. Toprasertpong, K. Watanabe, M. Sugiyama, and Y. Nakano, "Effect of Barrier Thickness on Carrier Transport Inside Multiple Quantum Well Solar Cells Under High-Concentration Illumination," IEEE Journal of Photovoltaics, vol. 5, no. 3, pp.846-853, 2015.

[5] S. M. Ramey, and R. Khoie, "Modeling of multiple-quantum-well solar cells including capture, escape, and recombination of photoexcited carriers in quantum wells," IEEE Transactions on Electron Devices, vol. 50, no. 5, pp.1179-1188, 2003.

[6] N. G. Anderson, "Ideal theory of quantum well solar cells," Journal

of Applied Physics, vol. 78, no. 3, pp.1850-1861, 1995.

[7] M. D. Archer, and M. A. Green, “Clean electricity from photovoltaics,” World Scientific, vol. 4, 2014.

[8] G. Siddharth, V. Garg, B. S. Sengar, and S. Mukherjee, “Progress in Thin Film Solar Cell and Advanced Technologies for Performance Improvement,” Invited by Prof. Saleem Hashmi (editor-in-chief), Reference Module in Materials Science and Materials Engineering, (Accepted).

[9] P. Harrison, “Quantum wells, wires and dots,” Chichester, UK: Wiley, 2016.

[10] D. J. Griffiths, and D. F. Schroeter, “Introduction to quantum mechanics,” Cambridge University Press, 2018.

[11] D. A. Miller, “Optical physics of quantum wells. Quantum Dynamics of Simple Systems," ed. G.-L. Oppo, SM Barnett, E. Riis, and M. Wilkinson, pp.239-26, 1996.

[12] M. Ito, "Theoretical and experimental investigation of quantum well intermediate band solar cells." PhD diss., Imperial College London, 2014.

[13] G.A. Bastard, “Wave Mechanics Applied to Semiconductor Heterostructures,” Les Editions de Physique, Paris, ISBN 978-0470217085, 1988.

[14] E. Aperathitis, A. C. Varonides, C. G. Scott, D. Sand, V. Foukaraki, M. Androulidaki, Z. Hatzopoulos, and P. Panayotatos, “Temperature dependence of photocurrent components on enhanced performance GaAs/AlGaAs multiple quantum well solar cells,” Solar Energy Materials and Solar Cells, vol. 70, no. 1, pp.49-69, 2001.

[15] I. E. H. Sayed, C. Z. Carlin, B. G. Hagar, P. C. Colter, and S. M. Bedair, “Strain-balanced InGaAsP/GaInP multiple quantum well solar cells with a tunable bandgap (1.65–1.82 eV),” IEEE Journal of Photovoltaics, vol. 6, no. 4, pp.997-1003, 2016.

[16] B. Kim, K. Toprasertpong, A. Paszuk, O. Supplie, Y. Nakano, T.

Hannappel, and M. Sugiyama, “GaAsP/Si tandem solar cells: Realistic prediction of efficiency gain by applying strain-balanced multiple quantum wells,” Solar Energy Materials and Solar Cells, vol. 180, pp.303-310, 2018.

[17] R. Dahal, J. Li, K. Aryal, J. Y. Lin, and H. X. Jiang, “InGaN/GaN multiple quantum well concentrator solar cells,” Applied Physics Letters, vol. 97, no. 7, p.073115, 2010.

[18] C. C. Yang, J. K. Sheu, X. W. Liang, M. S. Huang, M. L. Lee, K. H. Chang, S. J. Tu, F. W. Huang, and W. C. Lai, “Enhancement of the conversion efficiency of GaN-based photovoltaic devices with AlGaN/InGaN absorption layers,” Applied Physics Letters, vol. 97, no. 2, p.021113, 2010.

[19] S. Y. Bae, J. P. Shim, D. S. Lee, S. R. Jeon, and G. Namkoong, “Improved photovoltaic effects of a vertical-type InGaN/GaN multiple quantum well solar cell,” Japanese Journal of Applied Physics, vol. 50, no. 9R, p.092301, 2011.

[20] B. W. Liou, “Design and fabrication of $In_xGa_{1-x}N$/GaN solar cells with a multiple-quantum-well structure on SiCN/Si (111) substrates,” Thin Solid Films, vol. 520, no. 3, pp.1084-1090, 2011.

[21] B. W. Liou, “Temperature of InxGa1− xN/GaN solar cells with a multiple-quantum-well structure on SiCN/Si (111) substrates,” Solar Energy Materials and Solar Cells, vol. 114, pp.141-146, 2013.

[22] B. Behaghel, R. Tamaki, N. Vandamme, K. Watanabe, C. Dupuis, N. Bardou, H. Sodabanlu, A. Cattoni, Y. Okada, M. Sugiyama, and S. Collin, “Absorption enhancement through Fabry-Pérot resonant modes in a 430 nm thick InGaAs/GaAsP multiple quantum wells solar cell,” Applied Physics Letters, vol. 106, no. 8, p.081107, 2015.

[23] Y. Wen, Y. Wang, K. Watanabe, M. Sugiyama, and Y. Nakano, “Enhanced carrier escape in MSQW solar cell and its impact on photovoltaics performance,” IEEE Journal of Photovoltaics, vol. 2, no. 2, pp.221-226, 2012.

[24] K. Matsushima, R. Shimizu, T. Ide, D. Yamashita, H. Seo, K. Koga, M. Shiratani, and N. Itagaki, “Fabrication of ZnInON/ZnO multi-quantum well solar cells,” Thin Solid Films, vol. 587, pp.106-111, 2015.

[25] G. Siddharth, R. Singh, V. Garg, B. S. Sengar, M. Das, B. Mandal, M. T. Htay, M. Gupta, and S. Mukherjee, “Investigation of DIBS-Deposited CdZnO/ZnO-Based Multiple Quantum Well for Large-Area Photovoltaic Application,” IEEE Transactions on Electron Devices, vol. 67, no. 12, pp.5587-5592, 2020.

Chapter 3

Analytical model for *p-i-n* solar cells

3.1. Introduction

Generally, a single *p-n* junction solar cells are developed and this technology has almost reached to its efficiency limit as predicted from Shockley and Queisser limit. Also, the production of a healthy depletion region depends on the doping concentration of the two semiconductor regions used to fabricate the *p-n* junction. As, low doping concentrations produce a wide depletion region, and heavy doping concentrations create a thin depletion layer, which are not helpful for PV conversion. Optimising the doping concentration to create a depletion region width comparable to the thickness of a thin film solar cell is a real challenge faced by the researchers [1]. Therefore, new approaches are developed and researched to further improve the conversion efficiency, one of which is the introduction of intrinsic region in between the *p* and *n* type semiconductor. In this structure, the built in potential is same as that of the *p-n* junction with the same doping levels, but the electric field extends to wider region. The lifetime of the carriers in the intrinsic region are usually extended relative to those in the doped regions. The overall depletion region is increased by the insertion of intrinsic region, and therefore extends the thickness over which the more number of photons can be absorbed and thus generates more number of electron-hole pairs. As, this region is feasible for the carrier generation and collection, thus it leads to the increase in short-circuit current density of the solar cell. However, the intrinsic region thickness does not have much impact on the open-circuit voltage, so the increase in conversion efficiency is basically governed by the short-circuit current density [2]. The charge carrier which are photo-generated in this intrinsic region are separated and driven towards the respective contacts by the electric field [3].

For this structure, the thickness of the intrinsic region should to be optimized for maximum current generation in the solar cell. Although, the light is more efficiently absorbed in thicker intrinsic region, but at some thickness value of intrinsic region, it exceeds the space charge width. The exceeded thickness is of no use and does not contribute to the photocurrent generation [2-6]. So, this defines the maximum limit of intrinsic region thickness in *p-i-n* structure, and therefore p-i-n solar cell should be designed by having depletion region width greater than the thickness of intrinsic region at operating bias.

A physics-based analytical model is presented to obtain device performance parameters of the *p-i-n* solar cells. The solar energy spectra for space and terrestrial application referred to as AM0, AM1.5G and AM1.5D are based on ASTM standards [7-9]. In the developed models, the device performance parameters such as short circuit current density, open circuit voltage, and energy conversion efficiency are studied for different indium composition (x = 0.1, 0.2 and 0.3) in $In_xGa_{1-x}N$ (intrinsic region) and at different temperatures. Despite the fact that higher indium composition leads to a much better spectral overlap, it is limited to 0.3 in this work, as the higher composition reduces the crystalline quality leading to a larger loss of photo-generated charge carriers [10]. In this work, the data sheets from the ASTM standard are used, to ascertain the photon flux density [11] instead of the black body radiation formula which differs from the actual solar energy spectra.

3.2. Analytical Model

3.2.1 Basic parametric equations

Some of the basic parametric equations that are utilized in the model developments to study the performance of the solar cell under different conditions such as different composition of intrinsic material and different operation temperature, are explained here.

The dependence of the energy band gap of the $In_xGa_{1-x}N$ alloy on the indium composition is obtained by using the Vegard's law and can written as [12]

$$E_g(In_xGa_{1-x}N) = xE_g(InN) + (1-x)E_g(GaN) - bx(1-x) \tag{3.1}$$

Here, b is the bowing parameter whose value for $In_xGa_{1-x}N$ is 1.43. The variation of the energy band gap with the temperature can be described by the expression given by Varshni [13]

$$E_g(T) = E_{g0} - \frac{\beta_1 T^2}{T+\beta_2} \tag{3.2}$$

where T is the absolute temperature, E_{g0} is the energy band gap at 0˚K and β_1 and β_2 are material dependent parameters.

The reverse saturation current density (J_s) is given by

$$J_s = qn_i^2\left(\frac{D_p}{L_pN_D} + \frac{D_n}{L_nN_A}\right) \tag{3.3}$$

where D_p and D_n are the diffusion constants for holes and electrons respectively and given by Einstein relation, L_p and L_n are the diffusion length for holes and electrons respectively and given by $L = \sqrt{D\tau}$, where τ is the minority carrier lifetime and N_A and N_D are the acceptor and donor concentrations.

The general absorption coefficient valid for all dimensional (D) materials for free carriers is given by [14]

$$\alpha(\omega) = \alpha_0^D \frac{\hbar\omega}{E_1}\left(\frac{\hbar\omega - E_g - E_0^D}{E_1}\right)^{\frac{D-2}{2}} \Theta\big(\hbar\omega - E_g - E_0^D\big)A(\omega) \tag{3.4}$$

where $\Theta(x)$ is the Heavyside function, $A(\omega)$ is the band-filling factor, $E_0^D = \{\hbar^2\pi^2(3-D)\}/\{2m_rL_c^2\}$ is the zero point energy, and the scaling parameters, $E_1 = \hbar^2/(2m_ra^2)$ and $a = \hbar^2\varepsilon_0/(q^2m_r)$. Most of the photon absorption occurs over the penetration depth, $\delta = 1/\alpha$. The thickness of the absorption material depends on the penetration depth and the diffusion coefficient of hole and electron by the following relation: diffusion lengths (L_p and L_n)> absorber thickness > penetration depth (δ) [15].

The spectral photon flux ($N_{ph}(\lambda)$) and irradiance (I) are calculated from spectral power density ($P(\lambda)$) by using the following expression [11, 16]

$$N_{ph}(\lambda) = P(\lambda)\frac{\lambda}{hc} = 5.034 \times 10^{14} P(\lambda)\lambda \tag{3.5}$$

$$I = \int P(\lambda)\, d\lambda \tag{3.6}$$

where h is the Planck's constant and c is the speed of light. The photon flux density is useful for calculating the theoretical number of photons that can be collected as a function of photovoltaic material band gaps [11, 17].

The $P(\lambda)$ for AM1.5 is available from ASTM standard data sheets [7] as a function of wavelength. These equations are further used for the assessment of current density vs voltage (*J-V*), power density vs voltage (*P-V*) characteristics and device performance parameters.

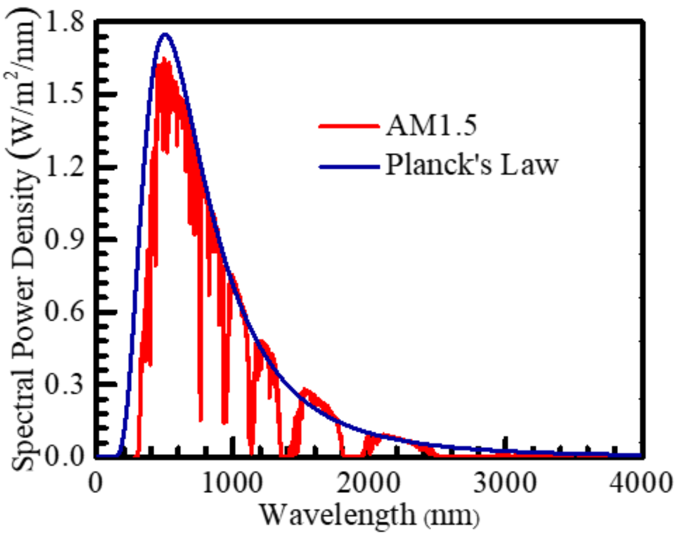

Figure 3.1 *Spectral power density from ASTM data sheets for AM1.5 and Planck's Law.*

The spectral power density calculated from Planck's Law is given by the following expression [18]:

$$P(\lambda, T) = \frac{2hc^2}{\lambda^5}\frac{1}{exp\left(\frac{hc}{\lambda k_B T}\right) - 1}\pi\left(\frac{R_s}{Au - R_e}\right)^2 \tag{8.7}$$

where R_s and R_e are the radii of the Sun and Earth, respectively, Au is the distance between the Sun and Earth, and T is the Sun temperature.

The spectral power density from the ASTM data sheets for AM1.5 and Planck's Law is shown in Figure 3.1, and it can be concluded that more accurate SC performance can be obtained with AM1.5 as compared to the results achieved by using Planck's law [19], as Planck's Law gives only approximate spectral power density. Therefore, in this study the ASTM data sheets for AM1.5 are utilized to obtain the photon flux instead of Plank's Law.

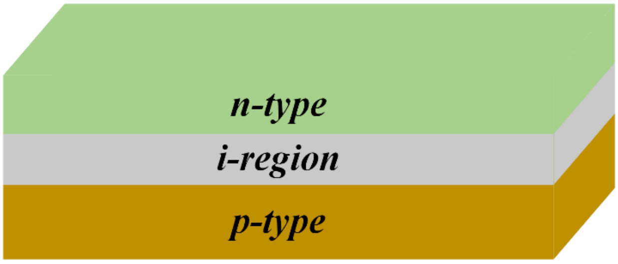

Figure 3.2 *The schematic of the p-i-n structure.*

3.2.2 *J-V* characteristics and performance parameters of *p-i-n* solar cell

The schematic of the *p-i-n* structure is shown in the Figure 3.2. The illuminated current density vs voltage (*J-V)* characteristics of the *p-i-n* solar cell is described by the Shockley solar cell equation [20, 21]:

$$J_{Bu}(V) = J_s[\exp(V/V_t) - 1] - J_{Ge} + J_{Re} \tag{3.8}$$

where V is the terminal voltage, V_t is the thermal voltage, J_s is the reverse saturation current density (the term including J_s represents the ideal recombination current from the diffusion and recombination of electrons and holes), J_{Ge} and J_{Re} are the superimposed current densities corresponding to carrier generation (because of illumination by solar spectra) and recombination in the intrinsic region respectively. For *p-i-n* solar cell, the generation and recombination current density terms can be written as in equations (3.9) and (3.10) [20, 21]:

$$J_{Ge} = qt_i[G_{BuO} + G_{BuT}] \tag{3.9}$$

$$J_{Re} = qt_iR_{Bu} = qt_iB_{Bu}n_{iBu}^2 \exp(V/V_t) \tag{9.10}$$

where t_i is the intrinsic region thickness and G_{BuO} and G_{BuT} are the optical and thermal generation rate respectively, throughout the intrinsic region, R_{Bu} is the average recombination rate in the intrinsic region,

B_{Bu} is the barrier recombination coefficient, n_{iBu} is the equilibrium intrinsic carrier concentration. Since, $G_{BuT} = B_{Bu} n_{iBu}^2$, and by substituting the equation of J_{Ge} and J_{Re} in equation (3.8), *J-V* characteristics of the *p-i-n* solar cell is

$$J_{Bu}(V) = J_s(1 + \beta_3)[\exp(V/V_t) - 1] - qt_i G_{BuO} \qquad (3.11)$$

where the factor β_3 describe the contribution of the current required to feed radiative recombination in the intrinsic region at equilibrium and is given as

$$\beta_3 = \frac{qt_i B_{Bu} n_{iBu}^2}{J_s} \qquad (3.12)$$

The short circuit current density can be obtained by substituting $V = 0$ in equation (3.11), if the optical generation rate in intrinsic region is known, however, in this model it is obtained using the spectral photon flux instead of Plank' Law and is given as

$$J_{scBu} = -qt_i G_{BuO} = -q[f_2 N_{ph}(E > E_{Bu}) + N_{ph}(E = E_{Bu})] \qquad (3.13)$$

The term $N_{ph}(E > E_{Bu})$ is the net photon flux density corresponding to the energies greater than E_{Bu} and $N_{ph}(E = E_{Bu})$ is the net photon flux density corresponding to the energy E_{Bu} and f_2 is the fraction of the light absorbed whose energies are above the energy band gap [22]. The open circuit voltage is obtained by evaluating the $J_{Bu}(V) = 0$ in equation (3.11) and by utilizing J_{scBu} obtained from equation (3.13) and is given by

$$V_{ocBu} = V_t \ln\left[\frac{J_s(1 + \beta_3) - J_{scBu}}{J_s(1 + \beta_3)}\right] \qquad (3.14)$$

The device performance parameter, which describes the quality of the *J–V* curve, is the fill factor (FF) and is defined as [17, 22]

$$FF = \frac{V_{mBu} J_{mBu}}{V_{ocBu} J_{scBu}} \qquad (3.15)$$

Here, V_{mBu} and J_{mBu} are the voltage and current density respectively, corresponding to the maximum power density point on the *J-V* characteristic of the solar cell, at which it has the maximal power density. The operating regime of the solar cell in which the it delivers the power is in the range from 0 to V_{oc}. The power density of the solar cell is given by $P = JV$ [17]. The voltage V_{mBu} is obtained by the derivation of power density P with respect to voltage V and then equating $\frac{\partial P}{\partial V} = 0$ [23-25]. The final equation which is used to obtained V_{mBu} by the iteration method is

$$exp\left(\frac{V_{ocBu}}{V_t}\right) - exp\left(\frac{V_{mBu}}{V_t}\right)\left[1 + \frac{V_{mBu}}{V_t}\right] = 0 \tag{3.16}$$

Similarly, the value of J_{mBu} is obtained by the derivation of power density P with respect to voltage J and then equating $\frac{\partial P}{\partial J} = 0$. So, the final iterative equation which is used to obtain J_{mBu} is

$$\frac{J_{mBu}}{J_{mBu} - J_{scBu} + J_s(1 + \beta_3)} + ln\left[\frac{J_{mBu} - J_{scBu} + J_s(1 + \beta_3)}{J_s(1 + \beta_3)}\right] = 0 \tag{3.17}$$

Finally, the energy conversion efficiency (η) of the solar cell is obtained by using J_{scBu}, V_{ocBu} and FF from equations (3.13, 3.14 and 3.15) and is given by [17]

$$\eta = \frac{V_{oc}J_{sc}FF}{P_{in}} \times 100\% \tag{3.18}$$

where $P_{in} = 100\ mW/cm^2$ as is described by the AM1.5 spectrum, is the irradiance of incident light.

3.3. Results and Discussion

Based on the analytical expressions derived above, the performance of InGaN/GaN-based *p*-*i*-*n* solar cells has been evaluated, where InGaN (150 nm) material is used as the intrinsic region with doping concentration of 2×10^{17} and 2×10^{18} cm^{-3} and thickness of 500 nm and 100 nm are used for the *p*- and *n*-GaN respectively. The *J*-*V* characteristics and device performance parameters of the InGaN/GaN-based *p*-*i*-*n* solar cell and their variation with different indium composition (x) of $In_xGa_{1-x}N$ in the intrinsic region and with various temperature of operation are illustrated in this section.

Figure 3.3 demonstrate the dark and illuminated *J-V* characteristics of the *p-i-n* solar cell with different indium composition (x) of $In_xGa_{1-x}N$ in the intrinsic region. Higher value of x in $In_xGa_{1-x}N$ alloy reduces the energy band gap of the intrinsic layer, because of which, J_{scBu} increases as a result of the increase in the carrier generation, however V_{ocBu} decreases as a result of the increase in carrier recombination [26-28]. Table 3.1 lists the performance parameters of the *p-i-n* solar cell for different x. As can be observed from Table 3.1, the increase in J_{scBu} with increasing x is larger as compared to the reduction in V_{ocBu}, consequently leading to the overall rise in the value of η. η increases by ~37 and ~56 % for x = 0.2 and 0.3, respectively, as compared to that for x = 0.1. Therefore, the increase in the x in the intrinsic region of the *p-i-n* solar cell enhances the solar cell conversion efficiency.

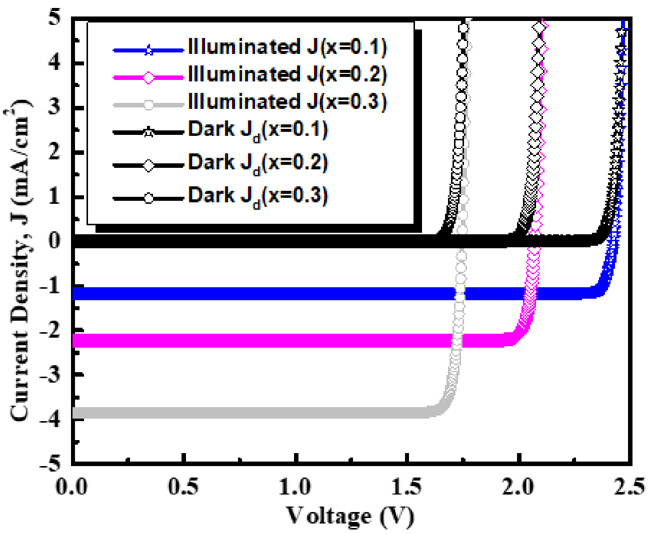

Figure 3.3 *J-V characteristics for p-i-n solar cell with different indium composition (x) of $In_xGa_{1-x}N$ in the intrinsic region.*

Table 3.1: *Performance parameters of p-i-n solar cell with different indium composition of $In_xGa_{1-x}N$*

Parameters	*x* = 0.1	*x* = 0.2	*x* = 0.3
J_{sc} (mA/cm^2)	1.18	2.22	3.84
V_{oc} (V)	2.42	2.07	1.75
η (%)	2.69	4.28	6.18

As the temperature of operation has a significant impact on solar cell performance, its effects on *p-i-n* solar cell performance parameters have been studied and are depicted in Figure 3.4. With the rise in temperature, the energy band gap decreases as depicted by equation (3.2), and because of that extra lower energy photons will be absorbed, which results in the increment of J_{scBu}. As expressed in equation (3.14), V_{ocBu} is determined by both J_{scBu} and J_s, however, the influence of the increase in J_s is more as compared to the increase in J_{scBu} with the increasing temperature, leading to the overall decrement of V_{ocBu} [29] and it follows approximately the linear curve [17]. As the temperature increases from 200 to 400 K, the larger reduction of V_{ocBu} (~28 %) as compared to the minor enhancement in the value of J_{scBu} (~13 %) eventually leads to the reduction in the value of η (~13 %) [17, 30], indicating that η has negative temperature coefficient. Therefore, it is concluded that, the rise in temperature leads to the reduction of the conversion efficiency.

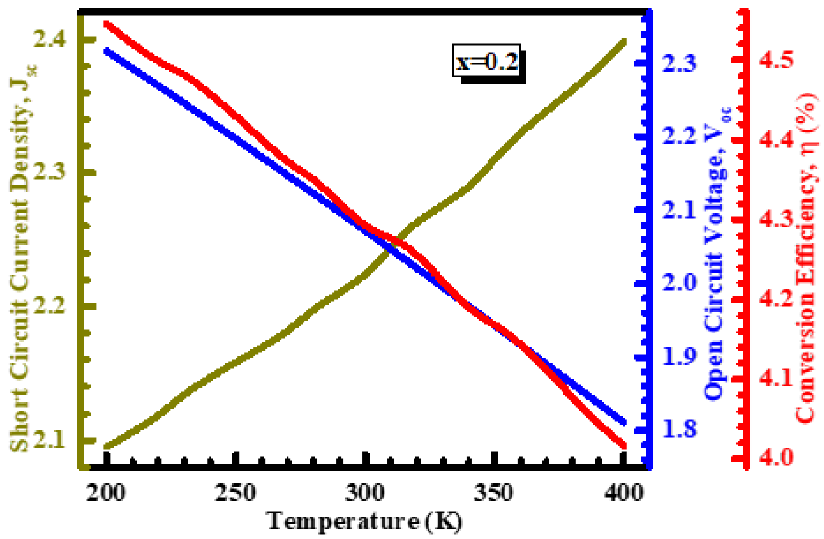

Figure 3.4 *The temperature-dependent short circuit current density, open circuit voltage and conversion efficiency of p-i-n solar cell.*

3.4. Conclusion

A physics-based generic analytical model for the *p-i-n* structure is developed for the calculation of device performance parameters and obtaining *J-V* characteristics of the solar cell. Significantly, in the developed model, the spectral power density available from the ASTM standard data sheets is utilized for attaining photon flux density instead of Plank's Law used in other published literatures, which minimizes the dissimilarities included in the performance parameters by using Plank's Law. Further, this obtained photon flux density is used for the modelling of performance parameters of the *p-i-n* solar cell. After, successfully developing the analytical model for *p-i-n* solar cell, the device performance parameters are studied for different indium composition in $In_xGa_{1-x}N$ (intrinsic region) of the InGaN/GaN-based *p-i-n* solar cell. The results shows that the conversion efficiency increases from 2.69 to 6.18 % as the indium composition in $In_xGa_{1-x}N$ increases from 0.1 to 0.3. The temperature-dependent study of the device performance parameters has shown that, with the increase in operation temperature from 200 to 400 K leads to the decrease in conversion efficiency of *p-i-n* solar cell from 4.54 to 4.01 %.

3.5. References

[1] I. M. Dharmadasa, "Advances in thin-film solar cells," CRC Press, 2018.

[2] S. W. Feng, C. M. Lai, C. H. Chen, W. C. Sun, and L. W. Tu, "Theoretical simulations of the effects of the indium content, thickness, and defect density of the i-layer on the performance of p-i-n InGaN single homojunction solar cells," Journal of Applied Physics, vol. 108, no. 9, p.093118, 2010.

[3] J. A. Nelson, "The physics of solar cells," World Scientific Publishing Company, 2003.

[4] S. Halilov, A. A. Baloch, N. Tabet, S. N. Rashkeev, and F. H. Alharbi, "Effect of Affinity Discontinuity on Heterojunction pin Solar Cell Performance," IEEE Journal of Photovoltaics, vol. 10, no. 2, pp. 458-466, 2020.

[5] H. Movla, D. Salami, and S. V. Sadreddini, "Simulation analysis of the effects of defect density on the performance of pin InGaN solar cell," Applied Physics A, vol. 109, no. 2, pp.497-502, 2012.

[6] J. Y. Chang, and Y. K. Kuo, "Numerical study on the influence of

piezoelectric polarization on the performance of p-on-n (0001)-face GaN/InGaN pin solar cells," IEEE Electron Device Letters, vol. 32, no. 7, pp.937-939, 2011.

[7] "ASTM G173-03 Reference Spectra Derived from SMARTS v. 2.9.2," [Online]. Available: https://www.nrel.gov/grid/solar-resource/spectra.html.

[8] C. A. Gueymard, D. Myers, and K. Emery, "Proposed reference irradiance spectra for solar energy systems testing," Solar Energy, vol. 73, no. 6, pp. 443-467, 2002.

[9] M. Anani, C. Mathieu, M. Khadraoui, Z. Chama, S. Lebid, and Y. Amar, "High-grade efficiency III-nitrides semiconductor solar cell," Microelectronics Journal, vol. 40, no. 3, pp. 427-434, 2009.

[10] B. W. Liou, "Design and fabrication of InxGa1−xN/GaN solar cells with a multiple-quantum-well structure on SiCN/Si(111) substrates," Thin Solid Films, vol. 520, no. 3, pp. 1084-1090, 2011.

[11] R. Hulstrom, R. Bird, and C. Riordan, "Spectral solar irradiance data sets for selected terrestrial conditions," Solar Cells, vol. 15, no. 4, pp. 365-391, 1985.

[12] J. Wu, W. Walukiewicz, K. M. Yu, J. W. Ager, E. E. Haller, H. Lu and W. J. Schaff, "Small band gap bowing in In1−xGaxN alloys," Applied Physics Letter, vol. 80, no. 25, pp. 4741-4743, 2002.

[13] Y. P. Varshni, "Temperature dependence of the energy gap in semiconductors," Physica, vol. 34, no. 1, pp. 149-154, 1967.

[14] H. Haug and S. W. Koch, Quantum Theory of the Optical and Electronic Properties of Semiconductors. World Scientific Publishing Company, p. 83, 2009.

[15] P. Wurfel and U. Wurfel, "Physics of solar cells: from basic principles to advanced concepts," Wiley-VCH, p. 182, 2016.

[16] K. Xu, "Monolithically integrated Si gate-controlled light-emitting device: Science and properties," Journal of Optics, vol. 20, no. 2, p. 024014, 2018.

[17] M. A. Green, Solar cells: Operating principles, technology, and system applications. Englewood Cliffs, NJ, Prentice-Hall, Incorporation, p. 80, 1982.

[18] A. H. Smets, K. Jäger, O. Isabella, R. A. Swaaij, and M. Zeman, “Solar Energy: The Physics and Engineering of Photovoltaic Conversion, Technologies and Systems,” Cambridge, U.K.: UIT Cambridge, 2015

[19] N. E. H. Gorji, H. Movla, F. Sohrabi, A. Hosseinpour, M. Rezaei, and H. Babaei, “The effects of recombination lifetime on efficiency and J-V characteristics of $In_xGa_{1-x}N$/GaN quantum dot intermediate band solar cell,” Physica E: Low-dimensional Systems and Nanostructures, vol. 42, no. 9, pp. 2353-2357, 2010.

[20] N. G. Anderson, “Ideal theory of quantum well solar cells,” Journal of Applied Physics, vol. 78, no. 3, pp. 1850-1861, 1995.

[21] J. C. Rimada and L. Hernández, “Modelling of ideal AlGaAs quantum well solar cells,” Microelectronics Journal, vol. 32, no. 9, pp. 719-723, 2001.

[22] T. Markvart and L. Castaner, “Solar Cells,” Elsevier, p. 34, 2005.

[23] S. R. Kurtz, P. Faine, and J. M. Olson, “Modeling of two-junction, series-connected tandem solar cells using top-cell thickness as an adjustable parameter,” Journal of Applied Physics, vol. 68, no. 4, pp. 1890-1895, 1990.

[24] H. Sun, K. Xu, J. Zhao, J. Zhang, Y. Zhou, L. Liu, J. Yuan, L. Huang, K. Zhu, L. W. Snyman, and K. A. Ogudo, “A dependency of emission efficiency of poly-silicon light-emitting device on avalanching current,” Optical Materials, vol. 88, pp. 711-717, 2019.

[25] H. Elghazi, A. Jorio, and I. Zorkani, “Analysis of temperature and 1 MeV proton irradiation effects on the light emission in bulk silicon (npn) emitter-base bipolar junctions,” Optics Communications, vol. 280, no. 2, pp. 278-284, 2007.

[26] S. M. Ramey and R. Khoie, “Modeling of multiple-quantum-well solar cells including capture, escape, and recombination of

photoexcited carriers in quantum wells,” IEEE Transactions on Electron Devices, vol. 50, no. 5, pp. 1179-1188, 2003.

[27] V. Garg, B. S. Sengar, A. Kumar, G. Siddharth, S. Kumar, and S. Mukherjee, "Investigation of valence plasmon excitations in GMZO thin film and their suitability for plasmon-enhanced buffer-less solar cells," Solar Energy, vol. 178, pp: 114-124, 2019.

[28] J. Wong, J. L. Huang, B. Eggleston, M. A. Green, O. Kunz, R. Evans, M. Keevers, and R. J. Egan, "Lifetime limiting recombination pathway in thin-film polycrystalline silicon on glass solar cells," Journal of Applied Physics, vol. 107, no. 12, p. 123705, 2010.

[29] Z. Chen, X. Zheng, Z. Li, P. Wang, X. Rong, T. Wang, X. Yang, F. Xu, Z. Qin, W. Ge, B. Shen, and X. Wang, “Positive temperature coefficient of photovoltaic efficiency in solar cells based on InGaN/GaN MQWs,” Applied Physics Letters, vol. 109, no. 6, p. 062104, 2016.

[30] K. Barnham, I. Ballard, J. Barnes, J. Connolly, P. Griffin, B. Kluftinger, J. Nelson, E. Tsui and A. Zachariou, “Quantum well solar cells,” Applied Surface Science, vol. 113, no. 96, pp. 722-733, 1997.

Chapter 4

Analytical model for MQW solar cells

4.1. Introduction

The recent approach for enhancing the energy conversion efficiency of the photovoltaic devices is to reduce the losses associated with the inability to absorb lower energy photons compared to the photons being absorbed by the base material [1]. This shortcoming can be resolved by using multiple quantum wells (MQWs) inside the intrinsic region of a *p*-*i*-*n* solar cell structure [2].

In the last few decades, the MQW solar cells (MQWSCs) have been studied extensively to enhance conversion efficiency of the solar cell [2]. The efficiency limitation in the *p*-*i*-*n* solar cell (because of the trade-off between a high energy band gap, which enhances the open circuit voltage and a low energy band gap which boosts short circuit current) is overcome by the implementation of the MQWs in the intrinsic region of the *p*-*i*-*n* solar cell [2-4]. Introducing MQWs provides the flexibility to modulate the optical properties to enhance solar cell performance [5], and therefore allows independently controlling and optimizing both the current and voltage performance parameters of the solar cell [4]. It is well known that the value of energy band gap of the well material must be smaller than that of the *p*-*i*-*n* solar cell in order to have additional energy sub-band levels between conduction and valence bands, so that additional low energy photons can also be absorbed in the solar cell [1, 6, 7].

The MQWSCs have potential application in the multi-junction solar cells (MJSCs) for the energy bandgap optimization so that current matching of the top, middle and bottom cells can be achieved [8-10]. In concentrators and conventional solar cells, the prime concern is the performance degradation with the increase in device temperature. Since in MQWSC, carrier escape from quantum wells is primarily thermally activated, thus these are expected to show a better conversion efficiency dependence on temperature than the conventional cells and this makes them more feasible for concentrated solar cell applications [11, 12].

Several simulation, analytical and experimental study have been reported to investigate the performance of the MQWSC [13-17]. Renaud *et al.* [13] have shown that with the inclusion of quantum wells in a *p-i-n* solar cell, the photocurrent improves without much reduction in the open-circuit voltage (*Voc*) leading to overall increment in the photon conversion efficiency (η). Connolly *et al.* [14] have not considered capture and escape rates from the well and characterized the dark current in terms of the quantum well density of states. A model including the escape, capture and recombination of the photo-excited carriers in quantum wells was proposed by Ramey and Khoie [15] in which an improved conversion efficiency is presented by inserting MQWs in the depletion region of *p-i-n* solar cell. Aperathitis *et al.* [16] have examined the tunneling current contribution to the photocurrent at various temperatures on AlGaAs/GaAs MQWSC. Anderson [17] developed an ideal model for MQWSC, incorporating carrier generation and recombination in the QWs, and discussed the qualitative analysis of MQWSC performance.

In this work, a physics-based analytical model and silvaco atlas tool based simulation are presented and the performance parameters of the solar cell based on the developed model and simulation are scrupulously investigated. The device performance parameters of the InGaN/GaN and CdZnO/ZnO-based MQWSC are obtained and the effect of mole fraction of the well material (intrinsic region) on the *J-V* characteristics of solar cell is also studied. The thermal stability of device performance parameters is also examined by an extensive discussion on the temperature dependence of these parameters. Further, the impact of number of pairs of quantum wells on the conversion efficiency of MQWSC is also studied. Significantly, the American Society for Testing and Materials (ASTM) standards data sheets and spectral irradiance are utilized for attaining photon flux density instead of Plank's Law used in other published literature [18-19]. Further, this photon flux density is used for the calculation of performance parameters of the device. The developed analytical model for the MQWSC is also verified with the published experimental data by other researchers.

4.2. Analytical Model

The MQWSC is basically a *p-i-n* solar cell containing multiple numbers of quantum well (QWs) in the intrinsic region (active region). The MQWSC structure consists of quantum well material of energy band gap E_W less than that of the barrier material having energy band gap of E_B. With the modification in equation (3.11) of *p-i-n* solar cell, the illuminated *J-V* characteristics of the MQWSC including the generation and recombination in the well and barrier region is described by

$$J_{QW}(V) = J_s(1 + r\beta_1)[\exp(V/V_t) - 1] - qt_i[f_1 G_{WO} + (1 - f_1)G_{BO}] \quad (4.1)$$

where $r = 1 + f_1[\gamma_1 \gamma_2^2 exp(\Delta E/kT - 1)]$ includes the enhancement in the dark recombination current because of the presence of the QWs in the intrinsic region, $\gamma_1 = B_W/B_B$ is the recombination coefficient enhancement factor, $\gamma_2 = g_W/g_B$ is the effective volume densities of states enhancement factor and $\Delta E = E_B - E_W$ and other parameters involved in equation (4.1) are described in the previous chapter.

The short-circuit current density for the MQWSC can be obtained by substituting $V = 0$ in equation (4.1), if the optical generation rate in well and barrier region are known, however, in the developed analytical model it is obtained using the spectral photon flux instead of Plank' Law and is given as follows

$$J_{scQW} = -qt_i[f_1 G_{WO} + (1 - f_1)G_{BO}] = -q[f_w N_{ph}(E_B > E > E_W) + (1 - f_w)N_{ph}(E > E_B)] \quad (4.2)$$

Here, $N_{ph}(E_B > E > E_W)$ is the net photon flux density corresponding to the energies between E_B and E_W and $N_{ph}(E > E_B)$ is defined net photon flux density corresponding to the energies greater than E_B. Now, by substituting $J_{QW} = 0$ in equation (4.1) and by utilizing equation (4.2), the open circuit voltage can be obtained and is given as follows

$$V_{ocQW} = V_t \ln\left[\frac{J_s(1 + r\beta_1) - J_{scQW}}{J_s(1 + r\beta_1)}\right] \tag{4.3}$$

The V_{mQW} and J_{mQW} are the voltage and current density respectively corresponding to the maximum power density point on the *J*-*V* characteristic of the MQWSC and can be obtained in the similar way as they are obtained for the *p*-*i*-*n* solar cell in the previous chapter by the derivation of $P = JV$ with respect to voltage (V) and current density (J), and then equating $\frac{\partial P}{\partial V} = 0$ and $\frac{\partial P}{\partial J} = 0$, respectively. The final expressions that are used for obtaining them by iterative methods are as follows

$$exp\left(\frac{V_{ocQW}}{V_t}\right) - exp\left(\frac{V_{mQW}}{V_t}\right)\left[1 + \frac{V_{mQW}}{V_t}\right] = 0 \tag{4.4}$$

$$\frac{J_{mQW}}{J_{mQW} - J_{scQW} + J_s(1 + r\beta_1)} + ln\left[\frac{J_{mQW} - J_{scQW} + J_s(1 + r\beta_1)}{J_s(1 + r\beta_1)}\right] = 0 \tag{4.5}$$

Next, the other performance parameters i.e. fill factor and conversion efficiency of the MQWSC are calculated in the same way as for the *p*-*i*-*n* solar cell in the previous chapter.

The above developed analytical expressions of various performance parameters of MQWSC are valid for the constant solar irradiance. However, in real-world application of the solar cell, the irradiance level varies with geographical location, weather conditions, time in a day, and most importantly with the solar concentration (i.e. concentrated light). Therefore, to analyse the device performance with respect to solar irradiance, the performance parameters developed above has to be modified accordingly.

The short-circuit current density (J_{scQW}) available from equation (4.2) is modified and it is included (multiplied) with the term corresponding to irradinace (I) (also called as number of suns) and is given by

$$J_{scQW} = -qI[f_w N_{ph}(E_B > E > E_W) + (1 - f_w)N_{ph}(E > E_B)] \tag{4.6}$$

In equation (4.6), J_{scQW} is directly proportional to irradiance because electron-hole pair generation is directly related to the irradiance level. However, there is no need to modify open circuit voltage (V_{ocQW}), as it is automatically gets modified since J_{scQW} term is already included in equation (4.3) and it can be seen that V_{ocQW} is logarithmically dependent on the irradiance level. Finally, the conversion efficiency also automatically gets modified as per the equation (3.18) and therefore, varies logarithmically with the irradiance level similar to V_{ocQW}, as the impact of increase in J_{scQW} is compromised by the increased solar irradiance level.

4.3. Simulation

After successfully developing the analytical model for MQWSC, simulation is also performed using the Silvaco-Atlas tool [20] to further investigate the MQWSC. This section gives a brief description of how the code is developed in the Silvaco-Atlas.

In Atlas simulation, basically there are three process involved to predict the electrical behaviour of the semiconductor devices: (a) Generating atlas input files, (b) Running atlas simulation, and (c) Analysing atlas output files.

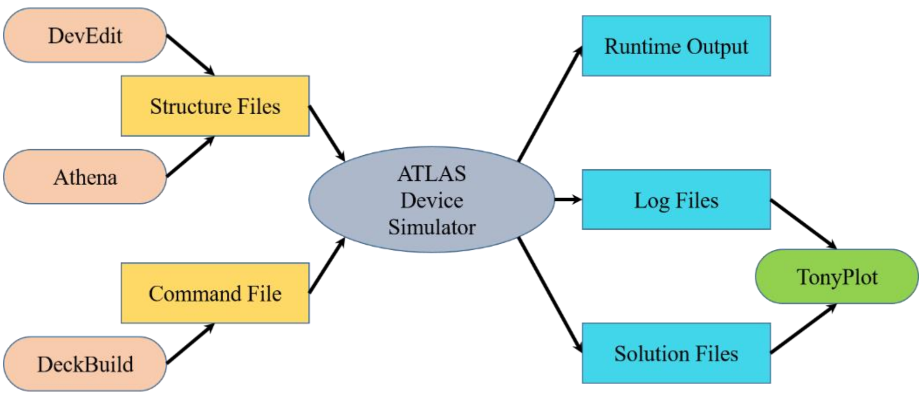

Figure 4.1 *Atlas Inputs and Outputs.*

Figure 4.1 shows the input and output files of the Atlas. The two types of input files are used in the Atlas: (a) a text file that contains Atlas commands and (b) a structure file that defines the structure to be simulated.

The output of Atlas comes in terms of three files: (a) the runtime output gives the progress, error and warning messages during the simulation process, (b) the log file stores the terminal characteristics, and (c) the solution file that stores 2D and 3D data relating to the values of solution variables.

An Atlas command file is a list of commands for Atlas to execute. The input file contains a sequence of statements. The order in which statements occur in an Atlas input file is important. There are five groups of statements that must occur in the correct order shown in Figure 4.2. Otherwise, an error message will appear, which may cause incorrect operation or termination of the program.

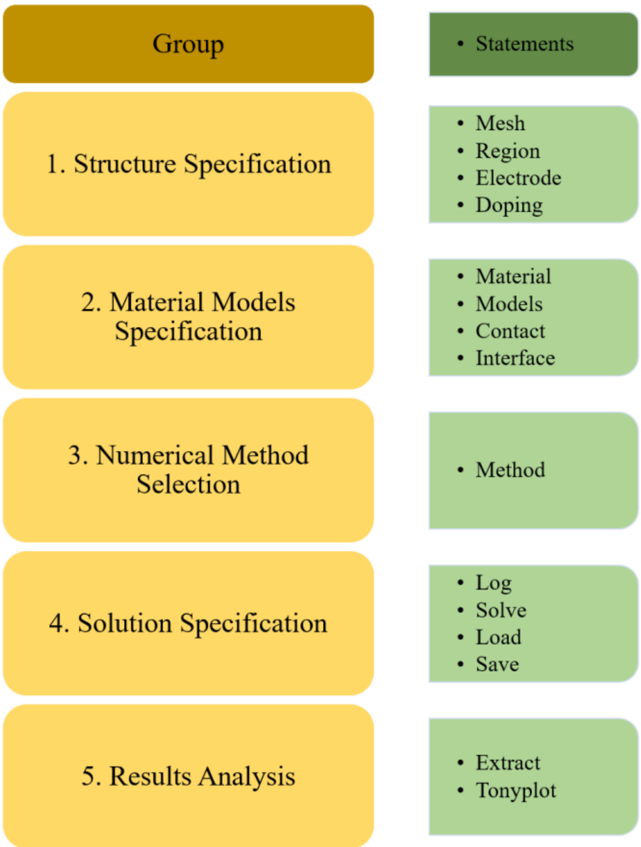

Figure 4.2 *Atlas command group with the primary statements.*

The device analysis has been carried out using Atlas from Silvaco by the incorporation of following physical models: Boltzmann statistics, Shockley-Read-Hall, Auger recombination, optical recombination/

generation model (OPTR), KP model and bandgap narrowing [20]. In Silvaco-Atlas, the drift-diffusion, Poisson, and Schrodinger equations are coupled and solved for both types of carriers, i.e. electron and hole, to study *J-V* curves.

As, the solar cell has to be analysed under illumination condition, therefore a Luminous program is there in the Atlas framework. Luminous calculate the optical intensity profiles that are converted to photo-generation rates and are directly integrated into the generation terms in the carrier continuity equation. In Atlas, the solar spectra AM0 and AM1.5 can be directly accessed by specifying them in the beam statement. In this study, numerical simulation is performed under 1-sun AM1.5G (100 mW/cm^2) of ASTM Standard Spectrum with a normal incidence of light source to the device, to study the device performance under illumination. The performance parameters associated with the solar cell are extracted using the extract statement after the log file is generated for the illuminated current-voltage characteristic.

4.4. Results and Discussion

Based on the analytical expressions derived above in section 4.2, the performance of MQW solar cells has been evaluated. The *J-V* characteristics and device performance parameters of the structure and their variation with different composition (x) of intrinsic region material are illustrated in this section. Further, the MQWSC is also analysed for various temperature of operation and different pairs of number of quantum wells.

4.4.1 InGaN/GaN-based MQWSC

InGaN alloy offers a great possibility for solar cell applications because its energy band gap can be tuned continuously from 0.7 to 3.4 eV, which can be utilized to cover almost the entire solar spectrum [21]. Apart from the direct and wide energy band gap, it possesses the favorable photovoltaic properties such as high mobility, low effective mass of carrier and high absorption coefficient, which makes them suitable for the photovoltaic application [22]. The various aspects such as optical and structural characteristics of InGaN alloy for the photovoltaic application are discussed by Jani *et al.* [22] and InGaN based *p–i–n* and quantum well solar cells are also designed, in which InGaN is deployed as the active layer [23].

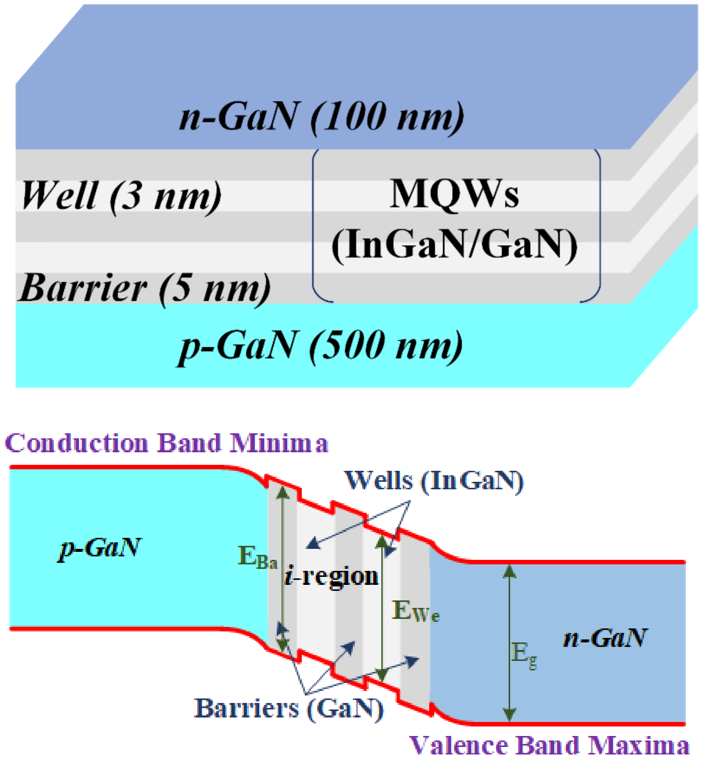

Figure 4.3 *J-V characteristics for MQWSC with different indium composition (x) of $In_xGa_{1-x}N$ in the intrinsic region.*

In this section, a discussion is presented on the results obtained for the MQWSC. The basic structure of InGaN/GaN-based MQWSC is shown in Figure 4.3 with its corresponding band diagram. The quantum well structure consists of GaN and InGaN as barrier and well materials, respectively, in the intrinsic region of the *p-i-n* structure, whereas the *p*- and *n*-regions are based on GaN material.

Figure 4.4 exhibits the dark and illuminated *J-V* characteristics of the MQWSC that consists of 20 wells of thickness 3 nm each with different indium concentration in $In_xGa_{1-x}N$ and 21 barriers each having 5 nm thickness. The device performance parameters are summarized in Table 4.1. The indium composition (x) of $In_xGa_{1-x}N$ in well has the similar effects on the *J-V* characteristics of MQWSC and its parameters as that for the *p-i-n* solar cell. As x increases from 0.1 to 0.3, J_{scQW} increases by ~41 and ~64%, respectively, whereas the V_{ocQW} decreases by ~17 and~39%, respectively, leading to the overall increment in η by ~30 and ~27%, respectively.

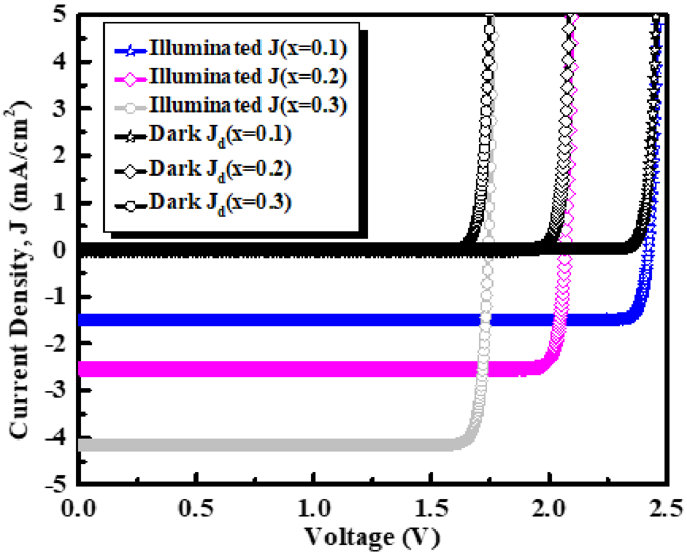

Figure 4.4 *J-V characteristics for MQWSC with different indium composition (x) of $In_xGa_{1-x}N$ in the intrinsic region.*

Table 4.1: *Performance parameters of MQWs solar cell with different indium composition of $In_xGa_{1-x}N$*

Parameters	***x* = 0.1**	***x* = 0.2**	***x* = 0.3**
J_{scQW} (mA/cm^2)	1.50	2.53	4.16
V_{ocQW} (V)	2.43	2.07	1.74
η (%)	3.42	4.89	6.69

In Figure 4.5, temperature-dependent device performance parameters of the MQWSC are exemplified. With the rise in temperature from 200 to 400 K, J_{scQW} increases from 2.37 to 2.77 mA/cm^2, respectively, and V_{ocQW} decreases from 2.32 to 1.81 V, respectively, due to which η decreases from 5.15 to 4.65%, respectively. The reason behind the increment in J_{scQW} and decrement in both V_{ocQW} and η are similar as explained for *p-i-n* solar cell, however, the impact of temperature on MQWSC is less as compared to that on *p-i-n* solar cell because the carrier escape mechanism in the quantum wells is mainly thermally activated and also MQW structure have better absorption properties than those of bulk materials [3, 24]. As the temperature increases from 200 to 400 K, MQWSC has exhibited ~9.7% decrement in the value of η as compared to 11.6% in case of *p-i-n* solar cell shown in chapter 3. Evidently, MQWSC shows favourable results with the temperature as compared to *p-i-n* solar cell.

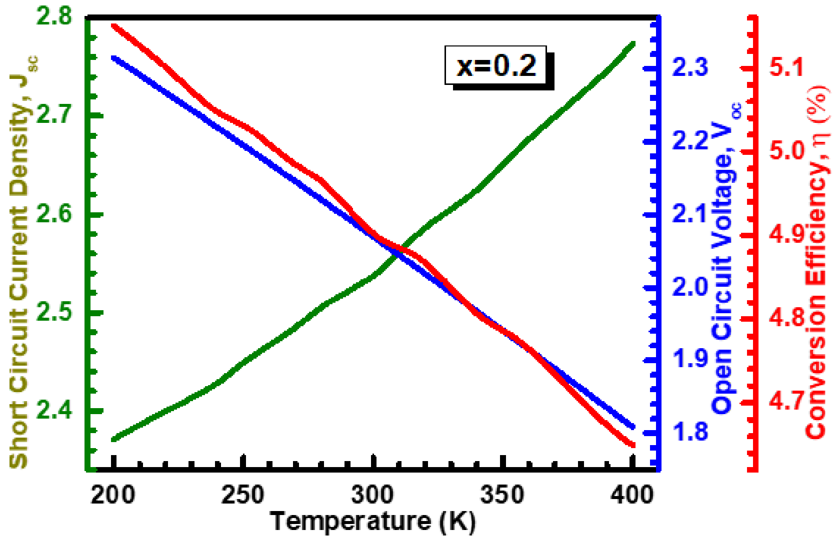

Figure 4.5 *Temperature-dependent variation of short circuit current density, open circuit voltage and conversion efficiency for MQWSC.*

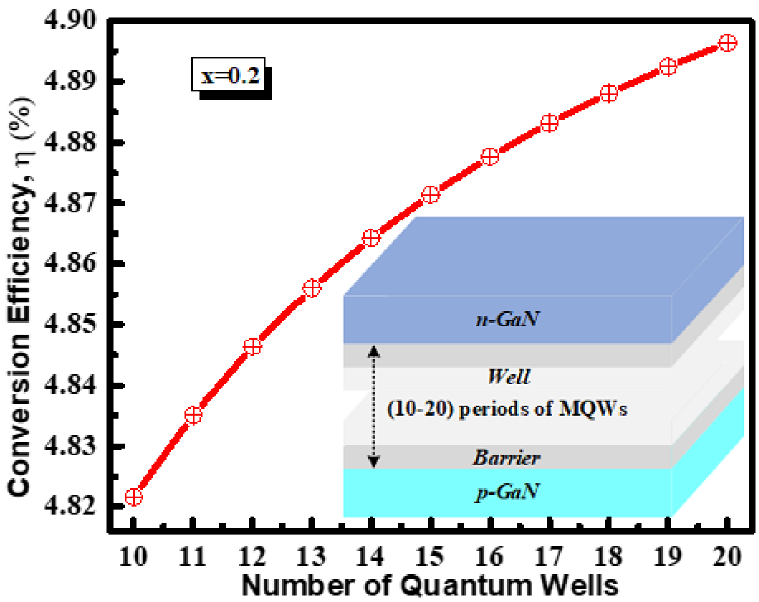

Figure 4.6 *The variation of conversion efficiency with the number of quantum wells. Inset shows the schematic of MQWSC.*

Figure 4.6 displays the variation of η with the number of quantum wells in the intrinsic region of MQWSC. As the number of quantum wells increase from 10 to 20, η increases from 4.82 to 4.89%, respectively, because of the availability of more material for the low energy photons to get absorbed efficiently, which in turn increases η [25]. The effective increase in η tends to reduce as the number of quantum wells increases beyond 20. This is because of the degradation in η of photogenerated carriers from the active region due to the fading of internal electrical field for large number of quantum wells [26]. Thus, it is concluded that, MQWSC shows improvement in overall η as the number of QWs increases till the point where the increased absorption outweighs the increased recombination [25].

Table 4.2: *Comparison of device performance parameters with the experimental results*

Parameters	**V_{ocQW} (V)**	**J_{scQW} (mA/cm^2)**	**η (%)**
Bae *et al.* [27]	2.20	1.25	2.30
Our Results	**2.24**	**1.43**	**2.61**
Farrel *et al.* [28]	1.93	2.67	-
Our Results	**1.93**	**2.53**	**-**

Table 4.3: *Comparison of temperature coefficient for device performance parameters*

Temperature Coefficient	Jeng *et al.* [29]	**Our Results**
V_{oc} (V/ ˚C)	-2.76×10^{-3}	$\mathbf{-2.46 \times 10^{-3}}$
J_{sc} (mA/cm^2/ ˚C)	0.46×10^{-3}	$\mathbf{1.0 \times 10^{-3}}$
η (%/ ˚C)	-9×10^{-4}	$\mathbf{-12 \times 10^{-4}}$

Now, the developed analytical model is also compared with the published experimentally obtained performance parameters of the MQWSC by other researchers [27-29], just to verify the developed model. During comparison, the results from the developed analytical model are obtained by inserting the materials and structural parameters of the published experimental research. The analytical results are obtained and compared in Table 4.2 and 4.3 with the published experimental research. From Table 4.2, it can be seen that, the performance parameters obtained from the analytical model are quite similar to the experimental work of others [27, 29] with acceptable error margin. Next, the temperature-dependent device performance parameters are verified with those reported by Jeng *et al.* [29] and the analytically obtained temperature coefficient are considerably similar to that of experimental work. The close agreement with the published experimental data by Bae *et al.* [27], Farrell *et al.* [28] and Jeng *et al.* [29] confirms the validity of the analytical model described here.

By comparing the results of the *p*-*i*-*n* solar cell from chapter 3 and MQWSC from this chapter, it is clear that with the inclusion of QWs in the intrinsic region of *p*-*i*-*n* structure increases the η as can be seen from Table 3.1 of Chapter 3 and Table 4.1 of this chapter, because the inclusion of QWs extends the solar cell absorption spectrum [24]. The proposed model can be used to analyse various multiple quantum well solar cell based on different well and barrier materials.

4.4.2 CdZnO/ZnO-based MQWSC

The major problem with InGaN and GaN system is their large lattice mismatch and the non-availability of native substrates. However, ZnO offers several fundamental advantages such as high breakdown strength, large excitonic binding energy, availability of native substrate, possibility of performing wet chemical processing, comparatively more resistant to radiation damage and transparency in the visible region [30]. Therefore, in this section, we have proposed the CdZnO/ZnO based MQWSC and obtained the performance parameters of the solar cell based on the developed analytical model and the Silvaco-Atlas simulation.

In recent years, the ZnO-based compound semiconductors are being probed for optoelectronic, energy and photovoltaic applications [31-35].

Our group has successfully demonstrated dual ion beam sputtering (DIBS)-grown MgZnO/CdZnO potential well for heterostructure field effect transistor (HFET) application [36] and CdZnO/ZnO MQWs for light emitting diode (LED) application [33] utilizing 15 at.% Cd in CdZnO. Here, we report utilizing 15 at.% Cd-doped ZnO in the MQWSC structure. Prior to experimental fabrication, it is imperative to perform analytical study regarding the performance parameters of the proposed MQWSC structure. Therefore, an analytical and simulation study has been undertaken to estimate the device performance parameters that will be expected from the proposed CdZnO/ZnO-based MQWSC. This is significant as DIBS-grown ZnO-based MQWSC can provide a high-efficient and cost-efficient SC option. In addition, with the energy bandgap range of 2.2 to 3.37 eV [33], CdZnO can offer a great possibility in photovoltaic devices as it covers ultraviolet-visible region of the solar spectrum.

In this work, an analytical and simulation study on the proposed CdZnO/ZnO-based MQWSC is implemented and the performance parameters of the solar cell based on the developed model are scrupulously investigated. The thermal stability of device performance parameters is also examined. In addition, this study explores the effect of variation in the QWs number on device performance of CdZnO/ZnO-based MQWSC. Further, this study delves into the possibility of efficiently absorbing high energy photons along with the probability of obtaining positive temperature coefficient of η in CdZnO/ZnO-based MQWSC. The material parameters used in this study are obtained from the Sb-doped *p*-type ZnO (SZO), Ga-doped *n*-type ZnO (GZO), CdZnO and ZnO thin films grown by DIBS. The DIBS system is remarkable in producing high-quality thin films with excellent uniformity, superior compositional stoichiometry and strong film adhesion to substrate. Apart from these, other perceptible features of the DIBS system are reduced surface roughness and *in situ* substrate pre-cleaning before the growth process using assist ion source [30].

The individual thin films of SZO, GZO, CdZnO and ZnO have been deposited by DIBS, as reported in our earlier works [30, 37, 38] and different characterization have been performed to obtain various electrical and optical parameters of the thin films. Some of the electrical and optical parameters obtained in these reports are used for analytical modelling and Silvaco-Atlas simulation of CdZnO/ZnO-based MQWSC, and they are listed in Table 4.4.

Table 4.4: *Room temperature material parameters used in the simulation and analytical modelling*

Parameters	GZO	SZO	CdZnO	ZnO
Carrier concentration (cm^{-3})	2.88×10^{19}	1.36×10^{17}	2.14×10^{16}	7.2×10^{18}
Mobility ($cm^2/V.s$)	14.16	6.75	8.38	6.5
Carrier lifetime (s)	3.0×10^{-9}	1.0×10^{-9}	1.0×10^{-9}	1.0×10^{-9}

The developed analytical model is already verified in the previous section. Now, the Silvaco-Atlas simulation model is compared with the experimentally obtained performance parameters of the GaAs-based MQWSC by Zhu *et al.* [4], just to verify the developed simulation model. While comparing, the results from the simulated model are obtained by introducing the materials and structural parameters of the published experimental research of Zhu *et al.* [4]. The results obtained are compared in Table 4.5 with the published experimental research. Table 4.5 listed the performance parameters obtained by Zhu *et al.* [4] experimentally and those from the simulated model in this work, and the error margin in both the values of the respective performance parameters. It can be seen that, the performance parameters obtained from the simulated model are quite similar to the experimental work of others [4] with acceptable error margin. The successful replication of the experimental results of GaAs-based MQWSC structure reported by Zhu *et al.* [4] confirms the validity of the simulated model in Silvaco-Atlas described here.

Table 4.5: *Validation of simulated device performance parameters with the experimental results*

Parameters	Zhu *et al.* [4]	Our Results	Error Margin (%)
V_{mQW} (V)	0.88	**0.89**	**1**
J_{mQW}(mA/cm^2)	20.83	**23.60**	**11**
V_{ocQW} (V)	0.98	**0.98**	**1**
J_{scQW} (mA/cm^2)	22.08	**24.34**	**9**
FF (%)	84.4	**87.8**	**4**
η (%)	18.33	**21.01**	**12**

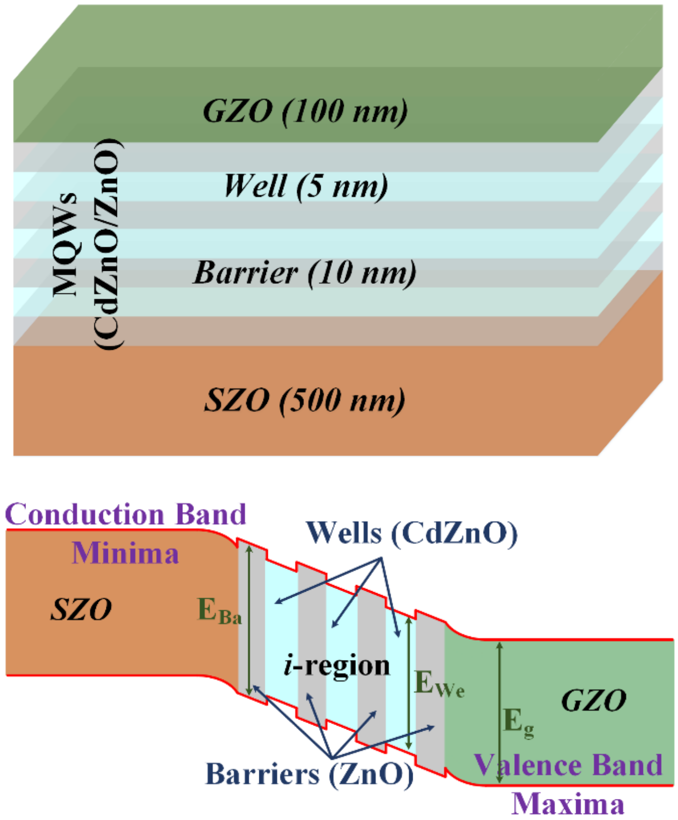

Figure 4.7 *Schematic of MQWSC structure with its corresponding band diagram.*

The CdZnO/ZnO-based MQWSC schematic is shown in Figure 4.7 with its corresponding energy band diagram. It consists of quantum well of CdZnO material with energy bandgap lesser than that of the ZnO barrier layer. On the basis of analytical expressions and simulation from Silvaco-Atlas described above, the performance of CdZnO/ZnO-based MQWSC has been investigated.

The structure consists of 100 nm of GZO, 500 nm of SZO and 3 pairs of QWs with well and barrier thicknesses of 5 and 10 nm, respectively. The dark and illuminated, *J-V* and power density versus voltage, *P-V* characteristics of the CdZnO/ZnO-based MQWSC are depicted in Figure 4.8. At room temperature, J_{sc} = 1.21 mA/cm^2, V_{oc} = 2.67 V, and η = 3.03%, are attained for the proposed MQWSC structure under AM1.5 condition from the analytical model, which are in good agreement with the simulated results obtained from the Silvaco-Atlas model as shown in Figure 4.8. From the *P-V* characteristics, maximum power density point is determined and the voltage and current density corresponding to the same are V_m = 2.55 V and J_m = 1.19 mA/cm^2.

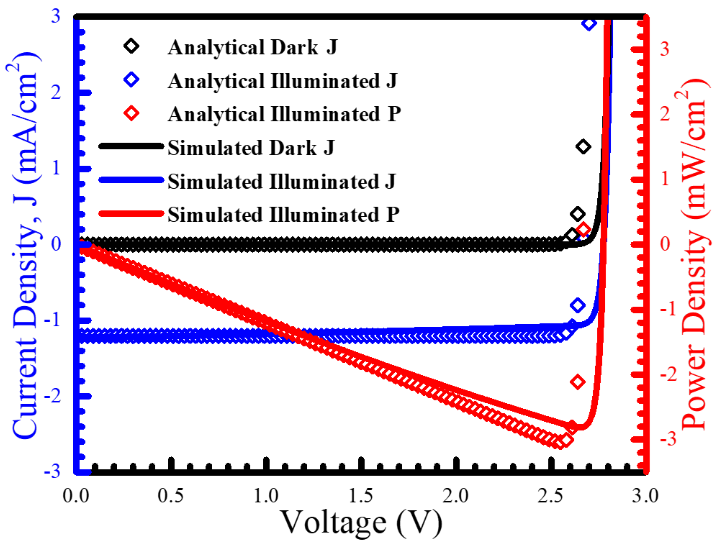

Figure 4.8 *J-V and P-V characteristic of MQWSC.*

In Figure 4.8, the obtained V_{oc} (2.67 V) is large as compared to that for GaAs material system (~ 1 V) [4] due to the high energy bandgap of ZnO-based material system. It is noteworthy that, due to the inability to absorb low energy photons, J_{sc} in CdZnO/ZnO MQWSC is small as compared to that for GaAs-based MQWSC. Therefore, it can be concluded that a compromise amongst V_{oc} and J_{sc} is to be made, depending upon the energy bandgap of the materials system. However, this study utilizes higher energy bandgap materials to efficiently utilize high energy photons. This suggests that CdZnO/ZnO-based MQWSC can be used as a top cell in MJSC structure [8-10], so that current matching in different sub-cells of the MJSC can be achieved and the maximum current can be produced.

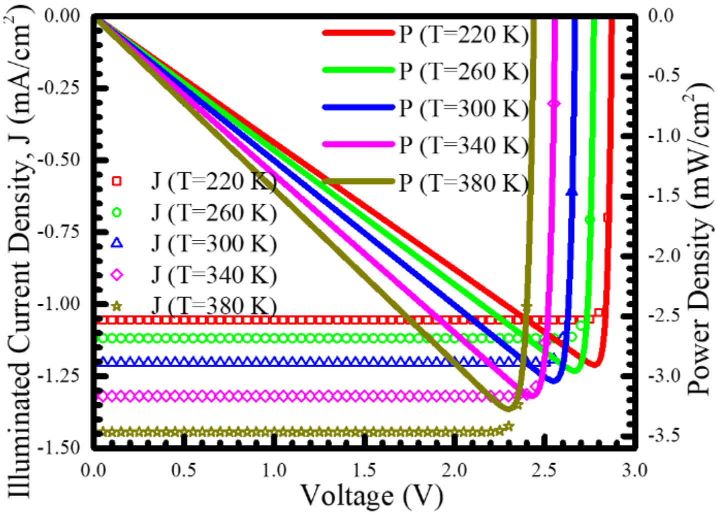

Figure 4.9 *Temperature dependent J-V and P-V characteristic of MQWSC.*

In Figure 4.9, the temperature dependent *J-V* and *P-V* characteristics of the CdZnO/ZnO-based MQWSC are described for same structural parameters as given in Figure 4.7. It can be seen that J_{sc} increases with a rise in temperature. As evident from equation (3.2) from chapter 3, E_g decreases with the operating temperature increase and the extra lower energy photons will get absorbed, that leads to increase in J_{sc}. However, the rise in temperature leads to a decrease in V_{oc}. Equation (4.3) shows that V_{oc} is directly proportional to J_{sc} and inversely proportional to J_s, yet the influence of J_s on V_{oc} is comparatively higher than that of J_{sc}, leading to an overall decrease in V_{oc} with temperature [39, 40]. The increase in J_s is caused by a decrease in *Eg* with the increase in temperature. The power density peak, as shown in Figure 4.9, drifts toward lower applied voltages with increasing temperature, which can be attributed to the coherent devaluation in V_{oc}. It is interesting to note that, in Figure 4.9, unlike other material systems such as Ge, Si, and GaAs [41], with the temperature increase from 220 to 380 K, the power density peak magnitude increases from ~2.91 to ~3.27 mW/cm^2 in ZnO-based MQWSC. The observed behaviour can be attributed to the higher rate of change in the photocurrent for CdZnO/ZnO-based MQWSC, than that of V_{oc}. The positive thermal power density coefficient (2.25×10^{-3} mW/cm^2/˚C) indicates that CdZnO/ZnO-based MQWSCs can be used in concentrator photovoltaic applications where good thermal performance is indispensable.

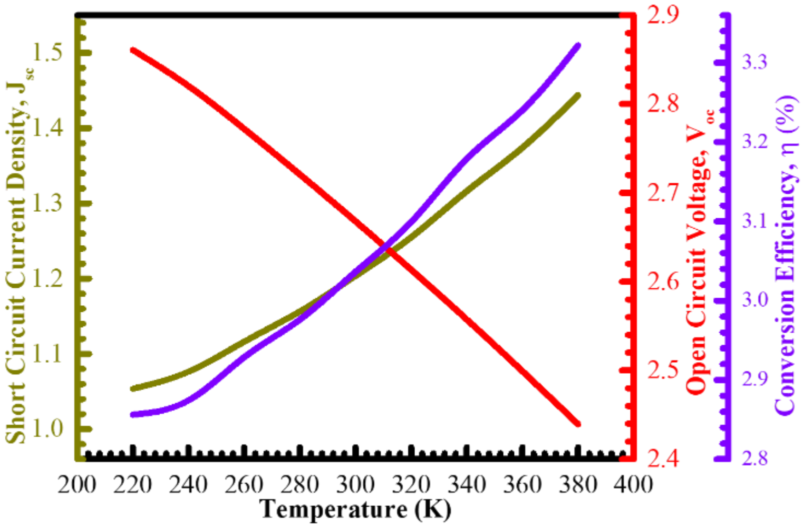

Figure 4.10 *Temperature dependence of performance parameters of MQWSC.*

In Figure 4.10, the variation of performance parameters such as J_{sc}, V_{oc}, and η with the operating temperature are shown for CdZnO/ZnO-based MQWSC with the same structural parameters as described in Figure 4.7. With the temperature increase from 220 to 380 K, J_{sc} increases from 1.05 to 1.44 mA/cm^2. However, V_{oc} decreases from 2.86 to 2.43 V. A higher increase in J_{sc} (27.1% increase) compared to the reduction in V_{oc} (17.7% decline), leads to an overall increment in η from 2.85 to 3.32% with increasing operating temperature. It is seen in Figure 4.10 that V_{oc} has a negative temperature coefficient (-2.63×10^{-3} V/˚C) while both J_{sc} and η have positive temperature coefficients i.e. 2.43×10^{-3} mA/cm^2.˚C and 2.91×10^{-3} %/˚C, respectively. Therefore, unlike GaN-based

MQWSC, conversion efficiency have positive temperature coefficient in ZnO-based MQWSC indicating better thermal performance.

Figure 4.11 exhibits the variation of performance parameters with the number of QWs (CdZnO as well layer and ZnO as barrier layer) in the intrinsic region of MQWSC. As the number of QWs increases from 3 to 19, the performance parameters of MQWSC decreases i.e. J_{sc} by ~2.21%, V_{oc} by ~0.04% and η by ~2.26%. As reported in prior literature [25], J_{sc} generally increases with the increase in number of QWs. However, here an opposite trend is observed for J_{sc} with increasing the number of QWs in CdZnO/ZnO-based MQWSC. This is probably due to the high energy bandgap of CdZnO and ZnO (used as well and barrier materials), that can absorb photons with smaller wavelengths with spectral power densities lesser than 1 W/m^2.nm. Bae *et al.* [42] have also observed similar results for InGaN/GaN material system. Now, as increase in the number of QWs enhances the recombination rate due to the increase in number of interface available for recombination, therefore leading to the decrease in V_{oc}. The combined effect of decrease in both the performance parameters, J_{sc} and V_{oc} leads to the decrease in η as shown in Figure 4.11.

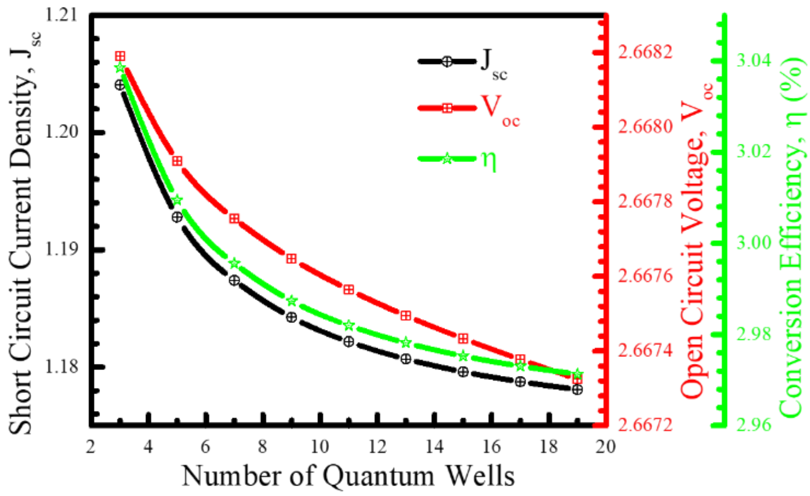

Figure 4.11 *The variation of performance parameters with the number of quantum wells.*

Mostly, performance parameters of the solar cells are reported at standard test condition (STC, i.e. irradiance level of 100 mW/cm^2 at

AM1.5G spectrum and at 25 °C). However, in real world applications, the solar cells are operated in non-STC, i.e., solar irradiance level (I) varies with geographical location, weather conditions, and time in a day [43, 44]. Therefore, here a study is performed to analyse the effect of solar irradiance, I = 10 to 5000 mW/cm^2 on CdZnO/ZnO-based MQWSC characteristic and its performance parameters. Here, the analysis is also performed for more than 1 sun i.e. under concentrated light, to investigate the performance of MQWSC under concentrated light [45]. For the analysis of performance parameters of MQWSC under different solar irradiance level, the modified short-circuit current density given by equation (4.6) is used instead of equation (4.2).

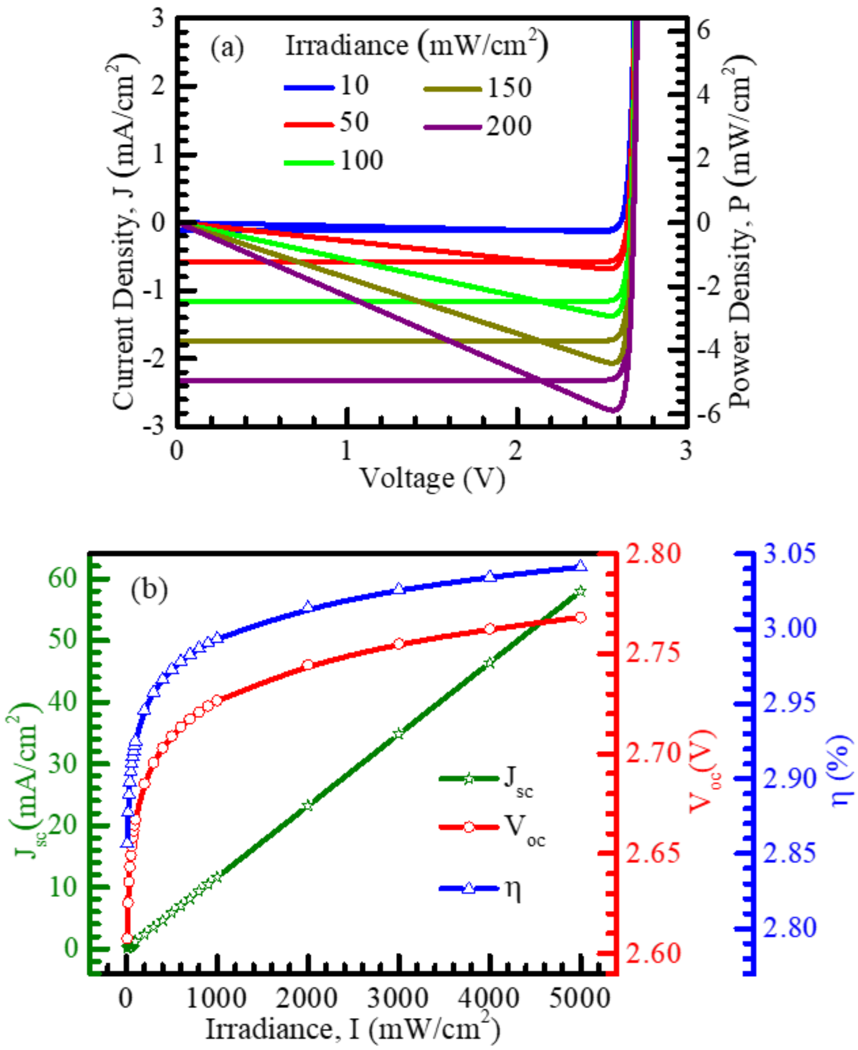

Figure 4.12 *(a) J-V and P-V characteristic with variation in Solar Irradiance level (10 to 200 mW/cm^2), (b) performance parameters of MQWSC with variation in solar irradiance level (10 to 5000 mW/cm^2).*

The variation of the *J-V* and *P-V* characteristics of the CdZnO/ZnO-based MQWSC with the change in *I* is shown in Figure 4.12 (a). The power density increases from 0.28 to 5.89 mW/cm^2 with the increase in *I* from 10 (0.1 sun) to 200 (2 suns) mW/cm^2, respectively. The SC performance parameters vary with changes in *I*, as can be seen in Figure 4.12 (b), and similar results are also reported by Dalal *et al.* [43]. However, in this work, the analysis with *I* is further extended to 50 suns to get better understanding of the effects appeared with increasing irradiance. It can be seen form (5) that J_{sc} is linearly dependent on *I*, due to the additional photo-generated charge carriers with the corresponding rise in *I*, as shown in Figure 4.12 (b) [43, 44]. However, V_{oc} increases logarithmically with *I*, since V_{oc} benefits arises from its logarithmic dependence on J_{sc}. As *I* increases from 10 to 5000 mW/cm^2, the SC performance parameters increase as follows: J_{sc} from 0.12 to 57.98 mA/cm^2, V_{oc} from 2.60 to 2.77 V and η from 2.85 to 3.04 %. It appears that η also varies logarithmically with the corresponding rise in *I* similar to V_{oc}, and it is because of the compromise of the linear effect of J_{sc} with that of *I*; therefore, it varies according to V_{oc} [45]. So, it is concluded that the SC performance decreases as *I* decreases and it might be due to bad weather condition, geographical locations etc. However, the performance can be improved by using solar concentrators acting as a source of multiple number of suns. The results specify the strong prospective of CdZnO/ZnO-based large-area and cost-effective MQWSC for concentrated photovoltaic applications.

4.5. Conclusion

A physics based generic analytical model for MQWSC is developed for the calculation of device performance parameters and obtaining *J-V* characteristics of the solar cell. The results show that the inclusion of QWs in the depletion region of the *p-i-n* solar cell leads to the enhancement of ~27% in the conversion efficiency for the same composition (x = 0.1) of $In_xGa_{1-x}N$ in InGaN/GaN-based solar cell. For InGaN/GaN-based MQWSC, the conversion efficiency increases by ~30 and ~27% if the indium composition in $In_xGa_{1-x}N$ increases from x

= 0.1 to 0.2 and further to x = 0.3. The temperature-dependent study of the device performance parameters has shown that, with the increase in temperature, conversion efficiency decreases. Approximately, 9.7% decrement in the conversion efficiency of the MQWSC is obtained as the temperature increases from 200 to 400 K. The MQWSC has demonstrated more favourable temperature dependence of the efficiency compared to *p*-*i*-*n* solar cell as seen from previous chapter. The study of the effect of number of quantum wells on the solar cell have shown that the increase in the number of QWs from 10-20 leads to the increment in conversion efficiency from 4.28 to 4.89%. The analytical model described, and the corresponding results analysed here can be used as the suitable model for estimating the performance parameters of MQWSC consisting of various material system.

An analytical and simulation study has been presented for the CdZnO/ZnO-based MQWSC with CdZnO/ZnO as the intrinsic layer, SZO as *p*-type layer and GZO as *n*-type layer of the *p*-*i*-*n* solar cell. The study of the device performance parameters with temperature shown a negative temperature coefficient of V_{oc}, and positive temperature coefficient of both J_{sc} and η i.e. -2.63×10-3 mV/˚C, 2.43×10-3 mA/cm2.˚C and 2.91×10-3 %/˚C, respectively. Approximately, 14% increment in the conversion efficiency of MQWSC is observed as the temperature increases from 220 to 380 K. This work suggests, that CdZnO/ZnO MQWSCs can be efficiently utilized in concentrator photovoltaic applications, where positive temperature coefficient of η is crucial. An increase in the number of QWs from 3 to 19 leads to the decrement in the performance parameters of MQWSC. This study significantly explores the possibility of efficient absorption of high energy photons and probability of positive temperature coefficient of η utilizing a low-cost ZnO-based MQWSC.

The change in solar irradiance, *I* leads to the change in all performance parameters of MQWSC. Approximately, 6% increase is observed in the η of MQWSC, as I increases from 10 to 5000 mW/cm^2. This study considerably explores the likelihood of efficient absorption of short wavelength photons and improving η of MQWSC by using concentrator.

4.6. References

[1] R. Corkish and C. B. Honsberg, “Dark currents in double heterostructure and quantum-well solar cells,” 26th IEEE Photovoltaic Specialists Conference, pp. 923-926, 1997.

[2] K. W. J. Barnham, and G. Duggan, “A new approach to high-efficiency multi-band-gap solar cells,” Journal of Applied Physics, vol. 67, no. 7, pp.3490-3493, 1990.

[3] K. Barnham, I. Ballard, J. Barnes, J. Connolly, P. Griffin, B. Kluftinger, J. Nelson, E. Tsui and A. Zachariou, “Quantum well solar cells,” Applied Surface Science, vol. 113, pp. 722-733, 1997.

[4] L. Zhu, M. Yoshita, J. L. Tsai, Y. C. Wang, C. Y. Hong, G. C. Chi, C. Kim, P. Yu, and H. Akiyama, “Diagnosis of GaInAs/GaAsP Multiple Quantum Well Solar Cells With Bragg Reflectors via Absolute Electroluminescence,” IEEE Journal of Photovoltaics, vol. 7, no. 3, pp. 781-786, 2017.

[5] K. Toprasertpong, T. Inoue, Y. Nakano, & M. Sugiyama “Investigation and modeling of photocurrent collection process in multiple quantum well solar cells,” Solar Energy Materials and Solar Cells, vol. 174, pp. 146-156, 2018.

[6] J. C. Rimada, L. Hernández, J. P. Connolly, and K. W. J. Barnham, “Conversion efficiency enhancement of AlGaAs quantum well solar cells,” Microelectronics Journal, vol. 38, no. 4-5, pp. 513-518, 2007.

[7] K. Xu, L. Huang, Z. Zhang, J. Zhao, Z. Zhang, L. W. Snyman, and J. W. Swart, "Light emission from a poly-silicon device with carrier injection engineering," Materials Science and Engineering: B, vol. 231, pp. 28-31, 2018.

[8] S. Kotamraju, M. Sukeerthi, and S. E. Puthanveettil, "Modeling of InGaP/InGaAs-GaAsP/Ge multiple quantum well solar cell to improve efficiency for space applications," Solar Energy, vol. 186

pp. 328-334, 2019.

[9] B. Kim, K. Toprasertpong, A. Paszuk, O. Supplie, Y. Nakano, T. Hannappel, and M. Sugiyama, "GaAsP/Si tandem solar cells: Realistic prediction of efficiency gain by applying strain-balanced multiple quantum wells," Solar Energy Materials and Solar Cells, vol. 180, pp. 303-310, 2018.

[10] N. G. Young, E. E. Per, R. M. Farrell, M. Iza, S. Keller, J. E. Bowers, S. Nakamura, S. P. DenBaars, and J. S. Speck, "High-performance broadband optical coatings on InGaN/GaN solar cells for multijunction device integration," Applied Physics Letters, vol. 104, no. 16, p. 163902, 2014.

[11] K. Y. Lai, G. J. Lin, C. Y. Chen, Y. L. Lai, and J. H. He, "Origin of hot carriers in InGaN-based quantum-well solar cells," IEEE Electron Device Letters, vol. 32, no. 2, pp.179-181, 2010.

[12] W. Yanwachirakul, H. Fujii, K. Toprasertpong, K. Watanabe, M. Sugiyama, and Y. Nakano, "Effect of Barrier Thickness on Carrier Transport Inside Multiple Quantum Well Solar Cells Under High-Concentration Illumination," IEEE Journal of Photovoltaics, vol. 5, no. 3, pp.846-853, 2015.

[13] P. Renaud, M. Vilela, A. Freundlich, A. Bensaoula, and N. Medelci, "Modeling p-i(MQW)-n solar cells: A contribution for a near optimum design," Proceedings IEEE Conference Photovoltaic Energy Conversion, New York, pp. 1787-1790, 1995.

[14] J. P. Connolly, J. Nelson, K. W. Barnham, I. Ballard, C. Roberts, J. S. Roberts, C. T. Foxon, "Simulating multiple quantum well solar cells," 28th IEEE Photovoltaic Specialists Conference, pp. 1304-1307, 2000.

[15] S. M. Ramey and R. Khoie, "Modeling of multiple-quantum-well solar cells including capture, escape, and recombination of photoexcited carriers in quantum wells," IEEE Transactions on Electron Devices, vol. 50, no. 5, pp. 1179-1188, 2003.

[16] E. Aperathitis, A.C. Varonides, C.G. Scott, D. Sand, V. Foukaraki, M. Androulidaki, Z. Hatzopoulos, P. Panayotatos, "Temperature

dependence of photocurrent components on enhanced performance GaAs/AlGaAs multiple quantum well solar cells," Solar Energy Materials & Solar Cells, vol. 70, no. 1, pp. 49-69, 2001.

[17] N. G. Anderson, "Ideal theory of quantum well solar cells," Journal of Applied Physics, vol. 78, no. 3, pp. 1850-1861, 1995.

[18] N. E. H. Gorji, H. Movla, F. Sohrabi, A. Hosseinpour, M. Rezaei, and H. Babaei, "The effects of recombination lifetime on efficiency and J-V characteristics of $In_xGa_{1-x}N$/GaN quantum dot intermediate band solar cell," Physica E: Low-dimensional Systems and Nanostructures, vol. 42, no. 9, pp. 2353-2357, 2010.

[19] A. Asgari and K. Khalili, "Temperature dependence of InGaN/GaN multiple quantum well based high efficiency solar cell," Solar Energy Materials & Solar Cells, vol. 95, no. 11, pp. 3124-3129, 2011.

[20] ATLAS User's Manual, Silvaco Inc., Santa Clara, CA, USA, 2015.

[21] Y. L. Tsai, C. C. Lin, H. V. Han, C. K. Chang, H. C. Chen, K. J. Chen, W. C. Lai, J. K. Sheu, F.I Lai, P. Yu, H. C. Kuo, "Improving efficiency of InGaN/GaN multiple quantum well solar cells using CdS quantum dots and distributed Bragg reflectors," Solar Energy Materials & Solar Cells, vol. 117, pp. 531-536, 2013.

[22] O. Jani, I. Ferguson, C. Honsberg, and S. Kurtz, "Design and characterization of GaN/InGaN solar cells," Applied Physics Letters, vol. 91, no. 13, p. 132117, 2007.

[23] O. Jani, C. Honsberg, A. Asghar, D. Nicol, I. Ferguson, A. Doolittle, and S. Kurtz, "Characterization and analysis of InGaN photovoltaic devices," 31st IEEE Photovoltaic Specialists Conference, pp. 37-42, 2005.

[24] B. W. Liou, "Temperature of $In_xGa_{1-x}N$/GaN solar cells with a multiple-quantum-well structure on SiCN/Si(111) substrates," Solar Energy Material and Solar Cells, vol. 114, pp. 141-146, 2013.

[25] B. W. Liou, "Design and fabrication of $In_xGa_{1-x}N$/GaN solar cells with a multiple-quantum-well structure on SiCN/Si(111)

substrates," Thin Solid Films, vol. 520, no. 3, pp. 1084-1090, 2011.

[26] T. Inoue, K. Watanabe, K. Toprasertpong, H. Fujii, M. Sugiyama, and Y. Nakano, "Enhanced Light Trapping in Multiple Quantum Wells by Thin-Film Structure and Backside Grooves With Dielectric Interface," IEEE Journal of Photovoltaics, vol. 5, no. 2, pp. 697-703, 2015.

[27] S. Y. Bae, J. P. Shim, D. S. Lee, S. R. Jeon, and G. Namkoong, "Improved Photovoltaic Effects of a Vertical-Type InGaN/GaN Multiple Quantum Well Solar Cell," Japanese Journal of Applied Physics, vol. 50, no. 9, p. 092301, 2011.

[28] R. M. Farrell,1, C. J. Neufeld, S. C. Cruz, J. R. Lang, M. Iza, S. Keller, S. Nakamura, S. P. DenBaars, U. K. Mishra, and J. S. Speck, "High quantum efficiency InGaN/GaN multiple quantum well solar cells with spectral response extending out to 520 nm," Applied Physics Letters, vol. 98, no. 20, p. 201107, 2011.

[29] M. J. Jeng, Y. L. Lee, and L. B. Chang, "Temperature dependences of $In_xGa_{1-x}N$ multiple quantum well solar cells," Journal of Physics D: Applied Physics, vol. 42, no. 10, p. 105101, 2009.

[30] S. K. Pandey, S. K. Pandey, V. Awasthi, A. Kumar, U. P. Deshpande, M. Gupta, S. Mukherjee, "Influence of annealing temperature on ZnO thin films grown by dual ion beam sputtering," Bulletin of Materials Science, vol. 37, no. 5, pp. 983-989, 2014.

[31] R. Bhardwaj, P. Sharma, R. Singh, M. Gupta, and S. Mukherjee, "High responsivity $Mg_xZn_{1-x}O$ based ultraviolet photodetector fabricated by dual ion beam sputtering," IEEE Sensors Journal, vol. 18, no. 7 pp. 2744-2750, 2018.

[32] J. Huang, S. Chu, J. Kong, L. Zhang, C.M. Schwarz, G. Wang, L. Chernyak, Z. Chen, and J. Liu, "ZnO p-n Homojunction Random Laser Diode Based on Nitrogen-Doped p-type Nanowires," Advanced Optical Materials, vol. 1, no. 2, pp.179-185, 2013.

[33] V. Awasthi, S.K. Pandey, S. Verma, S. Mukherjee, "Room temperature blue LED based on p-ZnO/(CdZnO/ZnO) MQWs/n-

ZnO," Journal of Luminescence, vol. 180, pp. 204-208, 2016.

[34] K. Matsushima, R. Shimizu, T. Ide, D. Yamashita, H. Seo, K. Koga, M. Shiratani, and N. Itagaki, "Fabrication of ZnInON/ZnO multi-quantum well solar cells," Thin Solid Films, vol. 587, pp. 106-111, 2015.

[35] L. Ma, Z. Xia, V. Atuchin, M. Molokeev, S. Auluck, A. H. Reshak, and Q. Liu, "Engineering oxygen vacancies towards self-activated $BaLuAl_xZn_{4-x}O_{7-(1-x)/2}$ photoluminescent materials: an experimental and theoretical analysis," Physical Chemistry Chemical Physics, vol. 17, no. 46, pp. 31188-31194, 2015.

[36] M. A. Khan, R. Singh, R. Bhardwaj, A. Kumar, A. K. Das, P. Misra, A. Kranti, and S. Mukherjee, "Enhanced sheet charge density in DIBS grown CdO alloyed ZnO buffer based heterostructure," IEEE Electron Device Letters, vol. 39, no. 6, pp. 827-830, 2018.

[37] S. K. Pandey, V. Awasthi, S. Verma, S. Mukherjee, "Blue electroluminescence from Sb-ZnO/Cd-ZnO/Ga-ZnO heterojunction diode fabricated by dual ion beam sputtering," Optics express, vol. 22 no. 25 pp. 30983-30991, 2014.

[38] V. Garg, B. S. Sengar, V. Awasthi, A. Kumar, R. Singh, S. Kumar, V. V. Atuchin, and S. Mukherjee, "Investigation of Dual-Ion Beam Sputter-Instigated Plasmon Generation in TCOs: A Case Study of GZO," ACS Applied Material Interfaces, vol. 10, no. 6, pp. 5464-5474, 2018.

[39] M. A. Green, Solar cells: Operating principles, technology, and system applications. Englewood Cliffs, NJ, Prentice-Hall, Incorporation, p. 80, 1982.

[40] K. Wang, O. Gunawan, T. Todorov, B. Shin, S. J. Chey, N. A. Bojarczuk, D. Mitzi, and S. Guha, "Thermally evaporated Cu_2 $ZnSnS_4$ solar cells," Applied Physics Letters, vol. 97, no. 14, p. 143508, 2010.

[41] J. C. Fan, "Theoretical temperature dependence of solar cell parameters," Solar cells, vol. 17, no. 2-3 pp. 309-315, 1986.

[42] H. Bae, J. B. Park, K. Fujii, H. J. Lee, S. H. Lee, S. W. Ryu, J.K. Lee and J. S. Ha, “The Effect of the number of InGaN/GaN pairs on the photoelectrochemical properties of InGaN/GaN multi quantum wells,” Applied Surface Science, vol. 401, pp. 348-352, 2017.

[43] R. Dahal, J. Li, K. Aryal, J. Y. Lin, and H. X. Jiang, “InGaN/GaN multiple quantum well concentrator solar cells,” Applied Physics Letters, vol. 97, no. 7, p.073115, 2010.

[44] M. J. Yang, and M. Yamaguchi, "Properties of GaAs/InGaAs quantum well solar cells under low concentration operation," Solar Energy Materials and Solar Cells, vol. 60, no. 1, pp. 19-26, 2000.

[45] H. Ohtsuka, T. Kitatani, Y. Yazawa, and T. Warabisako, "Numerical prediction of InGaAs/GaAs MQW solar cell characteristics under concentrated sunlight," Solar Energy Materials and Solar Cells, vol. 50, no. 1-4, pp. 251-257, 1998.

Chapter 5

Thin film deposition and characterization techniques

In this chapter, the deposition system and the various characterization technique utilized for the thin films are discussed briefly. The detailed description regarding the substrate selection and its cleaning procedure, is also discussed. The single step processes to deposit thin films under vacuum have attracted a lot of attention, as these technique not only suitable for uniform high quality thin film with precise composition but also used for large-scale production [1]. The CdZnO/ZnO-based MQWs are deposited using the single target of CdZnO and ZnO each by utilizing DIBS system. The optical properties, depth profile, elemental interdifussion and MQW periodicity of the deposited thin films have been observed by different characterization techniques. The optical properties of the thin films have been characterized by the spectroscopic ellipsometry (SE). The depth profile and elemental interdifussion has been characterized by Secondary Ion Mass Spectroscopy (SIMS). The MQW periodicity has been detected by High-Resolution Transmission Electron Microscopy (HRTEM).

5.1. Substrate selection and its cleaning procedure

Although the quality of the deposited thin film depends on the deposition technique, yet the nature and surface condition of the substrate plays vital role for high quality thin film growth. Some desired properties of the substrate are a) low surface roughness, (b) low chemical reactivity, and (c) good mechanical strength. The choice of substrate selection is depends on the application type, cost, process, and packaging of the device. Silicon and corning glass are the substrate used in this thesis work for the deposition of thin films. Contamination present at the substrate surface affects the film purity and their adhesion to the substrates, therefore, it is necessary to clean the substrate properly before the deposition of the sensing film. Depending on the type of substrate and type of contaminants may present on the substrate an appropriate cleaning procedure were followed to clean the substrates.

5.1.1 Silicon substrate cleaning procedure

In this thesis work, the following steps were employed to clean the Si substrates.

- Remove dust using pipette like blower before cleaning the substrates.
- Ultrasonic cleaning in diluted TCE solution to remove any fingerprints on the wafer or any other heavy residue on the wafer.
- Rinse with DI water to remove any TCE remaining.
- Ultrasonic cleaning in acetone to remove the organic remnants/contaminants from the wafers.
- Rinse with DI water to remove any acetone remaining.
- Ultrasonic cleaning in diluted isopropanol solution for dissolving non-polar contaminants which are left on the wafers.
- Rinse with DI water to remove any isopropanol remaining.
- Dip in HF solution to remove native silicon dioxide from wafers.
- Rinse with DI water.
- Purge with high purity nitrogen gas to remove any water remaining on the substrate.

5.1.2 Glass substrate cleaning procedure

In this thesis work, the following steps were employed to clean the glass substrates.

- Ultrasonic cleaning with methanol to remove any fingerprints, or oil contamination.
- Rinse with DI water to remove any soap remaining.
- Ultrasonic cleaning in acetone to remove tiny dust particles on the surface through agitation.
- Rinse with DI water to remove any acetone remaining.
- Ultrasonic cleaning in diluted isopropanol solution for dissolving non-polar contaminants which are left on the wafers.
- Rinse with DI water and blow off the water-droplets.

- Purge with high purity nitrogen gas to remove any water remaining on the substrate.

5.2. Deposition Equipment

In this thesis work, physical vapour deposition methods are employed for the deposition of thin films and contacts formation. Dual ion beam sputtering (DIBS) system is used for the thin film deposition and direct current (DC) magnetron sputtering is used for the contact formation on the device.

5.2.1 DIBS system

The DIBS system is used for the deposition of multiple thin films for the formation of MQW structure. The DIBS System is based on physical vapour deposition technique utilized for deposition of thin films for various electronics and optoelectronics devices, such as light-emitting diode (LED), photodetector, and photovoltaic in ultrahigh vacuum conditions [2]-[4]. The DIBS system is incredible when it comes to realize high-quality thin films with precise element composition, superior film adhesion to the substrate, diminished surface roughness, and the provision of in situ precleaning of substrates prior to film deposition [5]. The DIBS system also offers the advantage of uniform deposition on a large area, and thus, it can be helpful in realization of large-area photovoltaic cell.

The advantages of the DIBS system comes from the two ion sources: (1) depositing source or primary ion source and (2) assist source or secondary ion source [4]. The schematic of the deposition chamber (DPC) and photographic image of DIBS system are shown in Figure 5.1 and 5.2, respectively.

The primary ion source is used to sputter materials from a target to deposit it on the substrate. In the DIBS system, four different targets at a time can be mounted on a rotating and water-cooled target assembly, and an appropriate target can be selected for the depostion of thin film. The secondary ion source which is directed towards the substrate holder assembly is used to pre-clean (etch) the substrate surface before the start of thin film deposition process and also to remove any island formation during the deposition process. The angle of 45^o is fixed between the target assembly and primary ion source while the angle of 60^o is maintained between the substrate holder assembly and assist ion source. The inside assembly of the DPC is shown in Figure 5.1.

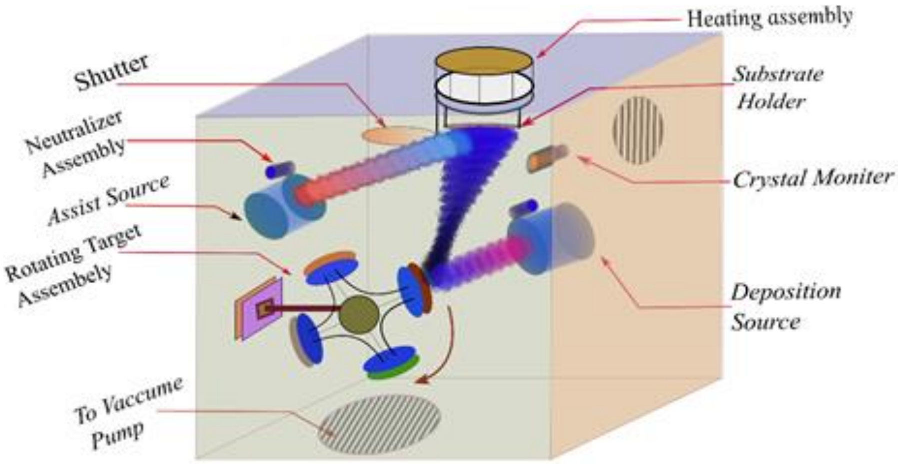

Figure 5.1 *Schematic diagram of Dual Ion Beam Sputtering System.*

There are two chamber in the DIBS: (1) deposition chamber (DPC) and (2) load lock chamber (LLC). The deposition process is performed in DPC, while the LLC is simply used for loading and unloading the sample from the DPC such that there is no need to vent the DPC every time sample has to be loaded or unloaded. Gate valve is used to separate both chambers. Two separate turbo pumps with the backing by separate rotary pumps maintain the vacuum in both DPC and LLC by rotating at 27 and 51 KRPM respectively. The vacuum gauges are connected to the DPC and LLC to measure and monitor the vacuum level at background and working conditions. The background pressure is maintained at ~10^{-8} mbar inside both the DPC and LLC. The DPC is manufactured from Stainless steel or Pyrex glass material because these materials are non-magnetic, easy to repair via welding, non-corrosive and highly malleable features [3]. The substrate holder is placed just below the heater assembly so that desired temperature value is maintained, which ranges from room temperature to 1000 ^{o}C during the annealing as well as deposition processes. The water chiller is associated with the system to cool down the deposition chamber, vacuum pumps and target assembly. Deposition parameters in DIBS system, i.e. gas pressure, gas composition, deposition temperature, and RF power are controlled by auto controller and various power supply unit associated with the DIBS system.

Figure 5.2 *Photographic image of Dual Ion Beam Sputtering System.*

In DIBS system, plasma of Ar^+ ion and electron is generated using ion sources made by Kauffman Robinson [2]. The primary ion source which is used to generate plasma, consist of three key parts: discharge chamber, grids and hollow-cathode neutralizer. The Ar gas, which is to be ionized utilizing inductive coupling is inserted into alumina or quartz chamber encircled with an RF powered coil. The free electrons are excited by RF field until they have sufficient energy to create Ar^+ and electron pair out of Ar gas. The voltages are applied on three-grids inside primary source to eject and focus the Ar^+ ions. The neutralizer of the primary ion source assembly is used to neutralize the Ar^+ beam [2]. The schematic diagram of primary ion source is shown in Figure 5.3.

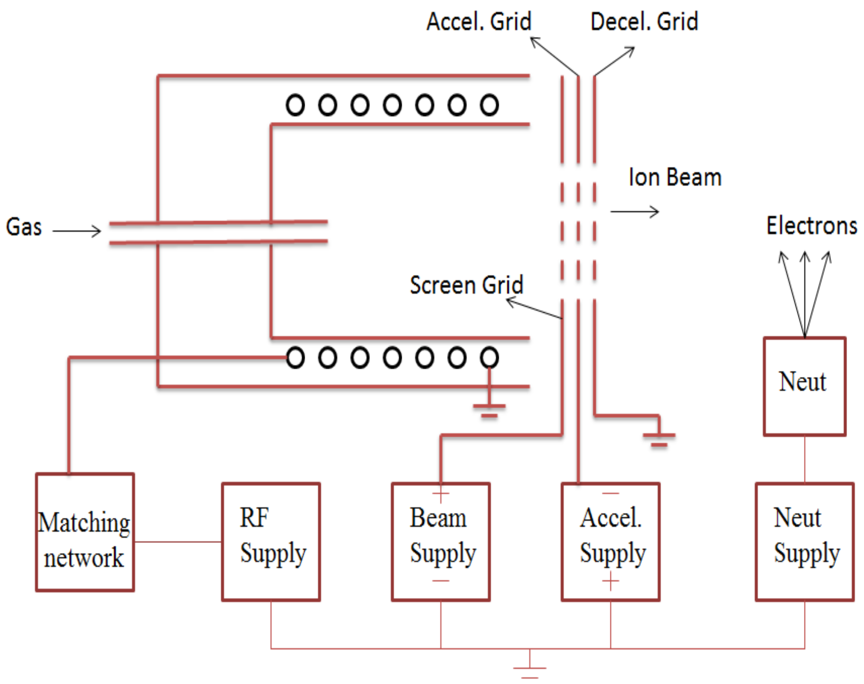

Figure 5.3 *Schematic diagram of primary ion beam source.*

The assist ion source consists of auto controller along with three power supplies i.e. keeper, emission and discharge power supplies, and hollow-cathode neutralizer assembly as shown in Figure 5.4. The keeper power supply ignite the hollow cathode and keep the cathode hot enough for thermionic emission of electrons. The emission voltage provide negative voltage and govern the electron current produced from the hollow cathode. The discharge power supply offers voltage and current to the anode of the assist ion source to produce the Ar^+ ion beam [3].

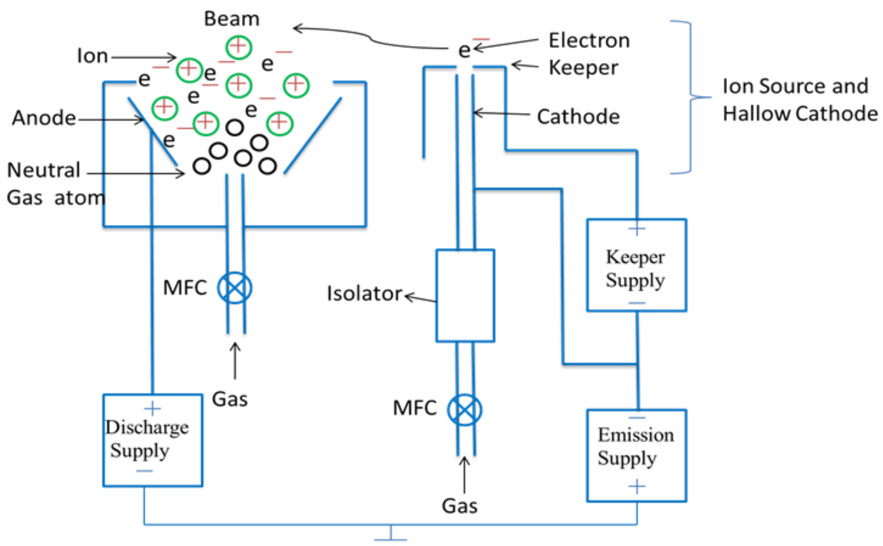

Figure 5.4 *Schematic diagram of assist ion source.*

In this research work, the deposition of CdZnO/ZnO-based MQW is performed by Electtrorava DIBS system [3, 4].

5.2.2 DC Magnetron Sputtering

Sputtering is a technique used to deposit thin films and is classified as physical vapours deposition (PVD) method. Main principle relies on the bombardment of highly energetic ionized gas on the target material causing atoms to sputter off into the plasma. These vaporized atoms are then deposited when they condense as a thin film on the substrate to be coated. DC Sputtering is the most basic and inexpensive type of sputtering for PVD metal deposition and electrically conductive target coating materials. Depending on the working principle and application type there are mainly four types of sputtering techniques are present. These are (1) DC/RF sputtering, (2) magnetron sputtering, (3) reactive sputtering, and (4) ion-beam sputtering. However, currently most complex version of sputtering is DC magnetron sputtering technique and it is used to deposit conducting thin films from a conducting target.

DC magnetron sputtering system consist of following components:

- Main stainless steel chamber
- Load lock chamber
- Robotic arm
- DC power supply
- Substrate holder (anode)
- Heater assembly
- Temperature reader
- Target (magnetron cathode)
- Gas inlets
- Vacuum pump
- Pressure gauge
- Ion gauge
- Water chiller and other parameter controlling unit

A photographic image of DC magnetic sputtering is shown in Figure 5.5. A two inch diameter target is used inside the DC magnetron sputtering gun. Target to substrate distance is also adjustable in order to achieve desired uniformity and deposition rate. The system is equipped with load lock to ensure high vacuum is not disturbed during sample loading into the chamber. The system is pumped with a turbo molecular pump to achieve vacuum of 10^{-6} mbar. The base pressure is monitored by ion gauge and pressure during deposition is monitored by capacitive nanometer. Initially, cleaned substrate is placed into substrate holder. Then, substrate holder is placed face down into the load lock onto the robotic arm. Load lock is pump down and substrate holder is transferred to the column connected to the heater assembly. Robotic arm is withdrawn and gate valve is closed. After that chamber is filled with the high purity inert gas usually argon gas and its flow rate is controlled by mass flow controllers.

Figure 5.5 *Photographic image of the DC magnetron sputtering.*

A DC having high negative potential is applied across the target material i.e. it acts as cathode. A positive supply is applied to the substrate to be coated behaving as anode. The argon gas is first ionized by forceful collision of the gas with the surface of negatively charged target, which ejects atom of the target material into the plasma. Then this plasma with the target material atoms driven to the substrate which is positively charged, therefore attracting the plasma and vaporised target atoms condense and form a thin film coating on the substrate.

DC magnetron sputtering system uses magnet behind the target to trap electrons so that they are not free to hit the substrate and thus allowing higher deposition rates. This also enhances both the efficiency of the initial ionization process and allowing a plasma to be generated at lower pressures which reduces background gas incorporation in the depositing film.

In this thesis work, metal deposition is performed using this technique for the formation of back as well as front contacts on the device.

5.3. Characterization Techniques

The instruments used for the characterization of thin films and MQW structure fabricated in this research work are demonstrated briefly in following sections.

5.3.1 Variable Angle Spectroscopic Ellipsometry Measurement System

Spectroscopic Ellipsometry (SE) is a non-destructive optical technique in which a beam of polarized light is incident on the thin film to be characterized. It has been used to analyze the thickness and optical properties of thin films by determining the variation in polarization of light as it reflects or transmits from thin film [6, 7]. The optical properties i.e. complex refractive index (complex dielectric function) of the any material determine how the light interacts with it. The complex refractive index ($\tilde{n}$) consists of index (n) and extinction coefficient (k):

$$\tilde{n} = n + k \tag{5.1}$$

The change in polarization of the reflected or transmitted light in comparison to incident light is acquired in the form of an amplitude ratio, Psi (Ψ), and the phase difference, (Δ), which depends on optical properties, thickness and roughness of individual materials. Thereafter, a suitable model allows the precise extraction of optical properties, thickness and roughness of thin film.

The polarization of incident light is composed of *p*- and *s*- components (*s*- component is oscillating perpendicular to the plane of incidence and *p*- component is oscillating parallel to the plane of incidence). The amplitude and phase of both *p*- and *s*- polarized component of incident light changes after reflection or transmission from the thin film. The ratio of reflectivity of *p*-polarized light to that of *s*-polarized light gives the change in polarization state, and is given by:

$$\rho = \frac{r_p}{r_s} = \tan\psi \, e^{i\Delta} \qquad (5.2)$$

where r_p and r_s are the amplitude of the *p*- and *s*- polarized component of reflected light normalized to their incident light, respectively, tan(Ψ) represents the ratio of the amplitude and Δ represents the phase difference between *s*- and *p*-polarized light.

The angle of incidence is selected based Brewster angle of the material whose thin film is formed, this is done to ensure a maximal difference in r_p and r_s of the polarized component of reflected light.

Figure 5.6 *Photographic image of Variable Angle Spectroscopic Ellipsometry system.*

The primary components of the ellipsometry system are a light source, polarization generator, sample, polarization analyzer, and detector [6]. In this research work, the thickness and energy bandgap of thin films are measured by M-2000D J. A. Woollam Variable Angle Variable Wavelength Spectroscopic Ellipsometer. In this system, the measurement can be performed at different angles for the wavelength range of 200-1000 nm. The photographic image of Variable Angle Spectroscopic Ellipsometer is shown in Figure 5.6.

5.3.2 Secondary Ion Mass Spectroscopy Measurement System

Secondary Ion Mass Spectroscopy (SIMS) is used for depth profiling of constituents elements in the deposited/ grown structure. Photographic image of the SIMS workstation is given in Figure 5.7. The deposited/grown structure is sputtered with a primary ion beam of O_2^+ or Cs^+ while secondary ions formed of the constituents elements of the deposited/grown films during sputtering are extracted and analysed using a mass spectroscopy.

Figure 5.7 *Photographic image of SIMS system.*

The plot of secondary ions versus time is obtained using this technique, which contains information of depth profiling of constituents elements in the deposited/ grown structure. The time axis can be converted to depth axis by knowing the total thickness of the films deposited assuming the constant sputtering rate. It is a destructive technique since the etching of the deposited/grown materials by sputtering leads to crater in the sample.

In this research work, Hiden SIMS workstation is used for knowing the depth profile of the fabricated MQW structure. It is equipped with two ion guns O_2^+ and Cs^+, both the guns can be operated in the energy range of 0.5 to 5 keV. A quadrupole SIMS analyser provides an opportunity to measure SIMS depth profiles in the mass range 1-1000 amu with a maximum counts up to 107. In this work, O_2^+ of energy 5 eV is used at an incidence angle of 45° with a background pressure of 1 x 10^{-11} mbar. But the working pressure during the SIMS measurement is 1 x 10^{-10} due to inflation of O_2^+ [5].

5.3.3 High-Resolution Transmission Electron Microscopy Measurement System

TEM technique utilizes high energetic electrons to provide compositional, morphological and crystallographic information of the thin film with which the electron interacted and can also provide the interface information if cross sectional TEM is performed. The primary components of the TEM is composed of an electron gun, an objective lens system, a condenser lens system, a magnification system, and the data recording system. In this technique, first the beam of electrons is focused on the thin film by the set of condenser lens and then the beam of electrons after interacting with the thin film is collected by an objective lens system which form the image of the thin film and determines the image resolution limit. Finally, the magnification system magnify the obtained image and projects it on a phosphorous screen or a charge coupled device (CCD) [8].

In TEM, either a thermal emission (CTEM) or field emission (HRTEM) electron gun is used to generate high energy (80-300 keV) electrons which are then accelerated (at a speed of light) and focused by several electromagnet lenses towards an ultra-thin specimen in an ultra-high vacuum column chamber. When these highly energized electrons strikes with the specimen, part of these electrons (elastically scattered electron, inelastically scattered electron, and unscattered electron) are transmitted through the specimen depending on the specimen thickness and density. Then, the transmitted unscattered electrons are focused by the objective lens onto a phosphor screen or CCD camera to produce the image of the internal structure of the crystal. Figure 5.8 illustrates the schematic of working principle of the TEM operation.

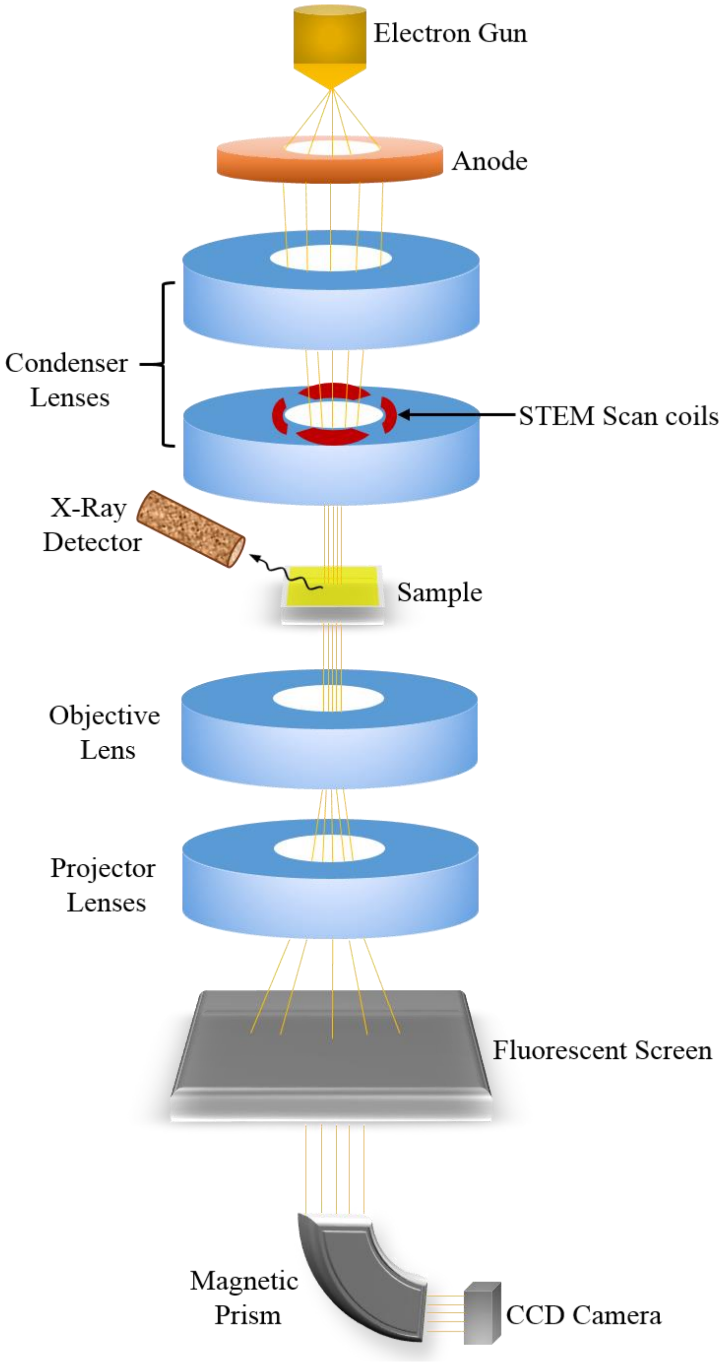

Figure 5.8 *Schematic of the TEM working principle.*

Figure 5.9 *Photographic image of HRTEM system.*

High-resolution transmission electron microscopy (HRTEM) gives structural information at the atomic size level, and therefore become very significant for interface analysis by performing cross-sectional HRTEM. The photographic image of HRTEM is shown in Figure 5.9. The resolution in phase contrast HRTEM is 0.05 nm and therefore individual atoms of a crystal and its defects can be resolved. The interface studies of oxide-semiconductor, metal-semiconductor, and semiconductor-semiconductor can be performed from HRTEM. In HRTEM, an interference image of the thin film under measurement is created using both the transmitted as well as the scattered electrons beams. As, phase contrast image is obtained, therefore, its size can be as small as the unit cell of the crystal. In this case, during propagation of modulated electron waves through the objective lens they interfere with themself at very low angles. All electrons that emerges from the thin films are combined at a point in the image plane. HRTEM has been widely used for investigating the crystal structures and lattice imperfections in the deposited/grown thin films with the resolution of an atomic scale. It can also be used for the getting the information of point defects, dislocations, stacking faults, surface structures and precipitates grain boundaries [8].

In this research work, the quality of interfaces in CdZnO/ZnO-based MQW structure are studied by cross-sectional HRTEM using HRTEM: JEOL JEM-2010 operated at 200 kV [5].

5.3.4 Energy-dispersive X-Ray Spectroscopy

Energy Dispersive X-Ray Spectroscopy (EDS or EDX) is a chemical microanalysis technique used in conjunction with scanning electron microscopy (SEM). The actual image of this EDX system is shown in Figure 5.10. The EDX technique detects X-Rays emitted from the sample during the bombardment by an electron beam to characterize the elemental composition of the analyzed volume. Features or phases as small as 1 µm or less can be analyzed [9].

Figure 5.10 *Photographic image of FESEM and EDX, Zeiss Supra 55.*

When the sample is bombarded by the SEM's electron beam, electrons are ejected from the atoms comprising the sample's surface. The resulting electron vacancies are filled by electrons from a higher state, and an X-Ray is emitted to balance the energy difference between the two electrons' states. The X-Ray energy is characteristic of the element from which it has been emitted.

The EDX X-Ray detector measures the relative abundance of emitted X-Rays versus their energy. The detector is typically lithium-drifted silicon, solid-state device. When an incident X-Ray strikes the detector, it creates a charge pulse that is proportional to the energy of the X-Ray. The charge pulse is converted to a voltage pulse (which remains proportional to the X-Ray energy) by a charge-sensitive preamplifier. The signal is then sent to a multichannel analyzer where the pulses are sorted by voltage. The energy, as determined by the voltage measurement, for each incident X-Ray is sent to a computer for display and further data evaluation. The spectrum of X-Ray energy versus counts is evaluated to determine the elemental composition of the sampled volume. Quantitative results can be obtained from the relative X-Ray counts at the characteristic energy levels for the sample constituents [9].

In this research work, the composition of different elements in CDZnO/ZnO-based MQW structure is characterized using energy dispersive X-Ray (EDX, Zeiss Supra 55).

5.3.5 Field Emission Scanning Electron Microscopy

Field emission scanning electron microscope (FESEM) is commonly used for analyzing morphological properties of the sample under observation. Figure 5.10 show the actual image of this FESEM system. FESEM is considered as a very powerful microscopic technique which provides 100000 times magnified image of the sample [10]. The FESEM mainly involves four components: (a) an electron source known as electron gun, (b) an electron condenser lens which controls the size of the electron beam, (c) XY defection coils to move the electron beam in a controlled fashion, and (d) the electron detectors. All components are fixed in a chamber, and this whole chamber is kept under ultra-high vacuum conditions. In FESEM system, a different type of electron source called Field Emission Gun is used for very high magnification. In this system, the source is not heated by the current; instead, an electric field is used to obtain the electrons from the source, which is a very sharp tungsten crystal or zirconium oxide. Here, the electrons have energy in the range of 1-40 KeV [10].

When the electron beam falls on the sample, it interacts with the atoms and the electron is slowed down due to strong elastic scattering. The atoms absorb the energy and get ionized. Some of the electrons from the sample atoms are released. These are called 'secondary electrons'. They usually have lower energy (< 50 eV) compared to the primary electrons from the electron gun. When the electron beam falls on the surface of sample, the electrons are scattered, and the beam diameter increases. Hence, in the beginning, it spreads like a cone and the area below the surface also is probed. The beam energy decreases as it goes deeper inside the sample. The number of secondary electrons produced also decreases. Besides, the electrons from the surface easily escape and arrive at the detector. The electrons from the bottom may be captured by other atoms before they escape to the surface. Hence only fewer secondary electrons from the trough come to the detector. Overall, the secondary electrons at the detector are essentially produced at the top of the surface. These secondary electrons are used to present the morphology and topography of the sample. The detector of instruments count the number of e-interactions and display to the screen whose intensity is determined by this number, producing the FESEM image [10, 11].

A ZEISS Supra55 FESEM system was used to observe the surface morphologies of the CdZnO thin films.

5.3.6 X-Ray Diffraction Measurement

X-Ray diffraction (XRD) is an important technique to examine the crystallinity, phase, strain, and preferred orientation, etc. of samples [12]. A collimated beam of X-Rays is incident on a sample and diffracted by the crystalline phases in the sample according to Bragg's law such that:

$$n\lambda = 2d \sin\theta \tag{5.3}$$

Where λ is the wavelength of the incident X-Ray beam, d is the inter-plane separation of lattice between atomic planes in the crystalline phase, θ is the angle between atomic planes and the incident X-Rays beam. Where n is an integer that represents the interference order.

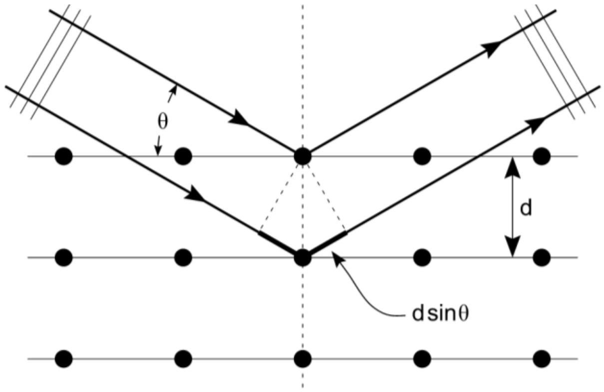

Figure 5.11 *Basic principle of XRD diffraction.*

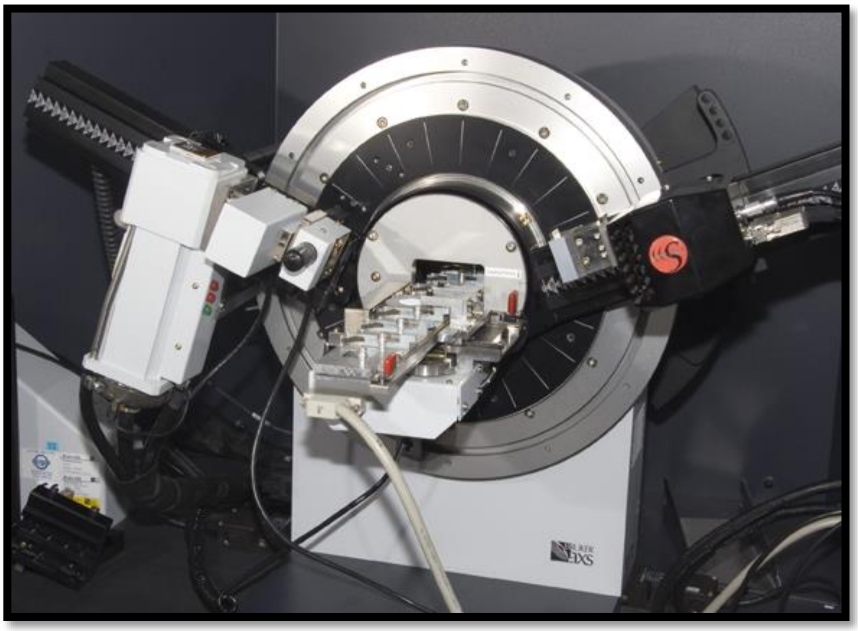

Figure 5.12 *Photographic image of Bruker D8 Advance X-rays diffractometer.*

The intensity of the diffracted X-Rays is measured as a function of the diffraction angle 2θ. This diffraction pattern is used to identify the sample crystal orientation [12]. It is well known that atoms of a pure solid are arranged in a regular periodic pattern called 'lattice.' The inter-atomic distance and interaction of atoms in any crystalline lattice is unique and results in a unique XRD pattern to identify its crystal structure. The XRD patterns include peak position and intensity of the diffracted beam, which provides a variety of information about the samples.

In this research work, the crystal structure of CdZnO thin films are characterized using Rigaku SmartLab, Automated Multipurpose X-Ray Diffractometer equipped with a copper target (Cu-Kα) to generate the incident X-Rays of wavelength λ = 0.154178 nm for the diffraction measurement in Bragg Brentano configuration. The actual image of this XRD system is shown in Figure 5.12.

5.3.7 Solar Cell Testers system

Solar cell tester is basically an integrated system combining solar simulator and *I-V* measurement system. The photographic image of the solar tester is shown in Figure 5.13. The various units of the solar cell tester are briefly explained here:

(a) Sample Placement and Connection Stage: Sample is placed on the chuck shown in the Figure 5.13. And thereafter connection to the solar cell under measurement is made with the help of adjustable pins. The sample placed on the chuck is hold on to it tightly by switching on the vacuum button.

(b) Temperature and Vacuum Controller Unit: As operation temperature has significant impact on the solar cell performance, therefore its analysis is very important. And this system provide the facility of varying the temperature of the device under measurement. The sample placed on the chuck is hold on to it tightly by switching on the vacuum button.

(c) Intensity Controller Unit: As in real-world applications, the SCs are operated in non-STC, i.e., solar irradiance level varies with geographical location, weather conditions, and time in a day, analysis of solar cell under different solar irradiance is of utmost important and can be performed in the solar simulator.

(d) Measurement System: Keithley is used for measuring *I-V* Characteristics of the Cell in dark and light condition.

Figure 5.13 *Photographic image of Solar cell tester system.*

Some of the salient features of the Solar cell testers are [13]:

(a) Fully integrated and automated system with computer control.

(b) Light intensity measurement and feedback control for stability.

(c) Flexible cell test fixture configurations, including optional cell temperature control (10°C to 70°C ±0.5°C or better).

(d) True four-probe cell contacting technique.

(e) Temperature controlled chuck with vacuum hold.

(f) Intensity measurement and temperature measurement with the ability to normalize the data points to Standard Test Conditions (STC) or other user specified conditions.

(g) Advanced *I-V* curve software, including powerful curve fitting algorithms, with 3 different curve fitting models and 17 different weight function models.

(h) Ability to determine Thermal Coefficients of various cell parameters.

Some of the technical specifications of solar cell tester are listed in Table 5.1.

Table 5.1: *Technical specifications of solar cell tester*

Feature description	**Specification**
Type of lamp	Xenon Short Arc
Lamp Power	150 W

Max. Illuminated area	2” (50 mm) x 2” (50 mm)
Air Mass	AM1.5G Standard: AM1.5D or AM1 optional
Adjustment Range of light intensity	100 mW/cm^2 +/- 15%
Spectral Range	350 nm - >2,700 nm
Spatial Non-uniformity of irradiance*	≤ 2% or better
Degree of Collimation	≤ 2 degrees
Phase/Voltage/Frequency	Single Phase/110-220 AC Volts /50-60 Hz
Max. Power Consumption (W)	0.5 KVA

A solar cell tester is the instrument which is used to measure *I-V* and *P-V* characteristic of the solar cell under dark and illuminated condition. From these characteristics obtained, it directly provides the performance parameters such as short-circuit current, open-circuit voltage, fill factor, maximum peak power, voltage and current corresponding to maximum power, shunt and series resistance and conversion efficiency. In this system, various AM filters can be used to measure solar cell performance for different applications.

5.4. References

[1] V. Garg, B. S. Sengar, V. Awasthi, and P. Sharma, “RSC Advances Localized surface plasmon resonance on Au nanoparticles : tuning and exploitation for performance enhancement in ultrathin photovoltaics,” RSC Advances, vol. 6, pp. 26216-26226, 2016.

[2] H. R. Kaufman, R. S. Robinson, and R. I. Seddon, “End-Hall ion source,” Journal of Vacuum Science & Technology A: Vacuum, Surfaces, and Films, vol. 5, no. 4, pp. 2081-2084, 1987.

[3] F. Quaranta, A. Valentini, F. R. Rizzi, and G. Casamassima, “Dual-ion-beam sputter deposition of ZnO films,” Journal of Applied

Physics, vol. 74, no. 1, pp. 244-248, 1993.

[4] V. Awasthi, S. K. Pandey, S. Kumar, C. Mukherjee, M. Gupta, and S. Mukherjee, “Evaluation of the band alignment and valence plasmonic features of a DIBS grown Ga-doped $Mg_{0.05}Zn_{0.95}O$/CIGSe heterojunction by photoelectron spectroscopy,” Journal of Physics D: Applied Physics, vol. 48, no. 48, p. 485305, 2015.

[5] G. Siddharth, R. Singh, V. Garg, B. S. Sengar, M. Das, B. Mandal, M. T. Htay, M. Gupta, and S. Mukherjee, “Investigation of DIBS-Deposited CdZnO/ZnO-Based Multiple Quantum Well for Large-Area Photovoltaic Application,” IEEE Transactions on Electron Devices, vol. 67, no. 12, pp.5587-5592, 2020.

[6] L. Arsov, M. Ramasubramanian, and B. N. Popov, “Ellipsometry,” Characterization of Materials, Hoboken, NJ, USA: John Wiley & Sons, Incorporation, pp. 1-11, 2012.

[7] P. Sharma, Aaryashree, V. Garg, and S. Mukherjee, “Optoelectronic properties of phosphorus doped p-type ZnO films grown by dual ion beam sputtering,” Journal of Applied Physics, vol. 121, no. 22, p. 225306, 2017.

[8] J. M. Howe, B. Fultz, and S. Miao, “Transmission Electron Microscopy,” Characterization of Materials, Hoboken, NJ, USA: John Wiley & Sons, Incorporation, pp. 1-46, 2012.

[9] S. T. D. Ellingham, T. J. U. Thompson, and M. Islam, “Scanning Electron Microscopy-Energy-Dispersive X-Ray (SEM/EDX): A Rapid Diagnostic Tool to Aid the Identification of Burnt Bone and Contested Cremains,” Journal of forensic sciences, vol. 63, no. 2, pp. 504-510, 2018.

[10] L. Reimer, “Scanning Electron Microscopy: Physics of Image Formation and Microanalysis, Second Edition,” Measurement Science and Technology, vol. 11, no. 12, pp. 1826-1826, 2000.

[11] B. Bhushan and O. Marti, “Scanning Probe Microscopy-Principle of Operation, Instrumentation, and Probes,” Springer Handbook of

Nanotechnology, Berlin, Heidelberg: Springer Berlin Heidelberg, pp. 573–617, 2010.

[12] H. Kim, C. M. Gilmore, A. Piqué, J. S. Horwitz, H. Mattoussi, H. Murata, Z. H. Kafafi, and D. B. Chrisey, “Electrical, optical, and structural properties of indium–tin–oxide thin films for organic light-emitting devices,” Journal of Applied Physics, vol. 86, no. 11, pp. 6451-6461, 1999.

[13] “Solar Cell Testers: Photo Emission Technology,” [Online]. Available: http://www.photoemission.com/celltesters.html.

Chapter 6

Analysis of DIBS deposited MQW for photovoltaic application

6.1. Introduction

The multiple quantum wells (MQWs) structures have gained significant interest for their potential applications in optoelectronic devices such as photodetector, light emitting diode, and photovoltaic [1-3]. It is because MQW based devices have greater thermal stability as compared to that of conventional devices, as they are driven by thermally activated carriers escaped from quantum wells and is commonly termed as carrier transport mechanism [4]. MQWs insertion in the *p-i-n* solar cell (SC) leads to the enrichment of the performance parameters by independently controlling and optimizing both the current and voltage performance parameters. The devices containing MQW structure in an active region demands for high depth resolution to resolve the individual barrier and well layers. For this reason, secondary ion mass spectrometry (SIMS) is widely used for measuring constituent elements profiles in deposited structure [5].

The ZnO-based semiconductors recently got much attention due to its wide range of optoelectronic, energy, and photovoltaic applications because of its wide bandgap, large excitonic binding energy, high breakdown strength etc. [2, 6-9]. Our group has effectively established dual ion beam sputtering (DIBS)-grown CdZnO/ZnO MQWs for light emitting diode (LED) [2] and MgZnO/CdZnO potential well for heterostructure field effect transistor (HFET) application displaying strong two-dimensional electron gas density (2DEG) [10, 11]. CdZnO as a material offers a pronounced prospect in photovoltaic devices because it covers ultraviolet-visible region of the solar spectrum as its energy bandgap can be varied from 2.2 to 3.37 eV [2] by manoeuvring Cd/Zn ratio. However, till date, there are no reports in the literature on the experimental implementation of CdZnO/ZnO-based MQWs for photovoltaic application.

In the present study, the DIBS system is used for the deposition of CdZnO/ZnO-based MQWs by using a single target of CdZnO and ZnO each during film deposition process. For the first time, the CdZnO/ZnO-based MQWs are fabricated by using DIBS system. The DIBS system is incredible when it comes to realize high-quality thin films with precise element composition and outstanding uniformity throughout the substrate and superior film adhesion to the substrate. Apart from this, other perceptible features of the DIBS system are diminished surface roughness and the provision of in-situ pre-cleaning of substrates prior to film deposition using assist ion source [12]. In DIBS system, the temperature of the substrate can be varied from room temperature to 1000 °C and the ambience of the film deposition can also be varied, so that quality deposition of thin films can be achieved of various materials. The DIBS system also offers advantage of uniform deposition on a large area, and thus, it can be helpful in realization of large area photovoltaic cell. The MQW structures are examined using the SIMS and high-resolution transmission electron microscopy (HRTEM) techniques to investigate its depth profile at high resolution and collect the information on elements inter-diffusion. This work explore into the possibility of developing CdZnO/ZnO-based MQWs structure, that can be further utilized in the solar cell application to improve the performance parameters associated with it.

6.2. Experimental

The CdZnO/ZnO-based MQW structure is deposited on silicon substrates using the DIBS system attached with radio frequency (RF) primary ion source. In addition to the primary ion source, the DIBS system also consists of a direct-current coupled (DC) assist ion source to reduce columnar growth and thereby boost film adhesion and deposition uniformity. Prior to the MQW deposition process, the substrates (1.2×1.2 cm^2) are ultrasonically cleaned in trichloroethane, acetone, isopropanol, and deionized water successively for 15 min each, in order to remove the adventitious dust particles and organic contaminations. The substrates are then purged with the nitrogen gas (5-N-purity). After placing the substrates into the DIBS chamber, pre-cleaning is performed by Ar^+ ion bombardment using assist ion source for 10 min. to further clean the substrate to remove any kind of native oxide formation over Si before the deposition of the device.

A schematic representation of the fabricated MQW structure is depicted in Figure 6.1. The film deposition is carried out using a 4-N-pure and 4-inch-diameter 15 at.% Cd-doped ZnO and ZnO targets mounted on water-cooled target holder inside the DIBS system chamber [13]. The background pressure inside the process chamber is maintained at 1×10^{-8} mbar while the working pressure during film deposition is 1×10^{-4} mbar. The discharge voltage and current of the assist ion source are kept constant at 70 V and 600 mA, respectively, with 5 sccm of Ar flow rate at the film deposition time.

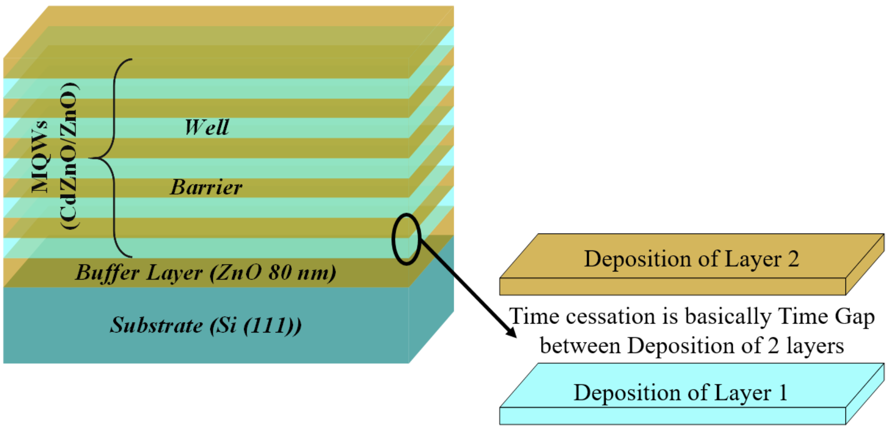

Figure 6.1 *Schematic of MQW structure.*

For the optimization of the films, different deposition conditions are used and the steps followed are as follows:

Step 1: Beam power of RF ion source is varied: (a) 44 W (b) 14 W, represented by B4 and B1, respectively.

Step 2: Substrate temperatures 100, 200, and 300 ˚C are used during deposition and they are represented by T1, T2, and T3, respectively.

Step 3: Barrier layer thickness values of 15, 20, 25, and 30 nm are used and they are represented by L15, L20, L25, and L30, respectively.

Step 4: Time cessations of 2, 30, and 45 min are used between the depositions of successive layers and they are represented by C2, C30, and C45, respectively.

As per the above steps of optimization, 9 different samples of MQWs structure are fabricated and represented as shown in the Table 6.1.

Table 6.1: *Samples representation*

Sample No.	Represented by	Sample No.	Represented by
1	B4T3L15C2	6	B1T1L20C30
2	B1T3L15C2	7	B1T1L25C30
3	B1T2L15C2	8	B1T1L30C30
4	B1T1L15C2	9	B1T1L20C45
5	B1T1L15C30		

Table 6.2: *Samples deposition condition used for SIMS and HRTEM analysis*

Sample No.	Deposition Conditions			
	Beam Power (W)	Substrate Temperature (˚C)	Time cessation (min)	Barrier layer thickness (nm)
1	44	300	2	15
2-4	14	300, 200, 100	2	15
5-8	14	100	30	15, 20, 25, 30
9	14	100	45	20

In Table 6.2, the deposition conditions are listed for the samples represented in Table 6.1. From Figure 6.1, it can be seen that a buffer layer of ZnO material is deposited on silicon substrate before the actual fabrication of the MQWs structure. This is just introduced to reduce the lattice strain and stress on the MQWs structure due to lattice mismatch between silicon and ZnO. The thickness of buffer layer (80 nm) and well layer (10 nm) is kept constant for all the samples. Before actual fabrication of the MQW structure, the individual film deposition rates are assessed from the thickness determination by spectroscopy ellipsometry (SE).

The crystalline phase and crystal orientations of CdZnO thin films are determined by X-Ray diffraction (XRD) using Rigaku Smart Lab system with Cu-Kα radiation (λ = 1.54 Å). And the morphology of the thin films is examined using the field emission scanning electron microscope (FESEM, Zeiss Supra 55). Following the MQW structure fabrication, the element depth profiling of the samples is carried out by Hiden SIMS workstation. The oxygen ion gun of energy 5 keV is used at an incidence angle of 45˚, with a background pressure of 1×10^{-11} mbar. The working pressure during SIMS measurements is $\sim1\times10^{-10}$ mbar due to inflating of oxygen gas. Further, the samples are studied by cross-sectional HRTEM using HRTEM: JEOL JEM-2010 operated at 200 kV. To calculate the energy band of the CdZnO and ZnO thin films and also to determine the deposition rate of the thin films, a SE instrument is used, provided by J.A. Woolam Co. Inc.

6.3. Results and discussion

6.3.1 Structural and Morphological properties

Most of the characterization of the individual thin-films involved in MQW structure formation i.e. CdZnO and ZnO has been already performed in our earlier work [13-15]. Here, structural and morphological studies are carried out for the CdZnO thin film.

XRD patterns of CdZnO thin films deposited at various substrate temperature are depicted in Figure 6.2. From the figure, the diffraction peaks of all the thin films can be indexed to c-axis (002) lattice plane at 2θ value of 34º, which is associated with hexagonal wurtzite structure. No other peaks except that of silicon (100) at 2θ value of 69º is identified in the XRD measurement, which is used as substrate for the thin film deposition. As substrate temperature is decreased from 300 to 100 °C, the diffraction peak intensity of (002) peak increased consistently with the reduction of full width half maximum (FWHM) as shown in Table 6.3, indicating an improvement of (002) crystal orientation. As, can be seen with increasing temperature, the peak intensity as well as crystallite size reduces, therefore no further increase in temperature above 300°C is performed for film deposition. However, substrate temperature is neither decreased below 100 °C, so as not degrade the adhesion of the thin film with substrate.

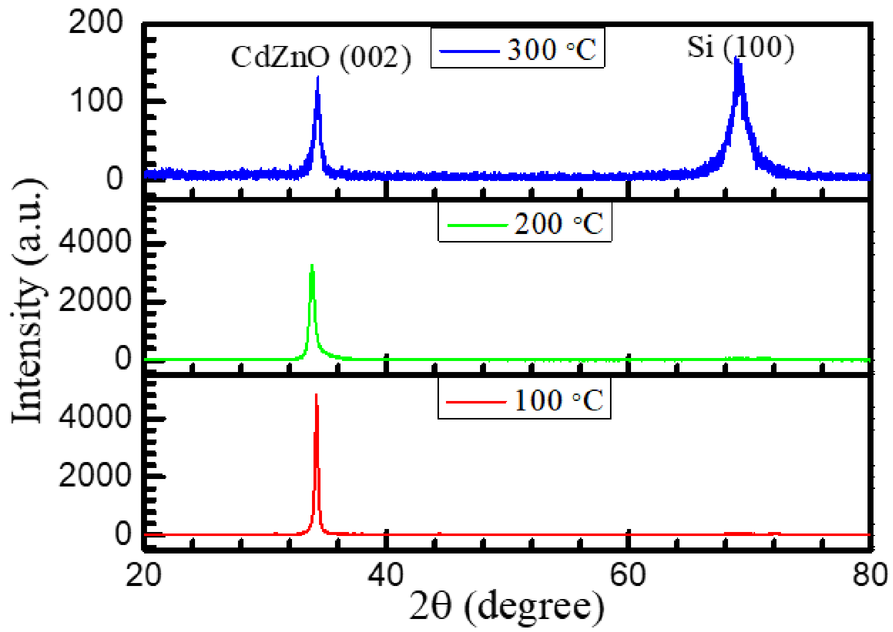

Figure 6.2 *XRD pattern of CdZnO thin films deposited at various substrate temperature.*

Table 6.3: *FWHM and Crystallite size of CdZnO thin films deposited at various substrate temperature*

Substrate Temperature (°C)	**100**	**200**	**300**
FWHM (degree)	0.29	0.47	0.51
Crystallite Size (nm)	33.11	20.34	18.86

The crystallite size (D) in these films can be evaluated using Scherrer's formula [16]:

$$D = \frac{k * \lambda}{FWHM * \cos\theta} \tag{6.1}$$

where k is Scherrer's constant, λ is X-ray wavelength, and θ is the corresponding Bragg's diffraction angle. The crystallite size is observed to decrease from 33.11 to 18.86 nm with increasing substrate temperature from 100 to 300 °C, as can be seen from Table 6.3. The increase in substrate temperature results in the breaking of CdZnO bonds and consequent re-sputtering of the deposited film rather than enabling the atoms to move to their stable lattice sites, producing defects in the film, and thus leading to degradation in the crystalline property. CdZnO grown at 300 °C has a very poor crystal quality, in comparison to other films, with the lowest (002) peak intensity with a very high value of FWHM (0.51°) and the corresponding crystallite size of 18.86 nm. Hence, from the above investigation it is observed with increasing temperature, the peak intensity as well as crystallite size reduces, therefore no further increase in temperature above 300°C is performed for film deposition. However, substrate temperature is neither decreased below 100 °C, so as not degrade the adhesion of the thin film with substrate.

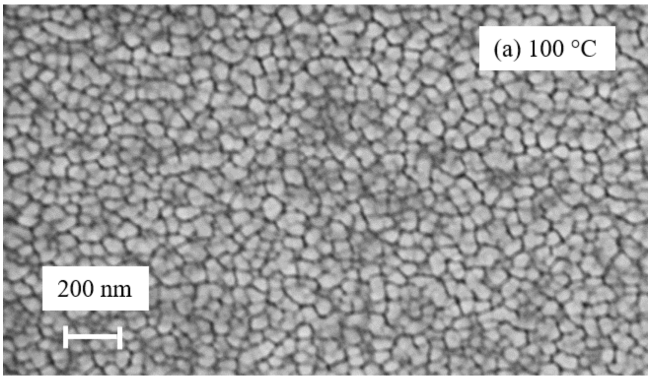

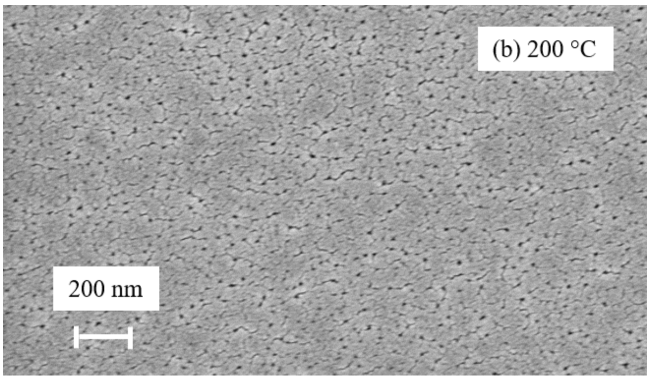

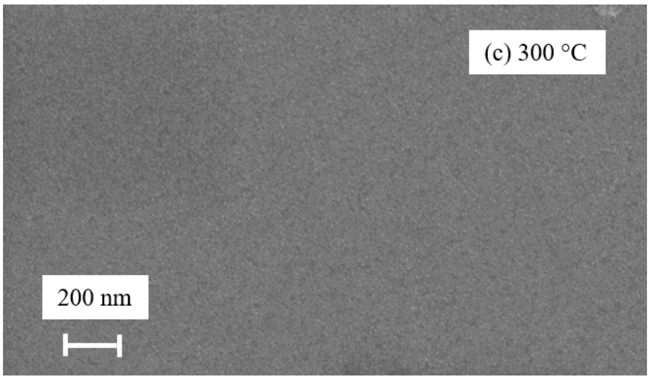

Figure 6.3 *FESEM images of surfaces of CdZnO thin films at various substrate temperatures.*

Figure 6.3 show FESEM micrographs of CdZnO thin films deposited at various substrate temperature. As substrate temperature increases, there is a noticeable decrement in the morphology and dimension of grains. The grains at 100 °C are found to be distinct, uniform and larger as compared to that of other higher substrate temperature. At 300 °C, grains are not distinctly visible at specified 200 nm scale of FESEM. A larger value of grain size may be advantageous depending on the electronic structure of the grain boundaries. The large grain size maximizes the minority carrier diffusion length in thin film. Therefore, 100 °C substrate temperature can be considered to be the optimum temperature to deposit uniform CdZnO crystal with the large grains.

6.3.2 Spectroscopy ellipsometry analysis

SE is a non-destructive technique used to obtain optical parameters of the materials [17]. The experimentally obtained SE data in terms of two standard ellipsometric angles psi (ψ) and delta (Δ), has been theoretically fitted with a three-layer optical model involving a top surface roughness layer, a CdZnO (or ZnO) layer, and a Si substrate using the complete ease software provided by J.A. Woolam Co. Inc. [18-19]. In the three-layer model, General Oscillator (GenOsc) model comprising of Gaussian oscillator is utilized to acquire theoretical spectra by fitting GenOsc parameters. The acquired theoretical spectra and experimental data are in acceptable concurrence, with low value of mean square error (MSE) of 8.91 and 8.98 for ZnO and CdZnO layers, respectively. The variation of $(\alpha h\nu)^2$ vs. hν for CdZnO and ZnO obtained from the theoretical spectra is shown in Figure 6.4. As can be seen from Figure 6.4, the energy bandgap values of CdZnO and ZnO thin films are 3.19 (± 0.03) and 3.37 (± 0.03) eV, respectively, as obtained by the linear extrapolation method. The thickness of the individual film deposited is also available from the theoretical spectra, from which the film's deposition rate is obtained and further used to deposit the film of required thickness.

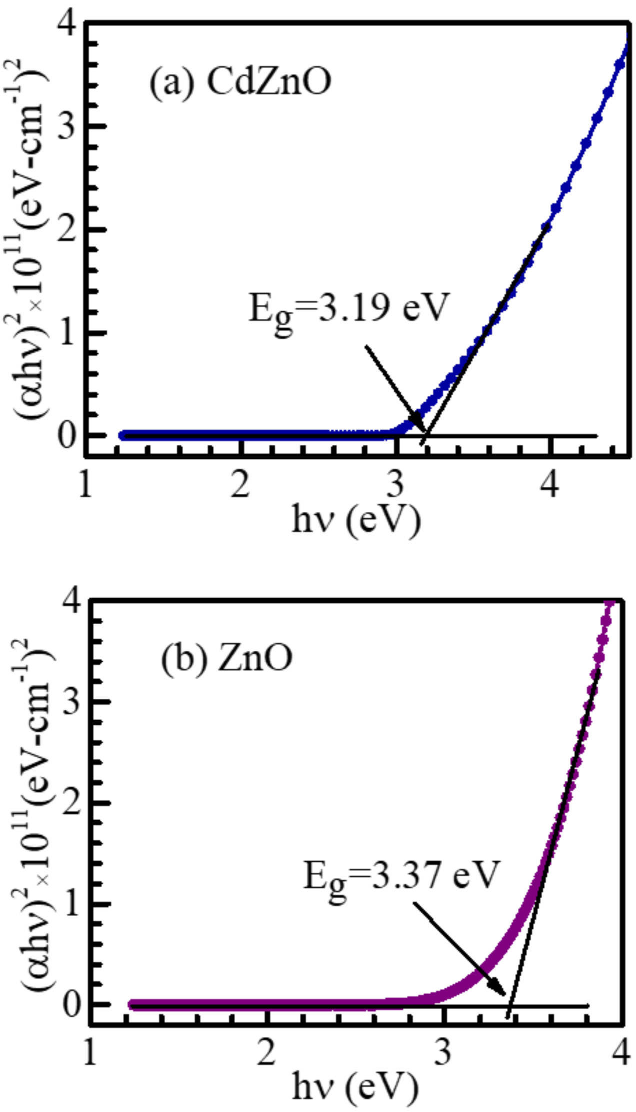

Figure 6.4 *Tauc plot of (a) CdZnO and (b) ZnO thin films.*

6.3.3 SIMS Analysis

The depth profile of the MQWs structure is probed by SIMS measurement with the primary ion beam of O_2^+ and the obtained depth profiles of constituent elements such as Cd and Zn in the well and barrier materials are shown in Figure 6.5 (a)-(i). The two stable isotopes of Cd present in the analysis are Cd 111 and Cd 106. As can be seen from Figure 6.5, oxygen (O) is absent because O_2^+ is used as the primary ion beam source.

The result of SIMS analysis of sample 1 (B4T3L15C2) is shown in Figure 6.5 (a). It is clear that Cd diffuses into all the layers and thus quantum wells are not formed. The reason of the diffusion is probably the high ion beam power deployed during film deposition.

Thereafter, the deposition of samples 2-9 is performed as per the B1 condition mentioned in Step 1 and improved results are obtained in terms of diffusion although the deposition rate is drastically reduced, by 3 times (from 1 to 0.33 nm/min), compared to deposition at B4 condition because of the kinetic energy reduction. Now, the analysis is performed concerning the deposition of thin films at different substrate temperatures (Step 2). From Figure 6.5 (b)-(d), it is clear that the deposition performed at T1 (i.e. sample B1T1L15C2) provides the best results in terms of the quantum well and barrier layer formation, as compared to T2 and T3 counterparts. The substrate temperature increase leads to the increase in Cd diffusion in all the layers and similar behavior has also been reported by Carlson *et al.* [20]. As expected, the Zn is found to be uniform throughout the deposited MQW structure because Zn is present in both well and barrier layers at high content.

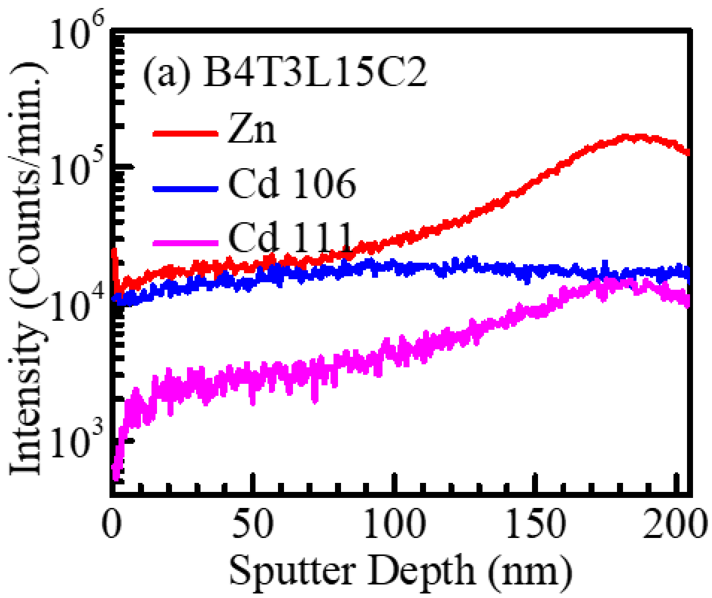

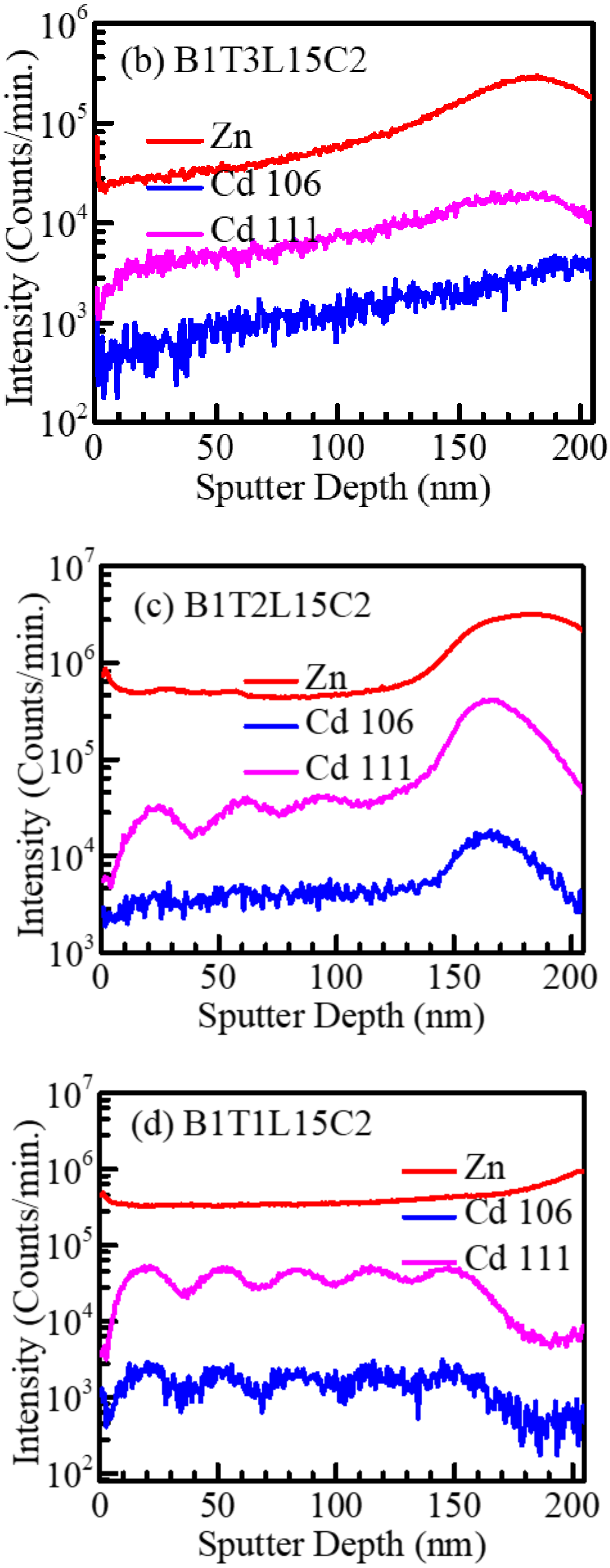
(b) B1T3L15C2
Zn
Cd 106
Cd 111
Intensity (Counts/min.)
Sputter Depth (nm)
(c) B1T2L15C2
Zn
Cd 106
Cd 111
Intensity (Counts/min.)
Sputter Depth (nm)
(d) B1T1L15C2
Zn
Cd 106
Cd 111
Intensity (Counts/min.)
Sputter Depth (nm)

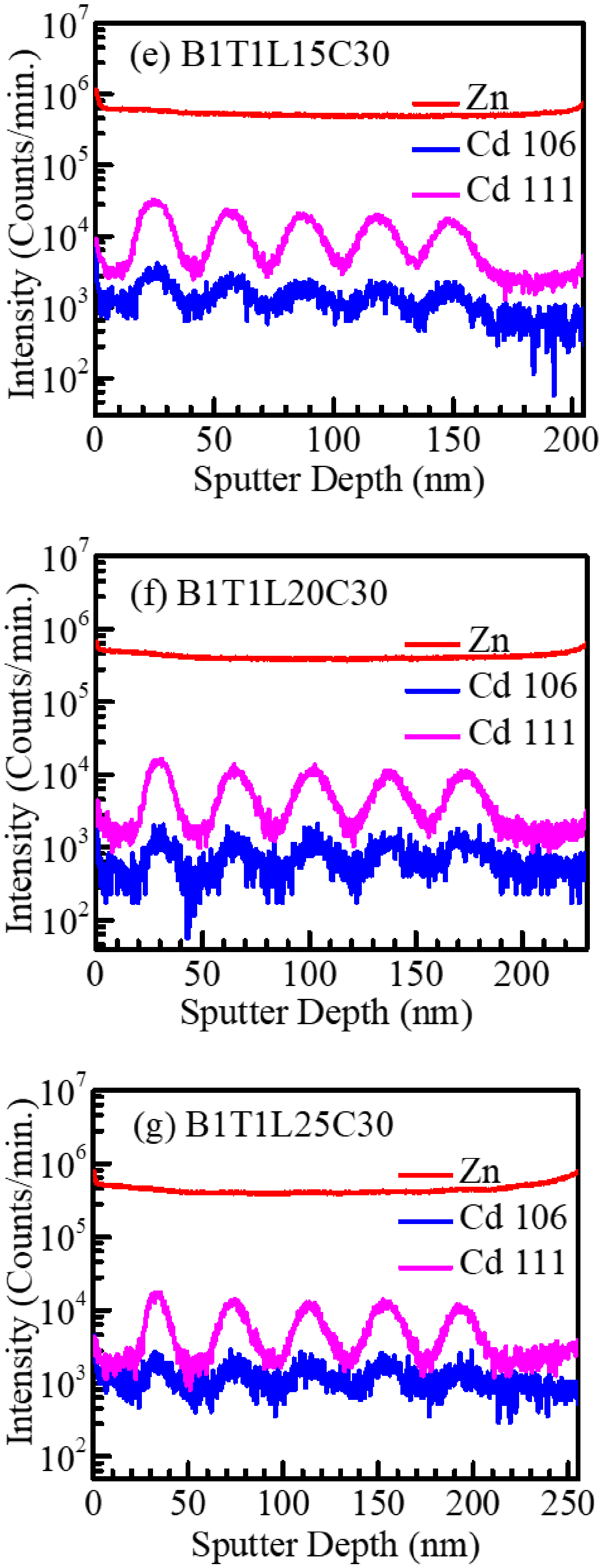
(e) B1T1L15C30
Zn
Cd 106
Cd 111
Intensity (Counts/min.)
Sputter Depth (nm)
(f) B1T1L20C30
Zn
Cd 106
Cd 111
Intensity (Counts/min.)
Sputter Depth (nm)
(g) B1T1L25C30
Zn
Cd 106
Cd 111
Intensity (Counts/min.)
Sputter Depth (nm)

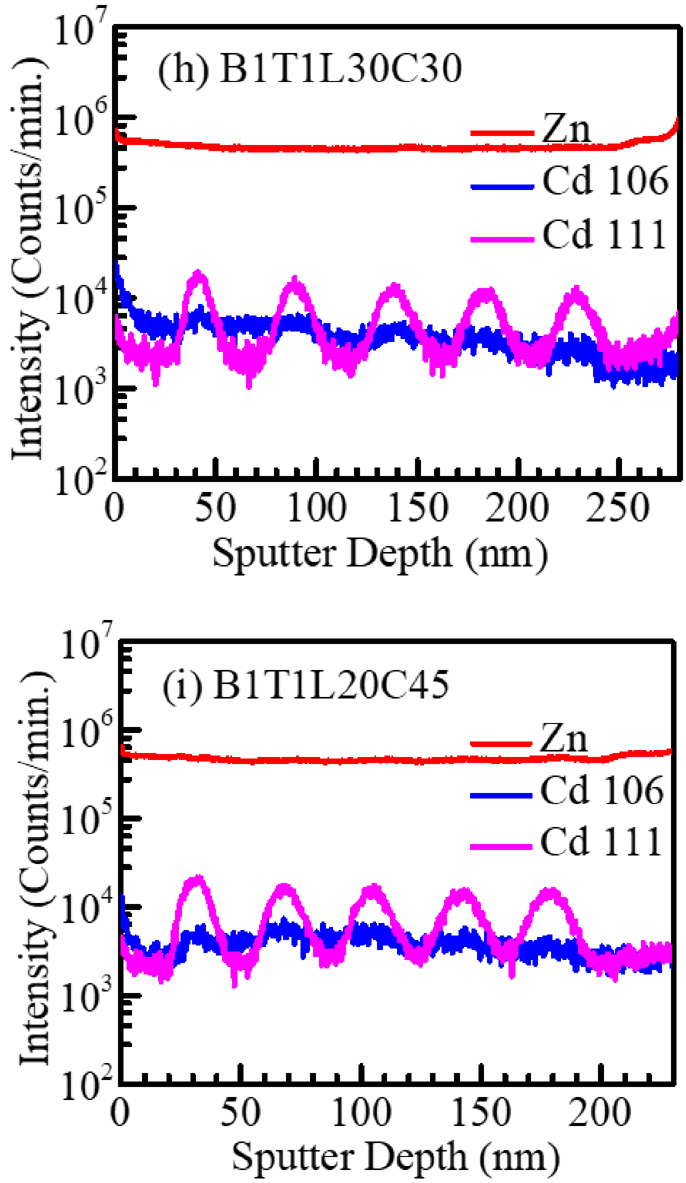

Figure 6.5 *SIMS profile of CdZnO/ZnO-based MWQs deposited at (a) B4 and T3 condition; (b)-(d) B1 condition and at different substrate temperature T3, T2 and T1 respectively; (e)-(h) B1, T1 and C30 condition, but variable barrier thickness L15, L20, L25 and L30 respectively; and (i) same condition as that of (f) but at different time cessation, C45.*

Subsequently, the substrate temperature of all the samples is fixed at T1 with a constant well thickness of 10 nm, however, the barrier layers thickness is varied as specified in the Step 3 and displayed in Figure 6.5 (e)-(h). Also, the time cessation between the deposition of successive layers in the samples 5-8 is 30 min compared to 2 min used in the samples 1-4, as represented in Figure 6.5 (a)-(d). The well and barrier formation are quite good as the peaks of Cd in the well region and its absence in the barrier region are clearly visible, and it is due the time cessation increase from C2 to C30. However, no noticeable impact is observed as the time cessation is increased from C30 to C45. The related SIMS profile of sample 9 (B1T1L20C45) is shown in Figure 6.5 (i), indicating that C30 is an optimal cessation time.

6.3.4 Cross-sectional HRTEM analysis

In the HRTEM image of sample 7 (B1T1L25C30), as shown in Figure 6.6 (a), it is observed that MQW periodicity and the layer interfaces are not distinct and appear like a single layer. This might be due to the small lattice mismatch of ~2% (as estimated from the data given in Ref. [21]) between the well and barrier layers. However, a much faded interface is visible separating the buffer layer from the MQW structure, as shown by the magnified version of the HRTEM image in the same Figure. The total thickness of sample 7, as calculated from TEM image is 252 nm, which is approximately the same as expected from the deposited rate. To confirm the formation of QWs, the SIMS analysis is also performed on this sample, as shown in the Figure 6.6 (b). It clearly indicates the periodic appearance of Cd humps, indicating the formation of CdZnO well layer. From a much higher resolution image of sample 6 (B1T1L20C30), as shown in Figure 6.6 (c), the interface between the well and barrier layers can be visualized, indicating the formation of well and barrier regions.

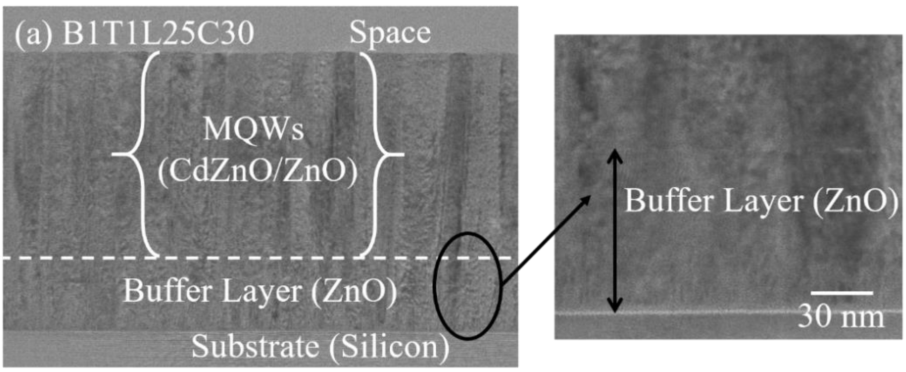

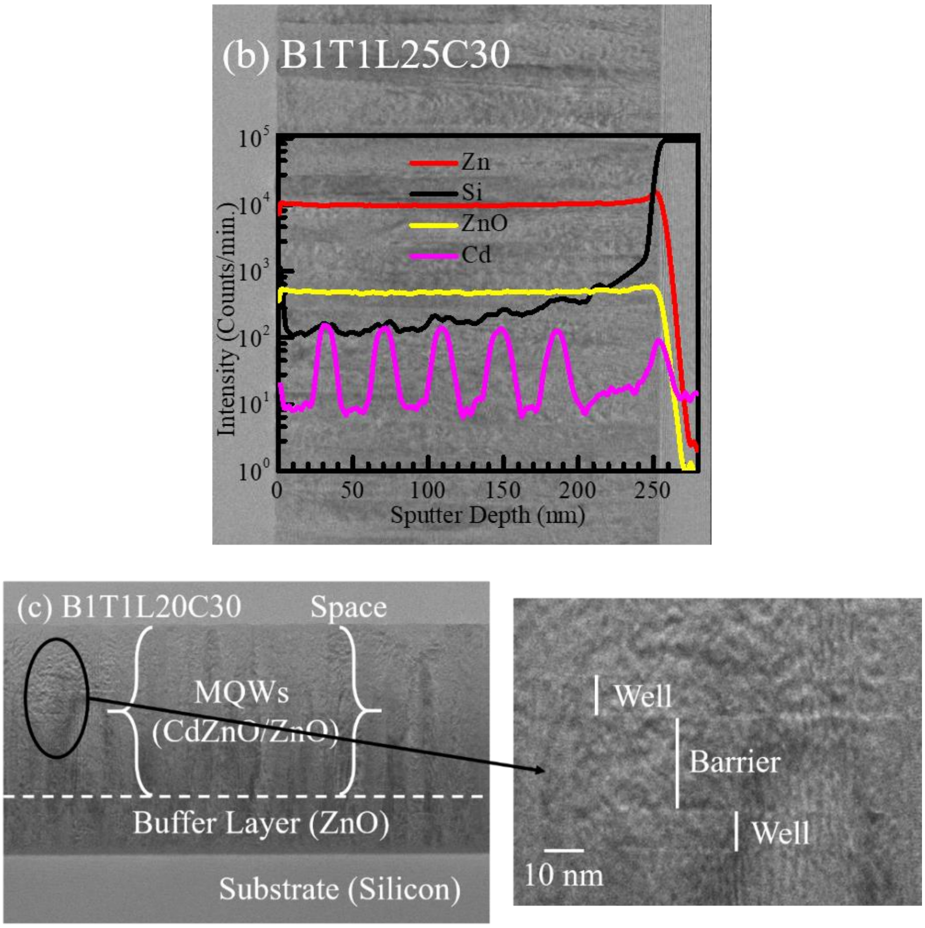

Figure 6.6 *(a) Cross-sectional HRTEM of sample 7, (b) SIMS coupled with TEM image of sample 7, and (c) Cross-sectional HRTEM of sample 6.*

This small lattice mismatch will be beneficial in realizing the SC using this material system, as it leads to reduction in the charge carrier recombination at the interface [22]. The HRTEM analysis is also performed for other samples and to avoid the redundancy, the data are not shown here.

6.3.5 EDX analysis

Furthermore, EDX analysis is performed on the cross sectional portion of the sample 6 as shown in Figure 6.7 to confirm the constituents element in the deposited MQWs structure by DIBS system. But from the figure we can see that, Cd is not clearly detected due to the sensitivity limitation of the instrument, while other elements are clearly detected in the EDX profile.

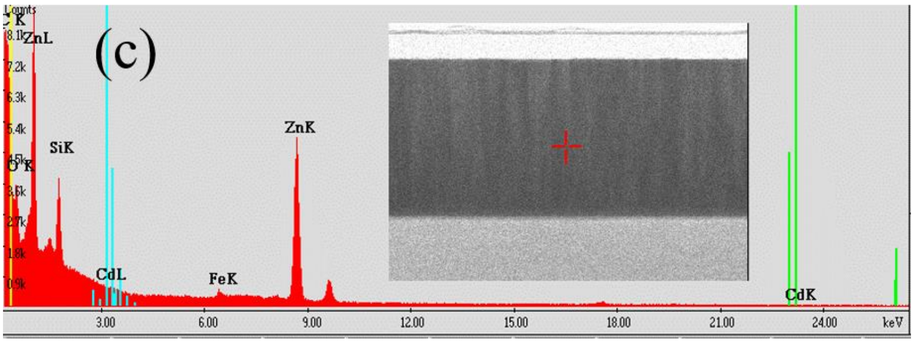

Figure 6.7 *EDX of sample 8 with the inset showing its cross-sectional HR-TEM of which EDX is performed.*

6.3.6 I-V measurement

After the successful fabrication of the CdZnO/ZnO-based MQWs structure, the CdZnO/ZnO-based MQWSC is fabricated using the optimized process. A schematic representation of the fabricated MQWSC is depicted in Figure 6.8. The fabricated structure consists of 100 nm of GZO acting as *n*-type material, 5 pairs of MQWs with CdZnO as well layer and ZnO as barrier layer having thicknesses of 10 and 15 nm, respectively. This whole structure is deposited on *p*-type silicon substrate acting as *p*-type layer for the MQWSC. The reason behind the choosing *p*-type silicon is that till now, we have not obtained reliable homo-junction of ZnO material system having Sb: ZnO as *p*-type material and Ga: ZnO as *n*-type material. Although, we have obtained reliable *p*-type ZnO in our lab.

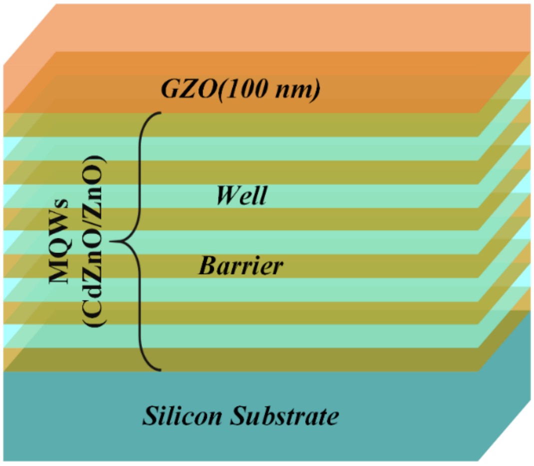

Figure 6.8 *Schematic of CdZnO/ZnO-based MQWSC deposited on p-type silicon substrate.*

Now, *I-V* characterization of the above fabricated structure is performed using the solar cell tester system at the standard test condition. The illuminated *I-V* characteristic of both in linear as logarithm axis is shown in Figure 6.9. From the figure it can be seen that the rectification ratio at ± 500 mV is ~18. And the performance parameters of the MQWSC obtained are shown in Table 6.4.

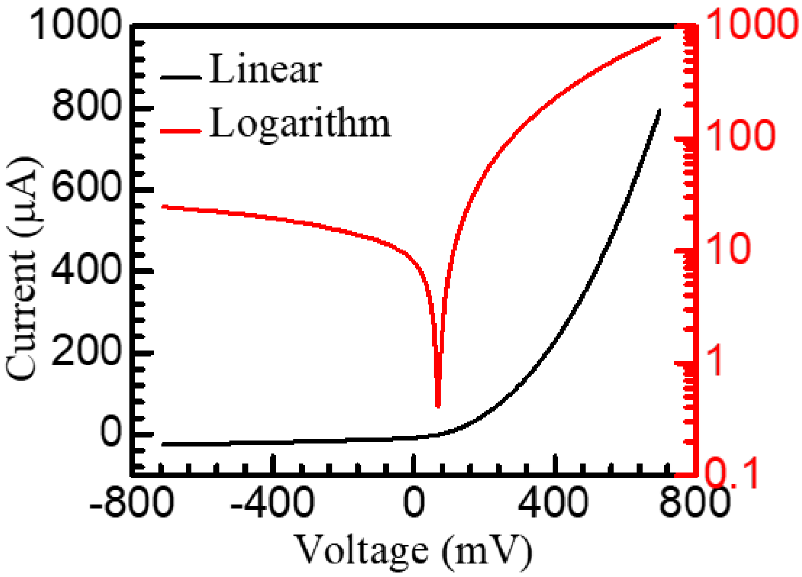

Figure 6.9 *Illuminated I-V characteristics of the CdZnO/ZnO-based MQWSC deposited on the p-type silicon substrate.*

Table 6.4: *Performance parameters of CdZnO/ZnO-based MQWSC*

Parameters	**V_{oc} (mV)**	**I_{sc} (μA)**	**V_m (mV)**	**I_m (μA)**	**P_m (nW)**
Values	69	8	38	5	190

From the table as well as from the figure it can be concluded that, the device performance is very poor as the values of the performance parameters is very low. The reason behind the low open-circuit voltage is *p*-type silicon (having low energy bandgap of 1.1 eV) used as the *p*-type layer in MQWSC. And also the high lattice mismatching of silicon and ZnO materials leads to higher recombination of the charge carrier before collection at the contacts, therefore the device produces very less short-circuit current. So, the material having low lattice mismatch with the ZnO material and having *p*-type conductivity is to be used for the

MQWSC fabrication. Secondly, the high composition of Cd in CdZnO can be used, so that the energy bandgap of the material reduces and therefore leading to the absorption of additional low energy photons and hence increasing the short-circuit current.

6.4. Conclusion

The CdZnO/ZnO-based MQWs structure are fabricated successfully for the first time by DIBS using the 4-inch-diameter CdZnO and ZnO targets at different deposition conditions. The films deposited at 100 °C substrate temperature and 14 W beam power show the best performance with respect to other deposition conditions, as confirmed by SIMS analysis. The HRTEM analysis shows that well and barrier layers are not separately visible, although SIMS results indicate the separate layers formation. This might be due to the very small lattice mismatch between the successive layers deposited. Therefore, it will benefit in a better performance of solar cell, as carrier recombination at the interfaces of the MQWs structure will be less.

For the complete structure fabrication of CdZnO/ZnO-based MQWSC, the *p*-type conductivity material having compatibility with the ZnO material i.e. having low lattice mismatch is to be used, so that charge carrier recombination can be minimised.

6.5. References

[1] L. Zhu, M. Yoshita, J. Tsai, Y. Wang, C. Hong, G. Chi, C. Kim, P. Yu, H. Akiyama, “Diagnosis of GaInAs/GaAsP multiple quantum well solar cells with bragg reflectors via absolute electroluminescence,” IEEE Journal of Photovoltaics, vol. 7, no. 3 pp. 781-786, 2017.

[2] V. Awasthi, S.K. Pandey, S. Verma, S. Mukherjee, “Room temperature blue LED based on p-ZnO/(CdZnO/ZnO) MQWs/n-ZnO,” Journal of Luminescence, vol. 180, pp. 204-208, 2016.

[3] J. Pereiro, C. Rivera, A. Navarro, E. Munoz, R. Czernecki, S. Grzanka, and M. Leszczynski, “Optimization of InGaN-GaN MQW photodetector structures for high-responsivity

performance," IEEE Journal of Quantum Electronics, vol. 45, no. 6, pp. 617-622, 2009.

[4] K. Y. Lai, G. J. Lin, C. Y. Chen, Y. L. Lai, and J. H. He, "Origin of hot carriers in InGaN-based quantum-well solar cells," IEEE Electron Device Letters, vol. 32, no. 2, pp. 179-181, 2010.

[5] D. N. Bose, P. Banerji, S. Bhunia, Y. Aparna, M. B. Chhetri, and B. R. Chakraborty, "Determination of well widths in a MOVPE-grown InGaAs/InP multi-quantum well structure using SIMS and photoluminescence," Applied Surface Science, vol. 158, no. 1-2, pp. 16-20, 2000.

[6] R. Bhardwaj, P. Sharma, R. Singh, M. Gupta, and S. Mukherjee, "High responsivity $Mg_xZn_{1-x}O$ based ultraviolet photodetector fabricated by dual ion beam sputtering," IEEE Sensors Journal, vol. 18, no. 7 pp. 2744-2750, 2018.

[7] K. Matsushima, R. Shimizu, T. Ide, D. Yamashita, H. Seo, K. Koga, M. Shiratani, and N. Itagaki, "Fabrication of ZnInON/ZnO multi-quantum well solar cells," Thin Solid Films, vol. 587, pp. 106-111, 2015.

[8] L. Ma, Z. Xia, V. Atuchin, M. Molokeev, S. Auluck, A. H. Reshak, and Q. Liu, "Engineering oxygen vacancies towards self-activated $BaLuAl_xZn_{4-x}O_{7-(1-x)/2}$ photoluminescent materials: an experimental and theoretical analysis," Physical Chemistry Chemical Physics, vol. 17, no. 46, pp. 31188-31194, 2015.

[9] B. S. Sengar, V. Garg, A. Kumar, V. Awasthi, S. Kumar, V. V. Atuchin, and S. Mukherjee., "Band alignment of Cd-free (Zn, Mg)O layer with $Cu_2ZnSn(S,Se)_4$ and its effect on the photovoltaic properties," Optical Materials, vol. 84, pp. 748-756, 2018.

[10] M. A. Khan, P. Kumar, M. Das, M. T. Htay, A. Agarwal, and S. Mukherjee, "Drain Current Optimization in DIBS-grown MgZnO/CdZnO HFET," IEEE Transactions on Electron Devices, vol. 67, no. 6, pp. 2276-2281, 2020.

[11] M. A. Khan, P. Kumar, G. Siddharth, M. Das, and S. Mukherjee, "Analysis of drain current in polycrystalline MgZnO/ZnO and

MgZnO/CdZnO HFET," IEEE Transactions on Electron Devices, vol. 66, no. 12, pp. 5097-5102, 2019.

[12] B.S. Sengar, V. Garg, V. Awasthi, S. Kumar, C. Mukherjee, M. Gupta, and S. Mukherjee, "Growth and characterization of dual ion beam sputtered $Cu_2ZnSn(S,Se)_4$ thin films for cost-effective photovoltaic application," Solar Energy, vol. 139 pp. 1-12, 2016.

[13] V. Garg, B. S. Sengar, V. Awasthi, A. Kumar, R. Singh, S. Kumar, V. V. Atuchin, and S. Mukherjee, "Investigation of Dual-Ion Beam Sputter-Instigated Plasmon Generation in TCOs: A Case Study of GZO," ACS Appl Mater Interfaces, vol. 10, no. 6, pp. 5464-5474, 2018.

[14] S. K. Pandey, S. K. Pandey, C. Mukherjee, P. Mishra, M. Gupta, S. R. Barman, S. W. D'Souza, and S. Mukherjee, "Effect of growth temperature on structural, electrical and optical properties of dual ion beam sputtered ZnO thin films," Journal of Materials Science: Materials in Electronics, vol. 24, no. 7 pp. 2541-2547, 2013.

[15] S. K. Pandey, V. Awasthi, S. Verma, and S. Mukherjee, "Blue electroluminescence from Sb-ZnO/Cd-ZnO/Ga-ZnO heterojunction diode fabricated by dual ion beam sputtering," Optics Express, vol. 22, no. 25, pp.30983-30991, 2014.

[16] M. Cohen, "X-Ray Diffraction Addison-Wesley Metallurgy Series," 1956.

[17] C. V. Ramana, S. Utsunomiya, R. C. Ewing, U. Becker, V. V. Atuchin, V. Sh Aliev, and V. N. Kruchinin, "Spectroscopic ellipsometry characterization of the optical properties and thermal stability of ZrO_2 films made by ion-beam assisted deposition," Applied Physics Letters, vol. 92, no. 1, p. 011917, 2008.

[18] J. A. Wollam Company, Incorporation, CompleteEASE TM Data Analysis Manual, 1-207, 2011.

[19] D. E. Aspnes, and A. A. Studna, "Dielectric functions and optical parameters of Si, Ge, GaP, GaAs, GaSb, InP, InAs, and InSb from 1.5 to 6.0 eV," Physical Review B, vol. 27 no. 2, pp. 985-1009,

1983.

[20] D. E. Carlson, and C. W. Magee, “A SIMS analysis of deuterium diffusion in hydrogenated amorphous silicon,” Applied Physics Letters, vol. 33, no. 1, pp. 81-83, 1978.

[21] D. M. Detert, S. H. M. Lim, K. Tom, A. V. Luce, A. Anders, O. D. Dubon, K. M. Yu, and W. Walukiewicz, “Crystal structure and properties of $Cd_xZn_{1-x}O$ alloys across the full composition range,” Applied Physics Letters, vol. 102, no. 7, p. 232103, 2013.

[22] M. Ettenberg, and G. H. Olsen, “The recombination properties of lattice-mismatched $In_xGa_{1-x}P/GaAs$ heterojunctions,” Journal of Applied Physics, vol. 48, no. 10, pp. 4275-4280, 1977.

Chapter 7

Conclusion and Future Scope

The prime objective of this research work is to analyse the MQWSC by developing the analytical models and numerical simulation in silvaco atlas, and finally fabricating the MQWs for photovoltaic application. In the developed analytical models, significant improvements are made upon the pre-existing models reported in the literature for predicting device performance matrix for MQWSC. The American Society for Testing and Materials (ASTM) standards data sheets are utilized for attaining photon flux density instead of Plank's blackbody radiation law. The numerical simulation has also been performed using the silvaco atlas simulation tool just to verify the results obtained from the analytical model. Further, the photon flux density is utilized to evaluate the performance parameters of MQWSC and bulk p-i-n solar cell.

For the first time, MQWs of CdZnO/ZnO-based material system are realized by dual ion beam sputtering (DIBS) system, by performing optimization at different deposition conditions in terms of ion beam power, substrate temperature, and time cessation between deposition of successive layers. The effects of DIBS deposition conditions are analysed by secondary ion mass spectroscopy (SIMS) and high-resolution transmission electron microscopy (HRTEM) and discussed systematically.

7.1 Conclusions

The main outcomes of this thesis are summarized as follows:

1) A physics based generic analytical model for both the *p-i-n* and MQW structures is developed for the calculation of device performance parameters and obtaining *J-V* characteristics of the solar cell. The results show that the inclusion of QWs in the depletion region of the *p-i-n* solar cell leads to the enhancement of ~27% in the conversion efficiency for the same composition

(x = 0.1) in $In_xGa_{1-x}N$. For MQWSC, the conversion efficiency increases by ~30 and ~27% if the indium composition in $In_xGa_{1-x}N$ increases from x = 0.1 to 0.2 and further to x = 0.3. The temperature-dependent study of the device performance parameters has shown that, with the increase in temperature, conversion efficiency decreases for both the solar cell. Approximately, 11.6 and 9.7% decrements in the conversion efficiency of the *p*-*i*-*n* and MQWSC, respectively, are obtained as the temperature increases from 200 to 400 K. The MQWSC has demonstrated more favorable temperature dependence of the efficiency compared to *p*-*i*-*n* solar cell. The study of the effect of number of quantum wells on the solar cell have shown that the increase in the number of QWs from 10-20 leads to the increment in conversion efficiency from 4.28 to 4.89%. The analytical model described, and the corresponding results analyzed here can be used as the suitable model for estimating the performance parameters of MQWSC and *p*-*i*-*n* solar cells consisting of various material system.

2) An analytical and simulation study has been presented for the CdZnO/ZnO-based MQWSC with CdZnO/ZnO as the intrinsic layer, SZO as *p*-type layer and GZO as *n*-type layer of the *p*-*i*-*n* solar cell. The study of the device performance parameters with temperature shown a negative temperature coefficient of V_{oc}, and positive temperature coefficient of both J_{sc} and η i.e. -2.63×10-3 mV/˚C, 2.43×10-3 mA/cm2.˚C and 2.91×10-3 %/˚C, respectively. Approximately, 14% increment in the conversion efficiency of MQWSC is observed as the temperature increases from 220 to 380 K. This work suggests, that CdZnO/ZnO-based MQWSCs can be efficiently utilized in concentrator photovoltaic applications, where positive temperature coefficient of η is crucial. An increase in the number of QWs from 3 to 19 leads to the decrement in the performance parameters of MQWSC. This study significantly explores the

possibility of efficient absorption of high energy photons and probability of positive temperature coefficient of η utilizing a low-cost ZnO-based MQWSC.

3) As the solar cells are operated under non-STC conditions, therefore in this study impact of change in solar irradiance on the performance parameters of CdZnO/ZnO-based MQWSC is also performed. Approximately, 6% increase is observed in the η of MQWSC, as I increases from 10 to 5000 mW/cm^2. This study considerably explores the likelihood of efficient absorption of short wavelength photons and improving η of MQWSC by using concentrator.

4) The CdZnO/ZnO-based MQWs structure are fabricated successfully for the first time by DIBS using the 4-inch-diameter CdZnO and ZnO targets at different deposition conditions. The films deposited at 100 ˚C substrate temperature and 14 W beam power show the best performance with respect to other deposition conditions, as confirmed by SIMS analysis. The HRTEM analysis shows that well and barrier layers are not separately visible, although SIMS results indicate the separate layers formation. This might be due to the very small lattice mismatch between the successive layers deposited. Therefore, it will benefit in a better performance of SC, as carrier recombination at the interfaces will be less.

7.2 Future Scope

The following are the summary of future work:

1) Fabrication of the complete CdZnO/ZnO-based MQWSC by DIBS system, as this system can be utilized for large area application.

2) Thereafter, performing the optimization based on the number of quantum wells, well and barrier layer thickness, so that maximum conversion efficiency can be achieved.

3) The optimization based on higher composition of Cd in CdZnO

can be performed, as the energy bandgap of the material reduces with higher Cd and therefore leads to the absorption of additional low energy photons and hence increasing the short-circuit current.

4) Fabrication of the strain balance MQWSC by utilizing MgZnO in place of ZnO, as MgZnO produces tensile strain compared to the compressive strain produced by CdZnO.
5) Fabrication of MQWSC on flexible substrate.
6) As, MQWSC can be used in MJSC for current matching of sub-cells. So, this has to be first optimized using analytical modelling and then can be fabricated.